

NANOSTRUCTURED CUPROUS OXIDE SYNTHESIZED BY BIPOLAR
ELECTROCHEMISTRY

By

Steven McWilliams

B.Sc., University of New Brunswick, 2016

A Thesis Submitted in Partial Fulfillment
of the Requirements for the Degree of

Master of Science

In the Graduate Academic Unit of Chemistry

Supervisor: Anna Ignaszak, PhD, Chemistry
Examining Board: C. Adam Dyker, PhD, Chemistry
Igor Mastikhin, PhD, Physics

This thesis is accepted by the
Dean of Graduate Studies

THE UNIVERSITY OF NEW BRUNSWICK

March, 2020

© Steven McWilliams, 2020

Abstract

This thesis covers the development of and groundwork for an environmentally benign approach for the fabrication of cuprous oxide (Cu_2O). By controlling the conditions that are applied to the reaction, the successful synthesis of uniform shapes and sizes of Cu_2O particles were achieved. The advantage of this approach over other existing synthesis methods lies in its potential ability to generate non-stoichiometric oxides, which demonstrate different photoelectrochemical and optical properties as compared to a control sample. Furthermore, with varying reaction conditions, there was a slight improvement of the carrier concentration, absorption of light, and photocurrent generation. Scanning electron microscope (SEM)/Transmission electron microscope (TEM) analyses showed that the structures appear to be built from substructures. Data from X-ray powder diffraction (XRD) determined that the nanoparticles are cubic in shape and the product is phase pure. Evidence provided by illuminating the sample under open circuit potential (OCP) conditions indicate that the Cu_2O produced is a P-type semiconductor.

Acknowledgments

First and foremost, I would like to acknowledge my supervisor Dr. Anna Ignaszak for taking me on as a student. Her guidance, wisdom, and expertise enabled me to explore a new form of Chemistry that I was previously unfamiliar with. I would also like to acknowledge the staff at the University of New Brunswick (UNB) for enabling me to further study Cu_2O by supporting me through cutting FTO plates (Brian Malcolm) or supplementary copper plates (Mike Albright, Adam Fowler). This extends to the physics department (Brian Titus), without whom my bipolar reactor may not have even existed. Thank you, Steven Cogswell of UNB's Microscopy and Microanalysis, who tirelessly assisted me in my training for both SEM and TEM.

Finally, I would like to acknowledge my wife (Jennifer McWilliams) for her love and support both by enduring my countless hours of ranting about frustrating results and always willing to lend a helping hand to talk me through it all. Without her, my Masters of Science in Chemistry would not have been possible. For that, I am truly thankful.

Table of Contents	
Abstract	ii
Acknowledgments	iii
Table of Contents	iv
List of Tables	vii
List of Nomenclature	xiii
List of Equations	xiv
List of Nomenclature	xviii
1.0. Introduction	1
1.1 Renewables and Climate Change	2
1.1.1 Climate Change and Weather Effects	2
1.1.2 Natural Resources	3
1.1.3 History of Solar Cells: Fundamental Mechanism Development for Solar Cell Operation	3
1.1.4. Solar Cell Requirements	8
1.2 Metal Oxides and Their Applications	10
1.2.1 Metal Oxides	10
1.2.2 Cu₂O Properties	11
1.2.3. Crystal Structure of Cu₂O	11
1.2.4. Cu₂O: P-type or N-type?	12
1.3. Green Chemistry	14
1.3.1. What is Green Chemistry?	14
1.4. Bipolar Electrochemistry	16
1.4.1 Electrochemistry versus Bipolar Electrochemistry	16
1.4.2 Open versus Closed Bipolar Electrochemistry	17
1.4.3. Current Flow and Resistance	20
1.4.4. pH	21
1.4.5. Why Bipolar Electrochemistry?	22
2.0. Experimental	24
2.1. Bipolar Electrochemical Cell	24
2.2. Filtration	25
2.3. Filter Paper and Electrode Preparation	26
2.3.1 FTO Cleaning	26
2.3.2. Electrode Fabrication	26

2.3.3. Cu ₂ O film on Filter Paper.....	27
2.4. Electrochemical Analysis.....	29
2.4.1. Open-Circuit Potential.....	29
2.4.2. Current-Time.....	30
2.4.3. Impedance Analysis.....	30
2.4.4. Mott-Schottky (M-S).....	31
2.5.2. Scanning Electron Microscopy (SEM).....	31
2.5.3. Epoxy Cross-Section Examination.....	32
2.5.4. Sputtering.....	32
2.5.5. X-Ray Diffraction (XRD).....	33
2.5.6. X-Ray Photoelectron Spectroscopy (XPS).....	34
2.5.7. Diffusive Reflectance Spectroscopy (DRS).....	34
2.5.8. List of Materials.....	36
3.0. Results.....	37
3.1. Cu ₂ O Bipolar Electrochemical Synthesis.....	37
3.1.1. Cu ₂ O Formation.....	37
3.1.2. Minimum Change in Voltage.....	39
3.2. Effect of Synthetic Conditions.....	42
3.2.1. Effect of Applied Potential.....	43
3.2.2. Effect of Time.....	43
3.2.3 Effect of pH.....	44
3.3. Yield.....	44
4.0. Morphological Studies Across Cu ₂ O Samples.....	46
4.1. Effect of Applied Potential.....	46
4.1.1. Applied Potential with Surfactant.....	47
4.1.2. Effect of Time.....	48
4.1.3. Effect of pH on Morphology.....	49
4.1.4. Substructure Generation.....	50
5.0. Characterization.....	53
5.1. X-Ray Diffraction.....	53
5.2 X-Ray Photoelectron Spectroscopy.....	63
6.0. Optical Studies.....	68
6.1. UV-Vis Diffusive Reflectance.....	68

7.0. Electrochemical Analysis	72
7.1. Mott-Schottky	72
7.2. Carrier Lifetime	75
7.3. Photocurrent	77
7.4. Impedance Analysis	80
7.5. Charge Carrier Diffusion Length	82
8.0. Summary	86
9.0. pH Analysis of Powders and Plates	89
9.1. Introduction	89
9.2. Cu₂O Plates and Powder Synthesis Conditions	89
9.3. Powder Characterization	91
9.3.1. X-Ray Diffraction Analysis	91
9.3.2 (Photo) Electrochemical Analysis	93
9.4 Conclusion	100
10.0. Future Research	102
11. References	103
Curriculum Vitae	

List of Tables

Table 1. Refinement data collected from the Rietveld analysis of room temperature XRD for BPE-made Cu ₂ O. All samples showed very good correlation with the Cu ₂ O model (space group: <i>Pn-3m</i> , with atom positions for Cu of (0,0,0) and O of (1/4, 1/4, 1/4). Parameter χ^2 is goodness of fit, R_{wp} is weighted profile, R_p is profile residual, and a is the lattice parameter in Angstroms (Å). Crystallite size is also represented with respect to applied potential and time.	59
Table 2. Calculated average of % reflectance with respect to wavelength region per sample.	69
Table 3. Band-gap values determined via Kubelka-Munk plot.	71
Table 4. Calculated carrier concentrations determined by slope of M-S plot.....	74
Table 5. Calculated carrier lifetimes of synthesized samples.	77
Table 6. Calculated values of R_{ct} , R_{tr} , R_{ct}/R_{tr} , L_D by Nyquist plot.....	85
Table 7. Carrier concentration, Flat-band potential obtained by M-S for pH samples...	96
Table 8. Carrier lifetime of pH samples.....	97

List of Figures

Fig. 1. Graph illustrating the change in global surface temperatures relative to 1951-1980 average temperatures. Data source: NASA's Goddard Institute for Space Studies (GISS).	3
Fig. 2. Carrier flow inside a PV cell under illumination. E_g represents the band-gap which excites the material and allows for polarization to occur. The electrons and electron holes are denoted by the solid and hollow circles, respectively. Finally, the depletion region represents the electric field that is generated by the initial recombination of electrons and electron holes.....	6
Fig. 3. PV material commonly utilized in commercial products.	10
Fig. 4. Crystal structure of Cu_2O (Cubic).	12
Fig. 5. Effect of applied potential on BPE where E_{tot} represents the total applied potential across the cell, ΔE_{elec} represents the minimum redox potential required to pass through the BPE for the faradaic reactions to occur, and $\eta_{\text{an/cat}}$ represents the overpotentials driving the reaction at the extremities.	18
Fig. 6. Representation of current in the system both without (A) and with (B) a BPE. Within an open bipolar electrochemical cell, there are two potential paths for current to flow. The bottom images are represented as electric field, E , with x representing position in the cell.	20
Fig. 7. (Left) Individual components of a PEC cell (Cu BPE, driving electrodes, plexiglass spacers, holder rod, screw, and custom teflon cap). (Right) Assembled cell ready for immersion in electrolyte.	25

Fig. 8. Electrode fabrication by depositing Cu ₂ O suspension onto 1 cm x 1 cm active area FTO sites.	27
Fig. 9. Filter paper deposition for ultraviolet-visible (UV-Vis) diffusive reflectance and for cutting into 1 x 1 cm squares for XPS.....	28
Fig. 10. Image of a PEC cell set-up consisting of a Pt counter electrode, Ag AgCl reference electrode and fabricated Cu ₂ O FTO electrode.....	29
Fig. 11. Specular and diffusive reflectance.....	36
Fig. 12. Redox reactions inside bipolar reactor filled with Cu gluconate associated with generation of Cu ions for Cu ₂ O production at 80° C. H _{2(g)} generated by the reduction of H ₂ O (cathodic reaction) while O _{2(g)} is generated by the oxidation of OH ⁻ (anodic reaction).....	39
Fig. 13. Progression of the generation of Cu ₂ O. (a) Progression of the synthesis from start (0 min) until the shut off period of 60 min via removal of solution at specified time intervals. (b-g) Progression of the reaction remaining inside the bipolar cell at times; 0, 5, 10, 20, 40, 60 min respectfully.....	39
Fig. 14. Depicting both the Frost and Pourbaix diagram for Cu species.	43
Fig. 15. SEM image with corresponding TEM insert shows the structure of Cu ₂ O obtained at 4.5 V and 8.0 V.....	47
Fig. 16. TEM of Cu ₂ O after sonication without HMT surfactant (left) and with HMT (right).....	48
Fig. 17. TEM images of both 4.5 V-3H (left) and 4.5 V-1H (Right) with star like agglomerates.	49
Fig. 18. TEM image of sample synthesized at 7.0 V with a pH of 5.4.	50

Fig. 19. Cu ₂ O TEM images indicating substructure generation 4.5 V (Left), 7.0 V (Right).	51
Fig. 20. Enlarged image of multi-crystal lattice section (7.0 V).....	52
Fig. 21. XRD of Cu ₂ O formed via bipolar electrochemistry utilizing calcium gluconate as a complexing agent.	54
Fig. 22. XRD of cuprous oxide synthesized with potassium gluconate at pH 6.8 with an applied potential of 8.0 V.....	55
Fig. 23. XRD spectrum of Cu ₂ O synthesized by wet-chemical route.....	56
Fig. 24. XRD spectrum of Cu ₂ O synthesized at 8.0 V for one hour at pH 6.8 at 80°C. .	57
Fig. 25. Stacked XRD of all samples compared to commercial material.	59
Fig. 26. Refinement profile for the Rietveld analysis of room temperature XRD data collected for 4.5 V3H fitted to the model proposed for Cu ₂ O by Foo et al. [56].....	60
Fig. 27. Refinement profile for the Rietveld analysis of room temperature XRD data collected for 4.5 V1H fitted to the model proposed for Cu ₂ O by Foo et al. [56].....	61
Fig. 28. Refinement profile for the Rietveld analysis of room temperature XRD data collected for 5.0 V fitted to the model proposed for Cu ₂ O by Foo et al. [56].	61
Fig. 29. Refinement profile for the Rietveld analysis of room temperature XRD data collected for 6.0 V fitted to the model proposed for Cu ₂ O by Foo et al. [56].	62
Fig. 30. Refinement profile for the Rietveld analysis of room temperature XRD data collected for 7.0 V fitted to the model proposed for Cu ₂ O by Foo et al. [56].	62
Fig. 31. Refinement profile for the Rietveld analysis of room temperature XRD data collected for 8.0 V fitted to the model proposed for Cu ₂ O by Foo et al. [56].	63
Fig. 32. XPS spectrum of Cu ₂ O 5.0 V sample with Cu 2p _{3/2} peak deconvoluted to determine individual peak contributions.	64

Fig. 33. Cu ₂ p _{3/2} peak for all synthesized samples representing shift compared to commercial material.....	65
Fig. 34. O1s scan of 8.0 V sample depicting the possible presence of adsorbed O ₂ (A). O1s scan of all samples overlaid (B).....	66
Fig. 35. % reflectance spectrum of all synthesized samples compared to commercial material.....	69
Fig. 36. Kubelka-Munk function for all samples compared to commercial material	71
Fig. 37. M-S plot of samples obtained under dark conditions	73
Fig. 38. Flat band potentials determined by x-int for each sample plotted vs. the sample name.	74
Fig. 39. Phase-Log(Frequency) spectrum (Bode plot) to determine carrier lifetime by f_{max}	75
Fig. 40. Photocurrent generated under OCP conditions. Samples exposed to illumination and dark conditions for 50 s intervals for a total of 400 s.....	78
Fig. 41. Theoretical impedance spectra.....	81
Fig. 42. Nyquist plot of sample synthesized at 8.0 V under both dark and illuminated conditions.	82
Fig. 43. Cross-section of Cu ₂ O layer on glass slide coated in epoxy-resin. The layer of Cu ₂ O is slightly suspended from the FTO depicted as a brighter white due to the cross section cut.....	83
Fig. 44. Current increase and decrease due to Cu ion generation and consumption with respect to samples prepared by specific pH.	91
Fig. 45. XRD of the powders for the pH samples compared to 8.0 V-1H sample previously synthesized.	92

Fig. 46. XRD of Cu ₂ O layer formed on Cu plate during synthesis at various pH.	93
Fig. 47. M-S plot across -0.7 – 0 V applied potential for samples synthesized with varying pH levels.	95
Fig. 48. Bode analysis of pH samples	97
Fig. 49. Photocurrent generation of pH by Xe lamp alternating illumination with 8.0 V- 1H serving as a reference material.	98
Fig. 50. Photocurrent generation by Cu BPE immersed in sodium sulfate electrolyte under alternating illumination conditions.	100

List of Nomenclature

l_{channel} – Distance Between Driving Electrodes (cm)

E_g – Bandgap Energy (eV)

E_{tot} – Applied Potential (V)

F – Faraday's Constant (C mol⁻¹)

f_{peak} – Peak Frequency (Hz)

$h\nu$ – Photon Energy (eV)

I – Current (A)

i_{bpe} – Total Current Through Bipolar Electrode (mA)

i_{sol} – Total Current Through Solution (mA)

i_{tot} – Total Current (mA)

K – Absorbance Coefficient

l_{channel} – Distance Between Driving Electrodes (cm)

l_{elec} – Length of Bipolar Electrode

L_n – Electron Diffusion Length (μm)

M – Molar Mass (g/mol)

m – Mass (g)

n – Number of Electrons

Q – Electric Charge (A s)

R – Gas Constant (J/mol K)

R_{bpe} – Bipolar Electrode Resistance

R_{ct} – Charge Transfer Resistance (Ω)

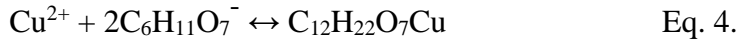
S – Scattering Coefficient

List of Equations

$$\Delta E_{\text{elec}} = E_{\text{tot}} \left(\frac{I_{\text{elec}}}{I_{\text{channel}}} \right) \quad \text{Eq. 1.}$$

$$E_{\text{tot}} = E_{\text{red}} - E_{\text{ox}} \quad \text{Eq. 2.}$$

$$T = I \times t \times K \times V_s \quad \text{Eq. 3.}$$



$$E = -59.2 \text{ mV} \cdot \text{pH} \quad \text{Eq. 8.}$$



$$E = 0.34 \text{ V} \quad \text{Eq. 10.}$$

$$\text{Cell potential} = E_{\text{red}} - E_{\text{ox}} \quad \text{Eq. 11.}$$

$$\text{Cell potential} = (-0.402) - (0.34) = -0.74 \text{ V} \quad \text{Eq. 12.}$$

$$E_{\text{tot}} = \Delta E_{\text{elec}} \left(\frac{I_{\text{channel}}}{I_{\text{elec}}} \right) \quad \text{Eq. 13.}$$

$$E_{\text{tot}} = (-0.74256\text{V}) \left(\frac{1.0\text{cm}}{0.2\text{cm}} \right) \quad \text{Eq. 14.}$$

$$E_{\text{tot}} = -3.7128 \text{ V} \quad \text{Eq. 15.}$$

$$m = (QF)(Mn) \quad \text{Eq. 16.}$$

$$D = \frac{(0.9\lambda)}{\beta \cos\theta} \quad \text{Eq. 17.}$$

$$F(R) = \frac{K}{S} = \frac{1-R_\infty}{2R_\infty} \quad \text{Eq. 18}$$

$$\frac{1}{c^2} = \frac{2}{\epsilon\epsilon_0 A^2 e N_A} \left(V - V_{\text{fb}} - \frac{k_\beta T}{e} \right) \quad \text{Eq. 19.}$$

$$Slope = \frac{2}{\varepsilon\varepsilon_0 A^2 e N_A} \quad \text{Eq. 20.}$$

$$\tau = \frac{1}{2\pi f_{max}} \quad \text{Eq. 21.}$$

$$Ln = L * \sqrt{\left(\frac{\tau n}{\tau d}\right)} = L * \sqrt{\left(\frac{Rct}{Rtr}\right)} \quad \text{Eq. 22.}$$

List of Acronyms

- BE – Binding Energy (eV)
- BPE – Bipolar Electrode
- CB – Conduction Band
- CTAB – Cetrimonium Bromide
- DB – Double Beam
- DRS – Diffuse Reflectance Spectroscopy
- DSSC – Dye Sensitizing Solar Cell
- EDX – Energy Dispersive X-Ray
- FTO – Fluorine Doped Tin Oxide
- FWHM – Full-Width Half Max
- HMT – Hexamethylenetetramine
- I-t – Current-Time
- K-M – Kubelka-Munk
- LSV – Linear Sweep Voltammetry
- M-S – Mott-Schottky
- OCP – Open-Circuit Potential
- PEC – Photoelectrochemical Cell
- PV – Photovoltaic
- PVP – Polyvinylpyrrolidone
- SDS – Sodium Dodecyl Sulfate
- SEM – Scanning Electron Microscopy
- TEM – Transmission Electron Microscopy
- UV-VIS – Ultraviolet-Visible

VB – Valence Band

XPS – X-Ray Photoelectron Spectroscopy

XRD – X-Ray Diffraction

Cu₂O – Cuprous Oxide

CH₃COOH – Acetic Acid

CuOH – Copper (I) Hydroxide

Cu(OH)₂ – Copper Hydroxide

Ag/AgCl – Silver/Silver Chloride

ZnO – Zinc Oxide

HCl – Hydrochloric Acid

CaCO₃ – Calcium Carbonate

K₂CO₃ – Potassium Carbonate

List of Nomenclature

l_{channel} – Distance Between Driving Electrodes (cm)

E_g – Bandgap Energy (eV)

E_{tot} – Applied Potential (V)

F – Faraday's Constant (C mol⁻¹)

f_{peak} – Peak Frequency (Hz)

$h\nu$ – Photon Energy (eV)

I – Current (A)

i_{bpe} – Total Current Through Bipolar Electrode (mA)

i_{sol} – Total Current Through Solution (mA)

i_{tot} – Total Current (mA)

K – Absorbance coefficient

l_{channel} – Distance Between Driving Electrodes (cm)

l_{elec} – Length of Bipolar Electrode

L_n – Electron Diffusion Length (μm)

M – Molar Mass (g/mol)

m – Mass (g)

n – Number of Electrons

Q – Electric Charge (A s)

R – Gas Constant (J/mol K)

R_{bpe} – Bipolar Electrode Resistance

R_{ct} – Charge Transfer Resistance (Ω)

S – Scattering Coefficient

1.0. Introduction

In recent years, technological advancements have improved the cost, production, and working efficiency of clean energy resources [1]. This has allowed for various forms of energy generation (e.g., solar) to become more accessible to industry and the public. However, there is still a long way for clean energy resources to become mainstream. For example, in 2017, non-hydro renewables only contributed 7% to the overall electricity generation across Canada, with 0.5% from solar [2]. As such, photovoltaics (PVs) has not proven to be one of the most promising means for harvesting clean energy [3].

The focus of the present research is the synthesis of cuprous oxide (Cu_2O) via a bipolar electrochemical approach. Due to the large sensitivity of Cu_2O properties to its method of synthesis, new electronic properties may be attained [4]. Cu_2O is currently in development for two main energy-based applications: PV and photoelectrochemical cells (PECs). Although the theoretical solar conversion efficiency of Cu_2O is 18%, current solar cells have only reached values of 3-5% [5]. In comparison, solar panels have an average conversion efficiency between 15-18% based on current silicon (Si) solar cells. This is believed to be due to the lack of N-type semi-conducting Cu_2O materials, as it is known to naturally exhibit P-type semi-conductivity. By introducing bipolar electrochemistry as a method of synthesis, this research aimed to create N/P-type semi-conducting Cu_2O . By altering the pH of the solution, the generation of N-type Cu_2O has been demonstrated. Furthermore, by increasing the applied

potential, the photocarrier concentration, lifetime, and charge transfer increased, which caused an increase in the photocurrent generation of P-type Cu₂O. Thus, by altering these parameters, this could potentially increase the efficiency of Cu₂O as a material for solar cell applications.

1.1 Renewables and Climate Change

1.1.1 Climate Change and Weather Effects

Climate change is a controversial topic. However, there is an undeniable truth: the earth's temperatures are rising, and biodiversity is being affected. Fig. 1 demonstrates the average temperature that was recorded between 1951 and 1980 [6]. Within the last 10 years, the highest temperatures to date have been documented, with detrimental effects for many species stemming from small changes in mean water temperatures [7]. For example, in recent news, the first mammalian species (*Bramble cay melomys*) has officially been identified as extinct [8]. This begs the question: Is this only the beginning? This evidence, and more, is driving the scientific community toward a common goal: To determine, optimize, and utilize renewable, clean energy sources to help ameliorate the damage caused by humans.

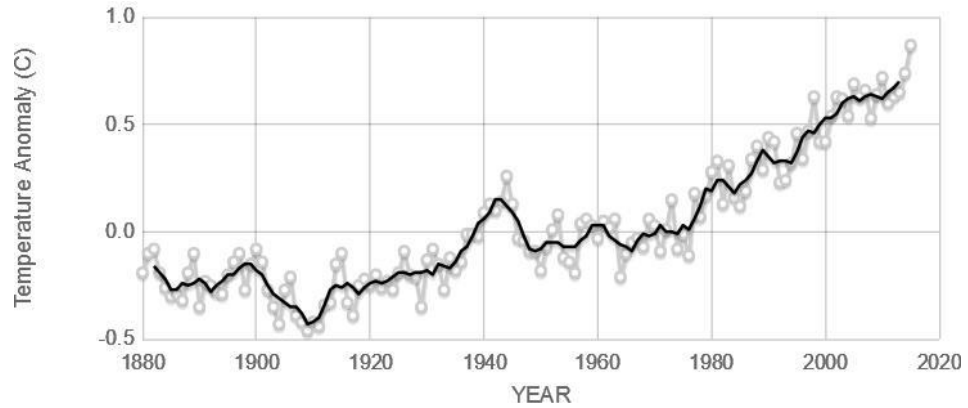


Fig. 1. Graph illustrating the change in global surface temperatures relative to 1951-1980 average temperatures. Data source: NASA's Goddard Institute for Space Studies (GISS).

1.1.2 Natural Resources

Recent statistics for global energy generation saw an increase of 25% in renewables [9]. In 2017, a total growth of renewable sources of 2.1% was achieved, doubling the previous year [9]. As astounding as this may seem, most of the demand for increased energy consumption was covered by oil, gas, and coal, which resulted in a 1.4% increase in CO₂ emission levels and an historical high of 32.5 gigatons. However, wind and PVs also increased in their individual contributions to renewable energies by 36% and 27% [10], respectively. Clearly, these increases demonstrate that much work is left to be done to ensure that only renewable energies are being utilized.

1.1.3 History of Solar Cells: Fundamental Mechanism Development for Solar Cell Operation

In 1839, Becquerel discovered the photoelectric effect/PV effect [11]. By placing two platinum (Pt) electrodes in an aqueous electrolyte and illuminating

it, electrons or other free carriers were emitted. Later, in 1876, professor William Grylls Adams witnessed the PV effect by exposing selenium to light to generate electricity; however, this was too small to power any device. In 1883, Charles Fritts created the first ever working selenium (Se) cell by coating the Se with a thin layer of gold (Au). This was the first ever solar cell, with a conversion efficiency of 1%. In 1954, Chaplin, Fuller, and Pearson developed the first Si-based solar cell that was capable of powering electrical equipment, reaching solar conversion efficiencies of 6% [12]. These are the commercially known solar cells of today. As time has passed, extensive research has taken place on the potential to switch to renewable, nonpolluting sources of energy to help mitigate the current impact of the population on the earth [13]. Currently, solar-thermal (i.e., solar energy is turned into heat), solar-fuel (i.e., solar energy is turned into chemical energy), and solar-electrical (i.e., solar energy is turned into electricity) are available [14]. Under the context of the work presented in this thesis, the focus will be on the solar-electrical system.

Solar-electric utilises the PV effect to produce electricity directly from sunlight using N- and P-type semi-conductors. N-type semi-conductors are electron rich, which enable electron mobile carriers to transfer charge. This results in the doping of polycrystalline Si (a natural semi-conductor with a low volume of free electrons) with a donor material (i.e., phosphorus; P). Phosphorus (P) atoms have 5 valance electrons, allowing for one free electron once it is bonded with the polycrystalline material. This then enables the one electron to move as a charge carrier. However, if one attempts to create a solar cell from

only this material, the electrons would move in random directions, resulting in no current through the load due to the lack of an electric field. Therefore, in order to generate the electric field to induce the electron flow, a P-N junction is required. Instead of an electron rich material, like P, if boron (B; an acceptor atom) is used to dope Si, there will be an excess of electron holes throughout the system. This is due to B having only three valence electrons, leaving a vacant space for an electron where B atoms bond to the polycrystalline Si. In this material, the electron holes act as the majority charge carrier. If these two doped materials were to come together, electrons from the N-type material will migrate towards the P-type material and the holes closest to the surface of the junction will recombine with the electrons. This is known as a depletion region, which has no free electrons or holes. However, due to the electron migration, the N-type semi-conductor becomes positively charged on the surface, while the P-side becomes negatively charged. This electric field generates the necessary driving force which enables the unidirectional movement of the photogenerated electrons and, therefore, produces what is known as photocurrent.

When light strikes the P-N junction and penetrates the depletion region, the photon energy is strong enough to break apart the recombined electron-hole pairs (Fig. 2) [15]. The electric field will then separate these pairs. From there, the concentration of electrons in the N-region and holes in the P-region become so high as to create a potential difference form between them. As soon as a load is connected, electrons flow through the load and into the P-region to recombine with the electron holes, resulting in the generation of direct current (DC).

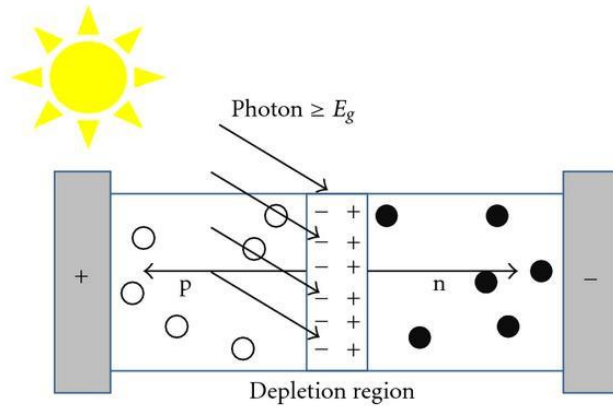


Fig. 2. Carrier flow inside a PV cell under illumination. E_g represents the band-gap which excites the material and allows for polarization to occur. The electrons and electron holes are denoted by the solid and hollow circles, respectively. Finally, the depletion region represents the electric field that is generated by the initial recombination of electrons and electron holes.

Before materials are utilized on the commercial scale, they are first tested in a PEC. PECs use a solid-electrolyte junction and are currently researched as a potential avenue for the generation of hydrogen (H^+) gas. In N-type doped material, the fermi-level is located near the valence band of the material and is typically higher than the fermi-level of the electrolyte [16]. However, upon contact with the electrolyte, an equilibrium condition must be met. Therefore, electrons will transfer from the semi-conductor to the electrolyte until equilibrium is reached. This produces a positive charge on the surface of the semi-conductor like what is seen with PVs when they generate an electric field. For example, for an N-type semi-conductor that is illuminated, electrons that are generated are first transported into the bulk of the material due to the electric field. They are then transported to the counter electrode through the external circuit to reduce H^+ ions to an H_2 gas species. The holes are then utilized to

oxidize water (H_2O) into oxygen (O_2) gas and H^+ ions on the surface of the electrode. In contrast, if a doped P-type semi-conductor is used, equilibrium is achieved by the flow of electrons into the material, which results in the generation of an electric field. This electric field has a negative charge which forms on the surface of the electrode. From there, photogenerated electrons are then pushed to the surface of the electrode by the electric field and are utilized to reduce the H^+ species, and the electron holes move towards the bulk of the material, flowing through the external circuit to the counter electrode to oxidize H_2O . Although not commercially utilized as a solar cell due to the complexity of parasitic reactions, PECs are an excellent and commonly employed way to determine the photo capabilities of materials prior to its application in PVs [17].

In hopes of obtaining industrial applications in the near future, two main approaches of implementing PECs into industrial applications include panel-based and slurry-based systems. Panel-based PECs consist of an electrode (N- or P-type semi-conductor) that is set-up with an external circuit and are immersed in an electrolyte (this is similar to a standard electrochemical set-up, whereas a slurry-based system consists of a suspension of N-/P-type semi-conducting material) [18]. Panel-based material tend to have better control via a connection to an external circuit, which allows for modification to the applied potential; however, this is limited by its surface contact with the electrolyte. Slurry-based systems have significant surface contact with the electrolyte; nevertheless, harvesting of $\text{H}_{2(\text{g})}$ can be difficult due to the entire suspension generating gas. Both systems have their respective advantages and disadvantages, but more is

known about panel-based PEC systems as they have been thoroughly researched due to their overlap with PV cell technologies [19]. The major advantage that PECs have for industrial application is the simple process of gas generation [20]. Furthermore, PECs possess a wide operating temperature range, with no intrinsic upper limit, and can move slightly below zero without having to first warm up [21].

1.1.4. Solar Cell Requirements

Based on semi-conducting physics, PV materials should have the following qualities [20]:

- A band-gap between 1.1eV – 1.7eV
- A direct band-gap
- The ability to be both P- and N-type
- An abundance of source material
- A simple synthesis method
- Should be non-toxic
- Good physical and chemical stability

These qualities can significantly increase and decrease the efficiency of the material. The band-gap between 1.1 – 1.7 eV is chosen as it represents the most significant percentage of light wavelengths within the AM 1.5 spectrum [20]. Direct band-gaps have strong optical transitions that allow for simultaneous absorption and emission of photons, whereas indirect band-gaps have weak transitions that result in thicker solar cells. Although thicker solar cells were

originally thought to be better due to their ability to increase the absorption of solar irradiation, this actually results in a decrease in the efficiency of the material. This decrease is caused by an increase in the minority carrier diffusion length, which also results in an increase in recombination. A material that is capable of being both P- and N-type allows for the creation of homo-junction solar cells, as well as has the potential for better communication between the two semi-conductors when the overlaying of valence/conduction bands is improved. Finally, the material should be non-toxic and provide good chemical and physical stability to allow for long lifetimes, without potentially contaminating the surrounding area upon decomposition.

Although many materials embody one or multiple of the above qualities, no material has been discovered to be the perfect candidate that matches every category. Current markets have a huge dependence on crystalline Si; however, industrial synthesis methods can be quite hazardous and costly. As demonstrated by Fig. 3, as of 2001, Si is the leading PV material, dominating approximately 85% of the current market [22]. However, with continuous growing interest in PV materials, the search will continue into new methods of synthesis and alternative materials to provide a cheap –but viable– option for the solar future. One such potential avenue is Cu_2O . Cu_2O 's advantages consist of the material exhibiting a direct band-gap, it is naturally abundant, has non-toxic properties, can be both N-/P-type, and is associated with a scalable, low-cost synthesis method[23]. However, the current draw-backs of the material stem from its larger

band-gap and insufficient stability under aqueous conditions[23]. Further research is needed before Cu_2O can be a commercially viable alternative to Si.

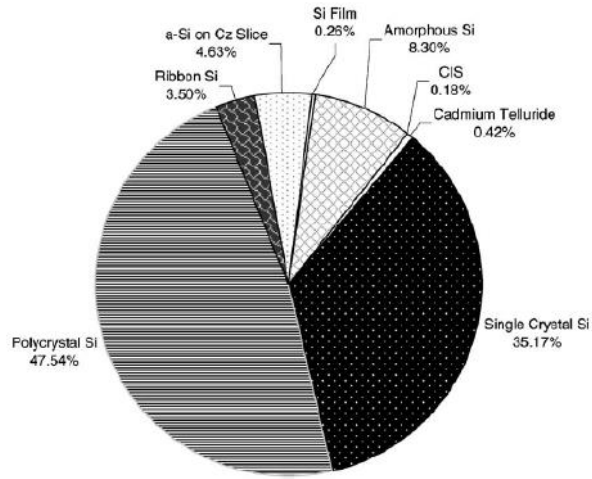


Fig. 3. PV material commonly utilized in commercial products.

1.2 Metal Oxides and Their Applications

1.2.1 Metal Oxides

Many inorganic PV devices that are utilized for converting light into energy are crafted from metal oxides. Metal oxides are ideal due to their broad bandgap semi-conducting properties [24][25], versatility of their properties, as well as their low-cost synthesis and ease of scalability [25]. Metal oxides have been produced on the industrial scene for a long time, which has resulted in an abundance of research surrounding various potential synthesis routes (e.g., electrochemical, chemical/chemical vapour, thermal depositions, sol-gel processing, high energy ball milling) [26]. Efforts in this area of research have provided invaluable findings, which have enabled researchers to obtain

morphology and size control, and well as the fine-tuning of electrochemical and optical properties.

1.2.2 Cu₂O Properties

Cu₂O is a non-stoichiometric defect metal oxide with intrinsic P-type semi-conducting properties [23]. Recognized since 1920 as a potential candidate for solar cell materials, it was neglected due to the discovery of Si and germanium (Ge). However, interest in Cu₂O was reintroduced in the 1970's by PV researchers due to its possible low cost of fabrication. Despite the prospect of more efficient metal oxides, such as perovskite (CaTiO₃), Cu₂O continues to be considered a promising alternative to Si due to its environmental advantages such as its non-toxicity, abundance, and its simplicity of production [27]. Furthermore, Cu₂O has a direct band-gap (which results in the direct emission of a photon, whereas an indirect band-gap results in some level of momentum transfer to the crystal lattice, resulting in an intermediate state) ranging between 1.9-2.2eV. The increase above 2.0 eV is due to quantum confinement effects as the material's crystallites become smaller. As such, this range falls nicely into the visible region.

1.2.3. Crystal Structure of Cu₂O

Cu₂O has a simple cubic structure (Fig. 4.), which can be described as a cubic unit with a lattice constant of 0.427 nm. It belongs to the space group, Pn-3m, with O₂ atoms at the corners of the crystal unit cell and a tetrahedral unit of Cu₄O at the centre [28]. However, within the lattice, each copper (Cu) atom

coordinates to two O₂ atoms, with each O₂ atom surrounded by four Cu. This gives it a 2:1 stoichiometry.

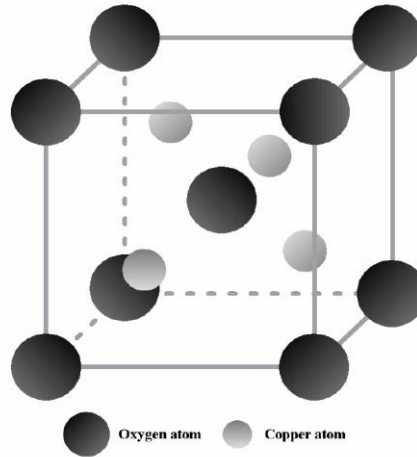


Fig. 4. Crystal structure of Cu₂O (Cubic).

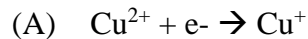
1.2.4. Cu₂O: P-type or N-type?

Cu₂O is known as an intrinsic P-type semi-conducting material [29]. However, with recent advancements in how defects can contribute to the type of conductivity that is produced by these compounds, evidence has demonstrated that N-type Cu₂O is a possibility [30]. Albeit, the plausibility of a “true” N-type Cu₂O is still very much debated. Ideas have ranged from experimental to theoretical and computational testing [32][33]. Original theories relating to the conversion of the oxide to N-type were attributed to donating impurities that were either forming and/or were trapped inside the crystal during the formation of the product, which increases the free electrons that are available. Current theories, however, have moved towards a focus on the defects are plaguing the

crystal structure or the effects that occur on the surface of the Cu₂O crystal structure [34].

P-type semi-conductivity is more commonly accepted in Cu₂O as being induced by the presence of Cu vacancies [29]. Cu vacancies are hole producing and are easily formed due to their low formation energy, and are very effective at readily releasing electron holes because of the small ionisation energy (i.e., it has a shallow acceptor level) with respect to hole production [29]. These are the conditions that make Cu₂O an intrinsic P-type semi-conductor. On the other hand, O₂ vacancies act as donors. Evidence that points towards this is in samples of Cu₂O that exhibit N-type behaviours and noticeably high O₂ defect photoluminescence peaks. It is then demonstrated that Cu₂O can be converted to a P-type semi-conducting material upon annealing, prompting the loss of the O₂ vacancy peaks.

Research focusing around the varying conditions of Cu₂O's synthesis has determined a large pH dependence on the semi-conducting properties [35]. Looking at the formation of Cu₂O through the reaction of Cu²⁺ and OH⁻ ions, we can see the formation of Cu₂O by first reducing Cu²⁺ species to Cu⁺ (A) resulting in the reaction with free hydroxides (B) to produce Cu₂O.



Based on the reaction presented above (B), the reaction is highly dependent on the hydroxide (OH⁻) concentration and, therefore, pH. By manipulating the pH of the solution to be significantly lower, the reaction occurs in a Cu rich/O₂ poor

environment, which may induce a reduction in Cu vacancies and an increase in O₂ vacancies. This may provide many donors, resulting in the N-type properties. However, the concentration of Cu species must be considered. If the concentration of the Cu species is also significantly lower, a standard P-type Cu₂O will be obtained.

Further research has been conducted into the conditions surrounding Cu₂O and the conditions by which N-type can be obtained [36]. Instead of manipulating the pH of the solution, the introduction of cationic/anionic surfactants was investigated. Through applying cationic surfactants to the reaction conditions, N-type Cu₂O was obtained. Furthermore, anionic surfactants provided P-type properties. The difference in properties relied on the significant difference in how the surfactants worked. In the case of utilizing cationic surfactants for N-type conductivity, the cationic surfactant was constantly flowing over the Cu₂O growth surface, which created an obstacle for the OH⁻ ions to absorb onto the Cu₂O through electrostatic means. As Cu₂O was made rapidly, the lack of OH⁻ presence induced a lack of O₂ that was available for the formation. This enabled the production of O₂ vacancies. Conversely, the anionic surfactant may act as a barrier to the Cu⁺ ions, which allowed for the formation of Cu vacancies and the production of a P-type semi-conductor [36].

1.3. Green Chemistry

1.3.1. What is Green Chemistry?

Current industrial methods result in high pollution rates which are caused by such instances as by-products, large volumes of solvents, and energy consumption. Proper methods for disposal tend to be expensive on an industrial scale, which may serve to persuade companies to look toward cheaper alternatives in waste disposal. As a result, water ways, soils, air, and the general environment are all polluted [38]. These issues result in the large increase in the overall demand for eco-friendly alternatives for solvents and renewable energy sources to reduce the use of fossil fuels. Originally defined in 1990, green chemistry is the pursuit to reduce or eliminate the generation of hazardous substances to prevent pollution to the environment [39]. Twelve principles of green chemistry have been proposed: 1) prevent waste; 2) atom economy; 3) less hazardous synthesis; 4) design benign chemicals; 5) benign solvents and auxiliaries; 6) design for energy efficiency; 7) use of renewable feedstock; 8) reduce derivatives; 9) catalysis (versus stoichiometric); 10) design for degradation; 11) real-time analysis for pollution prevention; and 12) inherently benign chemistry for accident prevention [39]. Although, ideally, all twelve principles should be applied to a proposed solution to enable the improvement of current methods, adjustments to some of these factors can still significantly contribute to the general impact that they have on the environment.

According to J. H. Clark in the article “Green chemistry: Challenges and opportunities”, in 1999, the United States spent \$115 billion dollars on waste treatment and disposal [40]. Considering the evolution of techniques and the products that are produced by competing companies by slightly changing

formulations, the accumulation of chemical waste will rise at an exponential rate as more products are released to market. Few, if any, green chemistry methods are used in current day mass production, despite the overall potential for financial savings over time. Due to the upfront research and development costs of new methods and optimization, many companies have strayed away from moving forward with green chemistry. However, it was presented by D. Constable et al. [41] that, by integrating green chemistry practices (i.e., solvent recovery), there could be a 66-89% reduction in the overall cost. As companies are looking at the short rather than the long-term benefits, industry needs to understand the potential positive difference in costs not only to themselves, but the negative costs to the environment if they continue on the path that they are currently on.

1.4. Bipolar Electrochemistry

1.4.1 Electrochemistry versus Bipolar Electrochemistry

In a standard 2-electrode electrochemical system, the electrodes are in direct electrical contact with the power supply and are physically separated (i.e., one cathode and one anode are present). This allows for the polarization of the solution and redox reactions to occur. Expanding on the typical 2-electrode system, bipolar electrochemistry utilizes a 3-electrode system. This alteration in design is derived from the question: What happens if a third, non-directly connected electrode is introduced into the center of the electric field that is produced by the two driving electrodes? While a potential difference is applied

between the two driving electrodes, an electric field is generated and, therefore, an electric field gradient is produced. Upon placing the third electrode between the two driving electrodes, the electrode becomes polarized by the electric field gradient and becomes the bipolar electrode (BPE). This electric field induces both a positive and negative pole on the BPE's two sides. The presence of this third electrode is the inherent difference between electrochemistry and bipolar electrochemistry.

1.4.2 Open versus Closed Bipolar Electrochemistry

Bipolar electrochemistry is split into two main subcategories: open and closed. Both electrochemical methods involve a 3-electrode system that is submerged in an electrolytic solution, with a potential that is applied between the two driving electrodes. The potential difference between the bipolar electrode and the electrolyte results in the polarization of the BPE, which produces the opposite charge on the surface with respect to the driving electrode. The potential difference is largest at the extremities of the bipolar electrode, which drives the faradaic reactions that occur on the surface (represented in Fig. 5) [42]. Open BPE (OBPE) and closed BPE (CBPE) require the same technique, however, with a slight change to the configuration of the cell. In CBPE, the bipolar electrode is placed between two electrolytes and acts as a barrier that prevents mixing between the two solutions. This then forces all current to flow through the bipolar electrode [43]. In comparison, OBPE involves placing all the electrodes in a single electrolytic bath. The two methods have their advantages and

disadvantages. For example, CBPE is better for grafting onto a conducting object, whereas OBPE is better for powder generation.

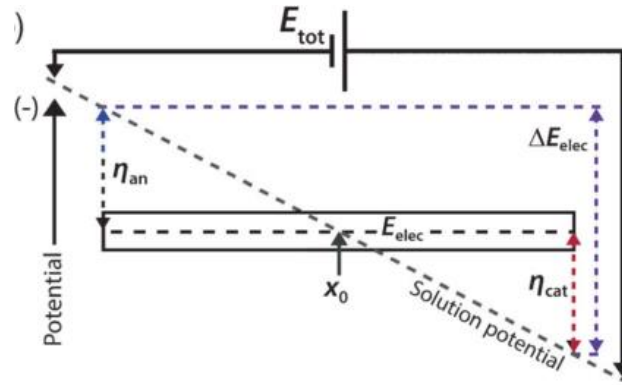


Fig. 5. Effect of applied potential on BPE where E_{tot} represents the total applied potential across the cell, ΔE_{elec} represents the minimum redox potential required to pass through the BPE for the faradaic reactions to occur, and $\eta_{an/cat}$ represents the overpotentials driving the reaction at the extremities.

Specific to OBPE, the formula for calculating the required applied potential (E_{tot}) for the system is represented by Eq.1. ΔE_{elec} represents the minimum potential applied for the faradaic reactions to occur at the extremities of the bipolar electrode. This is driven by the interfacial potential difference. Referring to Fig. 5, the solution potential varies along the length of the bipolar electrode due to the electric field. $l_{channel}$, as it is commonly denoted in the BPE formula, is the length of the channel between the two driving electrodes, while l_{elec} represents the length/thickness (depending on the orientation) of the bipolar electrode. Eq. 1, demonstrates a major dependence on the length of the channel and thickness/length of the bipolar electrode. However, this equation can only be applied if major assumptions are made (e.g., the bipolar electrode does not significantly impact the electric field of the solution). This is commonly not the

case, as will be discussed later. Comparatively, CBPE has a more simplified equation (Eq. 2). This is represented by E_{red} and E_{ox} , which are the electrochemical potentials of reduction reaction and oxidation reaction, respectively. Instead of what occurs with OPBE, all of the current is forced to run through the bipolar electrode, which polarizes the BPE and enables for the electrolysis of H_2O to occur at the extremities, as well as the preferred reactions. Therefore, the minimum voltage required for it to work would be the required voltage for the faradaic process, except with the addition of having to compensate for the ohmic drop.

$$\Delta E_{elec} = E_{tot} \left(\frac{l_{elec}}{l_{channel}} \right) \quad \text{Eq. 1.}$$

$$E_{tot} = E_{red} - E_{ox} \quad \text{Eq. 2.}$$

1.4.3. Current Flow and Resistance

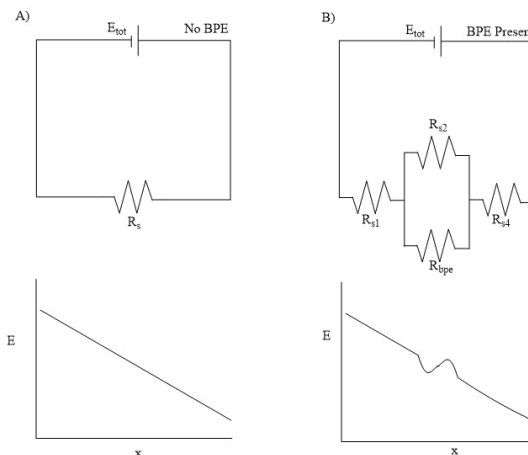


Fig. 6. Representation of current in the system both without (A) and with (B) a BPE. Within an open bipolar electrochemical cell, there are two potential paths for current to flow. The bottom images are represented as electric field, E , with x representing position in the cell.

The two pathways for current to flow are I_{sol} and I_{BPE} , which represent the current flowing through the solution and bipolar electrode, respectively. These two paths then comprise the total current flow (I_{tot}) as represented in Fig. 6. B by Fosdick et al. [42]. Also demonstrated by Fosdick et al., the absence of a bipolar electrode produces the expected resistance diagram of all current flowing through the solution (Fig. 6. A). The extent at which production occurs is dependent on the applied potential (E_{tot}) and the resistance of the solution (R_s); however, upon introducing the BPE, a new pathway is formed. This new pathway then removes some of the current from the solution due to the faradaic processes, represented as the resistance of the BPE (R_{bpe}). Taking a closer look at Fig. 6. B, the total resistance of the system is represented by four variables: Resistance of solution before contact with the BPE (R_{s1}), simultaneous to the BPE (R_{s2}), and

after the BPE (R_{s4}), R_{bpe} . If R_{s2} is significantly smaller than the R_{bpe} , then most of the current will flow through the solution, resulting in little perturbation of the system that is generated by the BPE. In contrast, if the $R_{bpe} < R_{s2}$, then the majority will flow through the BPE. When R_{bpe} is significantly less than the R_{s2} , this allows for either an increase or decrease in local electric field strength, and a nonlinear electric field that surrounds the BPE is produced. This procedure was named faradaic depolarization by Duval et al. [44], and was further expanded upon the process by indicating that the magnitude of the local field strength is dependent on the total electric field strength, concentration of supporting electrolyte, and properties of electrochemically active species (if present). Ultimately, this could be simplified to the applied potential and conductivity of the solution.

It is important to note that, in this work, the BPE is submerged in an electrolyte with a relatively large conductivity. Due to this, the BPE is assumed to have a minor amount of current flow as the difference in resistivity between the BPE and solution is likely sufficiently small.

1.4.4. pH

Inside an aqueous electrolytic system that is sufficiently conductive, the faradaic process for H_2O splitting readily occurs. Both H^+ and hydroxyl ions are produced, which can be identified as a constant change of pH in the system. However, despite changes in the local pH around the corresponding electrodes, no net charge is gathered inside of the cell, which results in the overall pH of the solution remaining at a constant level. As confirmed by Arora and colleagues

[45], they introduced a universal indicator into the electrochemical system, both with and without the use of a BPE. Without the use of the BPE, the change in the colour of the indicator is centralized at the driving electrodes. However, when one introduces a Pt wire to act as the BPE, a new center for the indicator forms. It is important to note that, based on the indicator, the local pH around the BPE is the opposite to its corresponding driving electrode, which indicates the opposite polarity [45].

1.4.5. Why Bipolar Electrochemistry?

Like any other method, bipolar electrochemistry has its advantages and disadvantages. Bipolar electrochemistry has the potential to answer some difficult questions, many of which can be addressed by applying bipolar electrochemistry principles (e.g., difficulty in making direct electrical contact to electrodes on the nanoscale, utilizing a non-uniform electric field to produce unique materials, generating metal oxides for photosensitive material applications). Bradley et al. [46] first demonstrated the connection of two 1 mm Cu beads in series by applying an electric field that was strong enough to allow for anodic oxidation to occur on one pole of the bead, followed by a reduction at the cathodic pole of the other. The Cu dendrites grew from one Cu bead and moved towards the other Cu bead until electrical contact was made. Influenced by their success, this group was able to further their work by connecting two Cu rings with a Si-based plate that was placed in the centre. The structures that were generated behaved like diodes. Due to the lack of direct electrical contact to the power source, many electrical contacts between the beads can be formed at once.

Furthermore, with a large enough electric field, the application can be translated to the nanoscale.

Variability in the interfacial potential difference along the BPE can cause a concentration gradient along the electrode's length. Shannon and Ramaswamy [47] demonstrated that, if multiple ions in solution are deposited at different potentials, they will then appear on the BPE at different lengths. For example, this can be seen by depositing both Au and silver (Ag) on a single stainless-steel electrode. The authors discovered that Au and Ag appeared at different locations on the electrode. This was caused by the different deposition potentials between Au and Ag. Therefore, the metal that required a larger deposition potential formed only on the extremities of the BPE, while the metal that required a lower deposition potential was able to reach further towards the centre of the electrode. This effect demonstrated the capabilities of bipolar electrochemistry to create gradients based on deposition potential. Bipolar electrochemistry can also be utilized for the synthesis of metal oxides, which can then be utilised in a wide variety of applications. As produced by our group, the implementation of a zinc (Zn) plate in deionized water can produce zinc oxide (ZnO) for the intended application of solar cells [48][49].

2.0. Experimental

This chapter will cover the techniques and apparatus that was utilized for the synthesis of Cu_2O through bipolar electrochemistry. This will be then followed by the fabrication of Cu_2O electrodes on fluorine-doped tin oxide (FTO) plates for the characterization and analysis of the properties of the material as detailed by various syntheses conditions.

2.1. Bipolar Electrochemical Cell

The bipolar electrochemical cell was designed by cutting and modifying a cylindrical piece of Teflon to enable it to fit within a 250.0 mL beaker. While designing this cell, the cylindrical piece of Teflon needed to be capable of holding two stainless-steel driving electrodes, which were separated by 1.0 cm with a pre-cleaned Cu plate that was suspended between the two driving electrodes (Fig. 7). For the driving electrodes and BPE to be held in parallel and to ensure that no shifts occurred during the reaction, plexiglass space holders were utilized. These plexiglass space holders were designed to withstand concentrated pressure by a screw, while distributing the pressure along an area of the driving electrode to allow for the electrode to remain stationary. The BPE holder was designed slightly differently than that of the stainless-steel driving electrodes: a plexiglass rod, with a slit cut into it, was designed to allow a screw to permeate through the glass and electrode, which allowed for the electrode to remain suspended. However, no pressure was required.

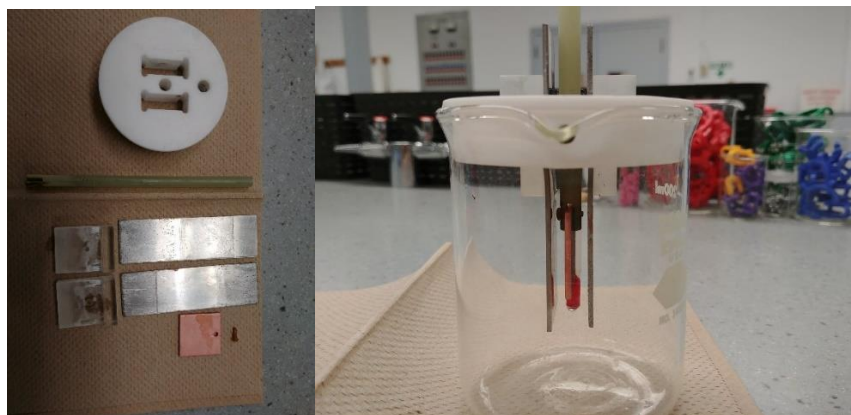


Fig. 7. (Left) Individual components of a PEC cell (Cu BPE, driving electrodes, plexiglass spacers, holder rod, screw, and custom teflon cap). (Right) Assembled cell ready for immersion in electrolyte.

The Cu plate was immersed in dilute nitric acid solution to remove any surface oxides that could passivate the Cu plate prior to being subjected to the current. A 250.0 mL beaker filled with 220 mL of 19.2 mMol potassium gluconate solution was heated on a hotplate covered by a watch glass until 80° C was obtained. The solution was then maintained at 80° C, while the specifically designed Teflon cap was placed onto the beaker. A Keysight E36106A DC power supply was connected via alligator clips to the driving electrodes, which enabled the potential I to be applied for a specific time (t).

2.2. Filtration

The collection of Cu_2O was done by filtering the 220.0 mL solution through a 0.22 μm nitrocellulose membrane (Millipore) with suction applied from a vacuum pump (Welch DryFast). Upon successful filtering of the product, initial washes with deionized H_2O were completed to wash any excess gluconate that may have been left on the surface. This was then followed by several small

washes with anhydrous ethanol (Commercial Alcohols) and suctioned dry over the course of 5 minutes to aid in drying the product. The filter paper was then collected into a 25.0 mL vial and subjected to low pressure nitrogen (N₂) airflow until dry to remove moisture before any potential decomposition could impact the material.

2.3. Filter Paper and Electrode Preparation

2.3.1 FTO Cleaning

7 Ω of FTO (Sigma-Aldrich) glass was cut into (1.5 cm x 6 cm) plates and were selected as the electrode material. The FTO glass was initially cleaned in pure deionized H₂O by sonication for 5 minutes in a Branson sonicating bath, followed by being wiped down with Kim wipes and dried in an oven at 50° C. The slides were then subjected to a second round of cleaning by first sonicating them in 10% acetone (Sigma-Aldrich) for 5 minutes, followed by a rinse and sonication in water for 5 minutes. The slides were then sonicated in 95% ethanol (Commercial Alcohols) for 10 minutes, rinsed in deionized H₂O once more, and dried using a N₂ gas stream. This process was completed twice to ensure that any foreign particulates were removed. The acetone was used in dilute concentrations due to reports of potential adsorption of acetone onto the surface of the FTO plate, which could prevent current from passing through it.

2.3.2. Electrode Fabrication

Cu₂O working electrodes were prepared by utilizing a suspension of Cu₂O colloids in ethanol at a concentration of 2 mg/mL (Fig. 8.). The suspension was

fabricated by submersing 10 mg of Cu_2O in 5 mL of anhydrous ethanol and sonicated for 1 hour to allow for proper dispersion. A 1 cm^2 square was cut out of a polymerase chain reaction (PCR, VWR) film, which was then placed onto the FTO plate to create a 1 cm^2 active deposition area. This was then placed into an oven at 70° C. Upon completion of the sonication, 125 μL of Cu_2O suspension was deposited onto the active area of the electrode and left to air-dry, leaving the electrode ready for characterization.

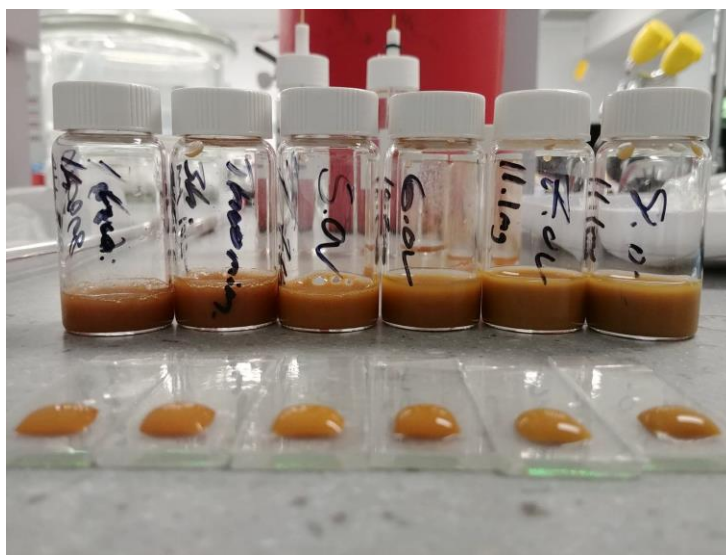


Fig. 8. Electrode fabrication by depositing Cu_2O suspension onto 1 cm x 1 cm active area FTO sites.

2.3.3. Cu_2O film on Filter Paper

Cu_2O colloids were suspended and dispersed onto filter paper for two reasons: 1) a large area of dispersion was needed so that the diffusive reflectance could occur (Fig. 9.), and 2) an additional 1 cm^2 cut-out of a single piece was collected for X-ray photoelectron spectroscopy (XPS) analysis. First, a dispersion of approximately 3 inches in diameter had to be obtained for diffusive

reflectance to be performed; thus, in order to keep every sample the same, the filtration set-up was used. Upon setting up the standard filtration and vacuum pump that was previously used, the suspension (2 mg/mL) was then re-sonicated for 5 minutes, followed by vortexing it to ensure a uniform suspension. This suspension was then poured into the filter set-up. Suction was turned on and off to allow the filter paper to lay flat on the base of the filter set-up, followed by allowing the solution to move through the filter paper via gravity for a more uniform film. This filter paper was collected, air-dried, and packaged for shipment to the University of Toronto (U of T) so that diffusive reflectance could be conducted. The previous step was repeated, however, with one alteration: upon drying the filter paper, multiple 1cm² cut-outs were obtained and placed between two glass slides that were secured to protect the sample. This was then shipped to Dalhousie's Clean Technologies Research Institute (CTRI) for XPS analysis.



Fig. 9. Filter paper deposition for ultraviolet-visible (UV-Vis) diffusive reflectance and for cutting into 1 x 1 cm squares for XPS.

2.4. Electrochemical Analysis

Electrochemical analysis was performed by CHI instrumentation-potentiostat model number CHI660E. Repurposing the previously made Teflon cap, it was possible to create a set-up that was like that of a PEC (Fig. 10). The previously made Cu_2O electrode was immersed in a 0.5 M solution of sodium sulfate (Na_2SO_4), with the polymerase chain reaction (PCR/VWR) film acting as a protective covering over the FTO plate. Doing so left only the Cu_2O active site exposed. A silver/silver chloride (Ag/AgCl) reference electrode and a Pt counter electrode was immersed into the electrolyte. To test the photosensitive properties, an 85 W (8500 Lumen) flashlight was mounted using a lab stand with an alternating barrier to prevent the passing of light.

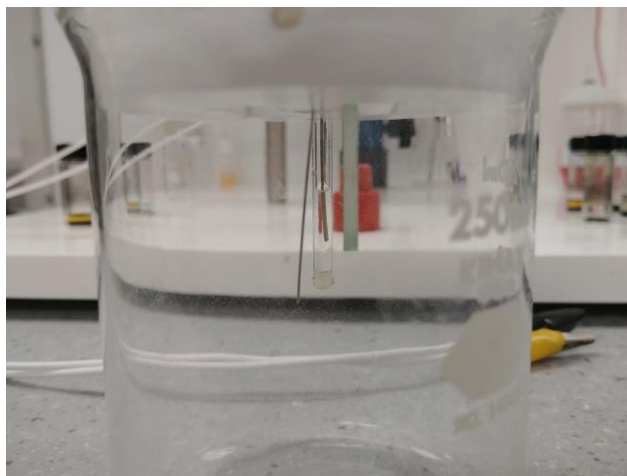


Fig. 10. Image of a PEC cell set-up consisting of a Pt counter electrode, Ag/AgCl reference electrode and fabricated $\text{Cu}_2\text{O}/\text{FTO}$ electrode.

2.4.1. Open-Circuit Potential

Open-circuit potential (OCP), also known as open cell voltage (V_{oc}), measures the difference between two terminals with no external load applied via

potentiostat. As changes of the material and electrolyte can have a significant impact on the OCP, it is often preferred under consistent conditions to remain comparable. In the definition of solar cells, PEC cells, and electrolytic cells, in general, OCP is the potential that needs to be applied to the system to cease the generation of current. This is important as it works to prevent the excess current that has an impact on the measured photocurrents and impedance analysis. In terms of stability, the OCP can also be a way to determine the stability of the material with respect to the electrolyte being used. This is determined in the literature as OCP, which is commonly considered a guide to navigate the thermodynamic tendency that materials will corrode; therefore, potentials applied below OCP are considered more thermodynamically stable (i.e., less likely to participate in corrosion) as compared to potentials above OCP. Samples were at OCP for a prolonged amount of time (1500 s) to ensure that equilibrium had been reached. Therefore, the material was left immersed in the electrolyte (sodium sulfate) for 1500 seconds prior to all measurements.

2.4.2. Current-Time

A single-potential amperometry technique was conducted under OCP while being exposed to alternating light and dark conditions. This was so that I-t graphs could be generated, which represented the photocurrent that was generated (i.e., illuminated) versus the dark. All trials were conducted over a duration of 400s. Dark and light conditions were alternated every 50 seconds.

2.4.3. Impedance Analysis

Impedance analysis allows for the determination of resistivity to current flow in a circuit while a potential is applied. Thus, impedance spectroscopy was used under OCP conditions from high (10000 Hz) to low (0.01 Hz) frequency. It is important, however, to ensure that the material is tested under the same conditions as the photocurrent to properly compare the two measurements.

2.4.4. Mott-Schottky (M-S)

Mott-Schottky (M-S) was measured after reaching equilibrium. In order to obtain the bulk carrier concentration, flat-band potential, and to determine the semi-conductivity, the sample was subjected to an applied potential in a reverse bias (-0.8 V – 0.1 V) under dark conditions.

2.5. Microscopy and Characterization

2.5.1. Transmission Electron Microscopy (TEM)

A JEOL JEM-2010 Scanning transmission electron microscope (SEM), with a Gatan Ultrascan camera, was used to collect the desired images. All samples were prepared on a nickel grid and performed with an accelerating voltage of 200 kV in the University of New Brunswick's (UNB) microscopy and microanalysis department. Further characterization was complimented at the Otto Schott Institute of Materials Research, Friedrich-Schiller University, Jena, Germany using JEOL 3010 and JEOL NeoARM.

2.5.2. Scanning Electron Microscopy (SEM)

UNB instrumentation consists of a JEOL JSM-6400 SEM, equipped with an EDAX Genesis 4000 energy dispersive X-Ray (EDX) analyzer with an applied accelerating voltage of 15 kV.

2.5.3. Epoxy Cross-Section Examination

The sample preparation department (i.e., Biology) was contracted to provide cross section samples of a previously deposited Cu₂O layer on a glass slide. The layer was prepared similarly to the Cu₂O electrodes and were immersed in a plastic epoxy mold diagonally, allowing for complete immersion of the active area. The epoxy mold consisted of an EPO fix kit (Struers) 25:3 resin to hardener ratio, followed by polishing via a 0.3 μm alumina (Al₂O₃) suspension (Buehler) and complimented with a grinding polisher (Logitech PMZA base with WG2 head). The cross sectioned slides were then delivered to SEM for analysis.

2.5.4. Sputtering

A sputter deposition technique utilizes three different components: a super ion gun (i.e., a metal filament that ejected electrons by thermionic emission) which collides with the sputtering gas (i.e., argon; Ar); a target, which is the material that is to be sputtered (i.e., carbon; C); and the sample to be coated. The accelerated noble gas contacts the target, resulting in the ejection of an ion of the target material at a relatively low kinetic energy. This was done purposely so that it could absorb onto the surface of the material. The thickness of the deposited film (T) can be summarized by Eq. 3:

$$T = l \times t \times K \times V_s \quad \text{Eq. 3}$$

Where I represents current, t represents time in minutes, K represents a constant denoted as 5, and V_s (KeV) representing the voltage setting. Edwards S150A sputter coater was used for all Au sputtering for SEM imaging.

2.5.5. X-Ray Diffraction (XRD)

X-ray diffraction (XRD) results in unique patterns of diffraction angles and allows for the determination of unknowns based on crystal structure. The Cu_2O samples that were collected were a fine powder; thus, they required no further processing. The Cu_2O sample was poured into a circular well and leveled off to allow for a smooth surface for proper diffraction. It was then placed onto a sample stage with three height settings. It is important to note that all samples were performed under the same height setting. However, if shifts in this height setting had occurred, it would be noticeable as these shifts would cause shifts in the XRD spectra, which could then prevent proper comparisons. All analyses were completed by a Bruker AXS D8 Advance solid-state powder diffraction XRD system that was equipped with a radiation safety enclosure. The X-ray source was a 2.2 kW Cu X-ray tube, with a maintained current of 40 kV and 25 mA. The X-ray optics were a Bragg-Brentano para-focusing mode, with divergence from a 1.0 mm slit and convergence at a 1.00 mm anti-scatter-receiving slit paired with a detector slit of 0.2 mm. The goniometer was computer-controlled, with a smallest angular step size of 0.0001° . The samples were scanned at a range of $10\text{-}90^\circ$. A step size of 0.02° every 1.0 s was used as the measurement conditions. A Sol-X (Peltier-cooled solid state [Si(Li)], with no correction for $\text{K}\beta$ radiation was used as the detector. Finally, data collection was

completed via a manually-controlled JOB program that employed a Doctrine Query Language (DQL) parameter file, which was refined by a program that was provided by Bruker. All information provided above is provided by UNB's XRD technologist, Dr. Venn Reddy. Additionally, Rietveld analysis was completed on all applied potential raw data samples by Dr. Donna Arnold.

2.5.6. X-Ray Photoelectron Spectroscopy (XPS)

XPS is a surface characterization technique that can analyze a sample that has a depth of up to 10 nm and determine the chemical element and nature of the chemical bond between the elements. Conducted under ultra-high vacuum, the sample is irradiated with X-rays that have enough energy to break away a photoelectron. Upon the ejection of a photoelectron, they are collected by an electron analyzer that measures the kinetic energy. A spectrum is developed, with the intensity relying on the number of electrons ejected at a specific binding energy versus time. These peaks are representative of a corresponding element. Due to the sensitivity of the ejected core electrons and the changes in the outer valence configuration, slight shifts can occur. These shifts can be utilised to help determine the valence state of the element and possible defects under the right conditions. The samples were measured at the Dalhousie University spectroscopy facility on a VG Microtech MultiLab ESCA 2000 System, with a 100 μm analyzer spatial resolution, 10 meV energy resolution, and Mg $K\alpha$ linewidth. Samples prepared for XPS were completed on filter paper.

2.5.7. Diffusive Reflectance Spectroscopy (DRS)

Diffusive reflectance spectroscopy (DRS) utilizes the reflection of light from a material to determine what wavelengths of light are absorbed versus reflected. Utilizing DRS can lead to obtaining important information from the spectrum (i.e., the band-gap). In order to understand diffusive reflectance, it must first be defined, which can be done by comparing it to specular reflectance. Specular reflectance and diffusive reflectance both occur on a single sample (Fig. 11). However, only diffusive reflectance is measured. Specular reflectance is what is observed if light is shined onto a mirror. The light from the light source would then bounce off of the surface of the mirror and, depending on the angle of incidence and the surface-based characteristics, reflect the light with respect to the angle. Diffusive reflectance can be explained with the help of a white wall. When light is shined onto a white wall in a single spot, the light will not become brighter or darker when observed from various angles. More technically, light moves to the sample, spectral reflectance occurs at the surface; however, some light passes through to the next particle, which could then continue to the next. Contact with the numerous particles within the sample allows for “absorbance” to occur before the light is reflected out of the sample and collected on the mirror. This is then directed to the detector, giving the resulting spectrum. Therefore, diffusive reflectance is important because it represents the diffraction of the crystalline sample [50].

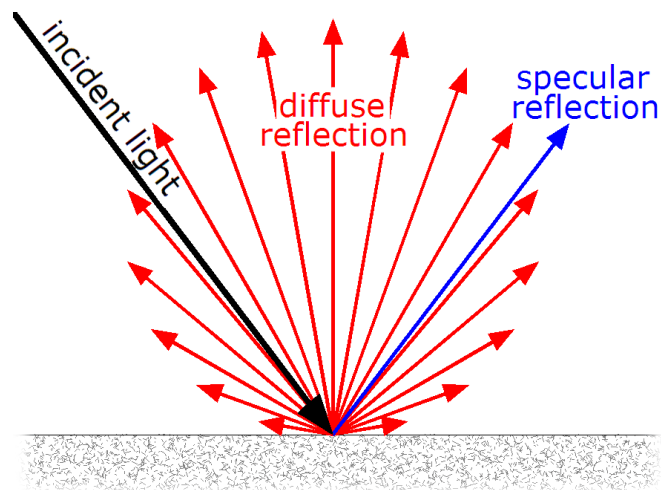


Fig. 11. Specular and diffusive reflectance.

The studies were performed at U of T's Analytical Laboratory for Environmental Science Research and Training Facility on a Lambda 25 UV/VIS spectrometer double beam (DB) instrument. The samples were prepared as previously discussed in section 2.3.3. Deposited samples were placed on the horizontal sample plate and examined from 200-800 nm.

2.5.8. List of Materials

Potassium D-gluconate ($\geq 99\%$, CAS# 299-27-4), FTO plates (300 mm x 399 mm x 2.2 mm resistivity $7 \Omega/\text{cm}^2$), and cuprous oxide ($\geq 99.99\%$, trace metal basis, CAS# 1317-39-1) were purchased from Sigma Aldrich. Anhydrous ethanol (100%, CAS# 64-17-5) was obtained from Commercial Alcohols and sodium sulfate ($>99\%$, CAS# 7757-82-6) was obtained from Fischer Scientific.

3.0. Results

3.1. Cu₂O Bipolar Electrochemical Synthesis

The purpose of this research was to investigate the properties of Cu₂O, which was synthesized via bipolar electrochemistry under varying conditions (e.g., potential, pH, time) while holding temperature and solution electrolyte concentration constant.

3.1.1. Cu₂O Formation

Fig. 12 depicts the reactions that are assumed to occur during oxidation of the Cu plate when it was submerged in the electrolyte. With an applied potential that was sufficiently high enough to polarize the BPE, faradaic reactions occurred on both sides of the Cu. The first observation that was made was the continuous formation of bubbles on both sides of the BPE, which indicated that the electrolysis of H₂O was occurring. This resulted in the generation of H₂ gas at the cathodic pole of the BPE and O₂ gas at the anodic pole of the BPE. Oxidation of the Cu plate occurred on the anodic pole of the BPE, which released Cu²⁺ that was paired with the reduction of H₂O on the cathodic pole. A complexation reaction then occurred, during which the Cu²⁺ ions complexed to the free gluconic acid ions to become Cu gluconate (Eq. 4.). The reaction began as a clear, colourless liquid and turned to a clear, light blue/blue colour. Indicating the complexation of the Cu²⁺ species. This prevented the reaction of Cu²⁺ ions to the free OH⁻ ions and its precipitation out of solution as Cu(OH)₂ (Fig. 12). Following the formation of the Cu²⁺ complex, two potential reactions occurred. As a sufficiently high concentration of Cu²⁺ species develops, an

equilibrium reaction on the Cu electrode surface can occur, resulting in the generation of Cu^+ species (Eq. 5). In previous literature, this has been reported to cause the formation of Cu_2O on the Cu electrode, as exhibited in Eq. 1. However, in this thesis, Cu_2O was both a powder and a film on the plate. An alternative reaction could be produced following the reduction of free gluconic acid to glucose (Eq. 6.). Glucose then reduces Cu^{2+} to Cu^+ , which allows for the Cu species to react with free OH^- ions, and a metastable product (i.e., CuOH , which is a yellow solution) to form. CuOH naturally decomposes to Cu_2O at 80°C during the bipolar electrochemical synthesis (i.e., an orange-red solution) as described in Eq. 2.

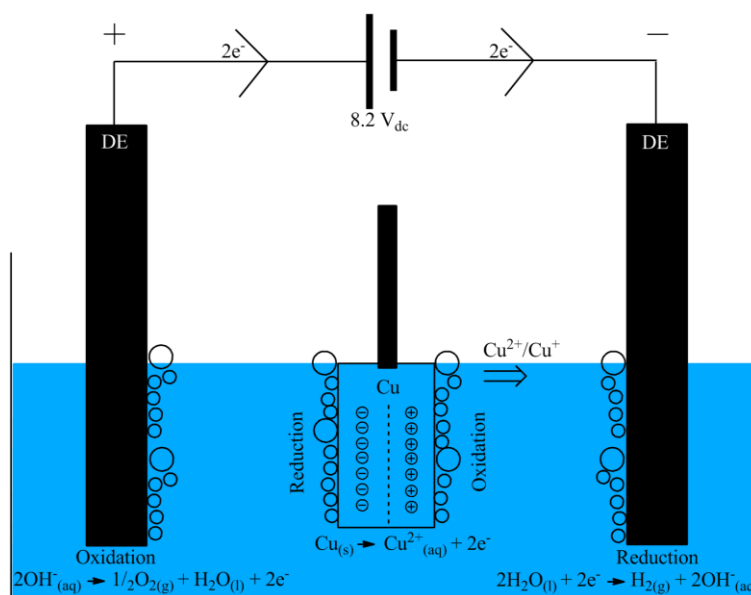
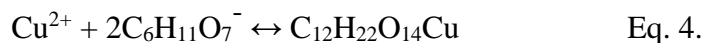


Fig. 12. Redox reactions inside bipolar reactor filled with Cu gluconate associated with generation of Cu ions for Cu_2O production at 80°C . $\text{H}_2(\text{g})$ generated by the reduction of H_2O (cathodic reaction) while $\text{O}_2(\text{g})$ is generated by the oxidation of OH^- (anodic reaction).

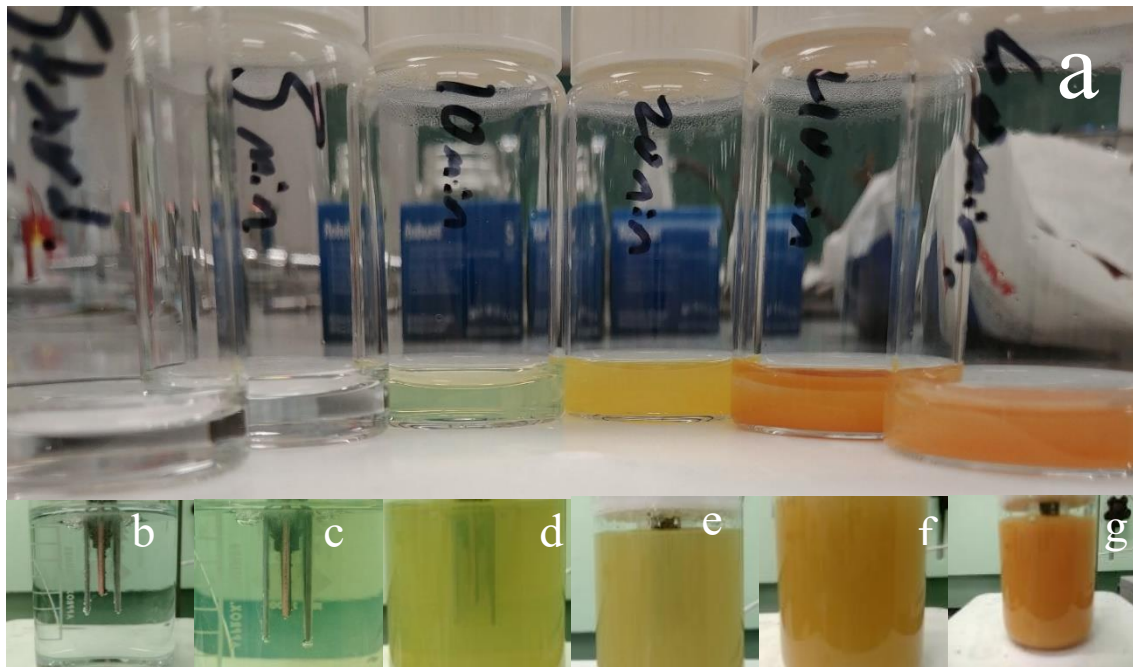


Fig. 13. Progression of the generation of Cu_2O . (a) Progression of the synthesis from start (0 min) until the shut off period of 60 min via removal of solution at specified time intervals. (b-g) Progression of the reaction remaining inside the bipolar cell at times; 0, 5, 10, 20, 40, 60 min respectfully.

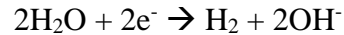
3.1.2. Minimum Change in Voltage (ΔV Minimum)

No previous reports discuss the minimum potential that is required for the reaction to move forward to produce Cu_2O . However, based on published papers for other metal oxides (e.g., ZnO), it can be safely assumed that the paired reaction for the oxidation of the metal species would be the reduction of H_2O . To

calculate the minimum required potential for the electrochemical processes is referred back to Eq. 1:

$$\Delta E_{elec} = E_{tot} \left(\frac{l_{elec}}{l_{channel}} \right) \quad \text{Eq. 1.}$$

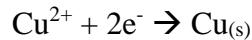
In the cell, the distance between the driving electrodes ($l_{channel}$) was 1.0 cm and the length of the bipolar electrode (l_{elec}) was equal to the thickness of the Cu plate (0.2 cm). Thus, to determine the ΔV_{min} only the difference between the two redox reactions (ΔE_{elec}) is required. As previously mentioned, the two redox reactions that were assumed to have occurred are the reduction of H₂O and oxidation of Cu. As such, this is complicated since the reaction for the reduction of H₂O is pH dependent, while the oxidation of Cu is assured not to be. As depicted, the two paired electrochemical reactions that were preferred for the formation of Cu₂O are depicted by Eq. 7 and Eq. 9, where the reduction of H₂O will take place in counter to the oxidation of the Cu plate. The potentials required to drive this reaction forward are determined in Eq. 8 and Eq. 10. By plugging Eq. 8 into Eq. 11 as E_{red} and Eq. 10 into E_{ox} , we are able to calculate the final value for ΔE_{elec} .



Eq. 7.

$$E = -59.2 \text{ mV} \cdot \text{pH}$$

Eq. 8.



Eq. 9.

$$E = 0.34 \text{ V}$$

Eq. 10.

$$\text{Cell potential} = E_{\text{red}} - E_{\text{ox}}$$

Eq. 11.

$$\text{Cell potential} = (-0.402) - (0.34) = -0.74 \text{ V}$$

Eq. 12.

The concentration of the solution that the reaction occurred in is 19.2 mMol potassium gluconate, which was tested via a pH meter in the lab (Science workshop 500 interface). The determined pH of the solution was 6.8; thus, the redox potential for the reduction of H₂O was -0.402. When the equation is rearranged and solved, the following is obtained:

$$E_{\text{tot}} = \Delta E_{\text{elec}} \left(\frac{l_{\text{channel}}}{l_{\text{elec}}} \right)$$

Eq. 13.

$$E_{\text{tot}} = (-0.74 \text{ V}) \left(\frac{1.0 \text{ cm}}{0.2 \text{ cm}} \right)$$

Eq. 14.

$$E_{\text{tot}} = -3.7 \text{ V}$$

Eq. 15.

-3.7 V is the theoretical minimum voltage that can be applied to allow the reaction to move forward. However, it is common in electrochemistry that a potential above the theoretical minimum is needed to account for changes to the system (e.g., concentration of electrolyte, temperature), so a common practice is to apply a 10% excess to compensate for any ohmic drop in the system. Colour change and/or bubble formation was used to determine if the reaction took place. This is based on the colour of the solution (Fig. 13) because the appearance of bubbles (i.e., electrolysis) will occur with or without the oxidation of Cu.

3.2. Effect of Synthetic Conditions

Initially, calcium gluconate (i.e., a complexing agent) and sodium hydroxide (NaOH) (i.e., used to adjust the pH) were used for the synthesis of Cu_2O . Calcium gluconate was originally introduced into the system as the literature pointed to the possibility of utilising this complexing agent to lessen the required voltage by depolarizing the electrode, which would then subsequently reduce the generation of H_2 gas. This also led to the possibility of the gluconic acid acting as a complexing agent to prevent the Cu^{2+} ions from forming $\text{Cu}(\text{OH})_2$. This was later replaced with potassium gluconate due to the formation of calcium carbonate (CaCO_3) impurities, which will be discussed later. The NaOH, used to adjust the pH from the Frost diagram (Fig. 14), in aqueous conditions, Cu_2O is less stable as compared to Cu^{2+} compounds. As such, Cu^+ will disproportionate to Cu^{2+} and Cu metal. However, with the addition of NaOH to increase the pH to more basic conditions, Cu_2O can become more stable and easier to obtain. As observed in the Pourbaix diagram, Cu_2O is expected to form in a narrow band of voltage at a pH above 4.

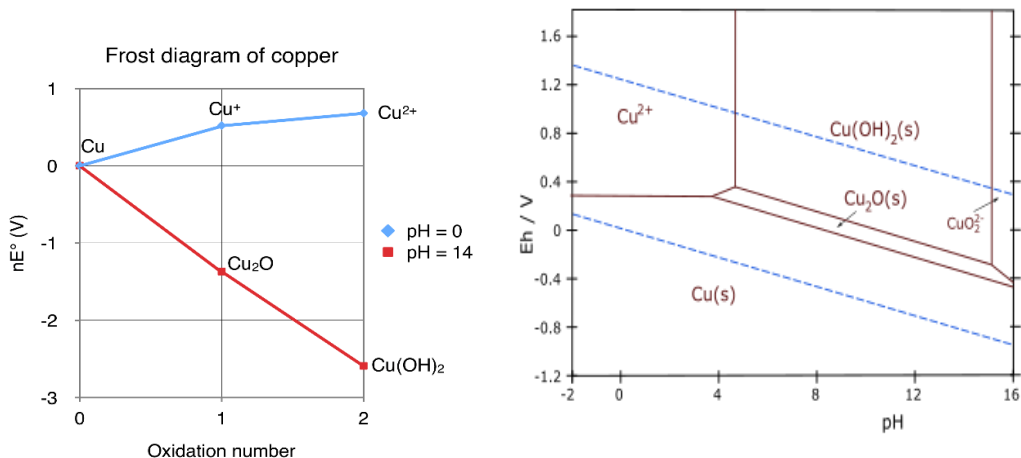


Fig. 14. Depicting both the Frost and Pourbaix diagram for Cu species.

3.2.1. Effect of Applied Potential

The main altered parameter of the synthesis conditions was the applied potential. The morphological and electrical properties were impacted by the applied potential. The applied potential ranged from 4.5 V – 8.0 V. The low end of the voltage range was determined via experimental observation of minimal V for which an appreciable amount of product was obtained. The sample was capable of being synthesized at all increasing potentials therefore, the potential limit was set to 8.0 V to maintain the sample size capable of determining the potential impact but to fit within the thesis.

3.2.2. Effect of Time

In order to observe if any impact would occur by altering the time of the synthesis, the 4.5 V sample was grown for a total of 3 hours (i.e., this was three times longer as compared to other samples). The 4.5 V sample was chosen to

observe if the time effect would result in a morphological change as the electric field was changed. The only observed change was an increase in the size of the particles, which will be discussed in section 5.1.

3.2.3 Effect of pH

The pH of the solution was also considered as a variable of interest that could potentially influence the properties of Cu_2O . In the literature, the effect of pH has been noted to have an impact on two major factors: the type of semi-conductivity and the strength of the generated photocurrent. Regarding the type of semi-conductivity, as previously mentioned, the N-/P-type nature of Cu_2O is dependent on the types of defects that are present in the cuprite lattice structure. One sample (i.e., 7.0 V) was repeated twice under two different pH conditions to investigate whether there was any influence of pH. One sample provided a powder product and was prepared at a pH of 5.4 by adjusting pH with dilute acetic acid (CH_3COOH). The other sample was adjusted to a pH of 3.0 and provided no powder. Instead, this sample resulted in the generation of a thick, red Cu_2O layer on the surface of the Cu electrode. To keep the comparisons, only synthesis conditions that yielded a powder and Cu plate deposition were characterized and tested.

3.3. Yield

Yields are extremely difficult to obtain in a bipolar electrochemical cell. When working in a system of low conductivity, it can be safely assumed that all or almost all current runs through the BPE due to the presence of a path of less

resistance as compared to the surrounding solution. However, the set up used for the experiments is highly conductive for a bipolar set-up due to the addition of potassium gluconate. Therefore, an attempt at obtaining a yield would require two assumptions. First, the current used for the Faraday's law (Eq. 16) calculation would need to be assumed and multiplied by a percent of current passing through the BPE; therefore, without a method for monitoring the amount of current through the BPE, yield calculations become impossible. Second, significant passivation of the BPE occurs, causing a hinderance on the product generation due to significant oxide generation on the surface; thus, it would need to be assumed that the passivation layer does not hinder the generation of the product.

$$m = (nFQM) \quad \text{Eq. 16.}$$

Faraday's law, as presented above, is defined as: (m) is the mass of electrode lost, (Q) is the average charge across the synthesis time, (F) is Faraday's constant, (M) is the molar mass of the material, and (n) is the number of electrons involved in the reaction. The mass obtained would be the theoretical yield. By determining the mass of product produced, we could then potentially calculate the % yield.

4.0. Morphological Studies Across Cu₂O Samples

Morphological comparisons across samples were completed by a combination of transmission electron microscopy (TEM) and SEM (Fig. 15 – 19). TEM provides detailed 2D, top-down, high resolution images of small particles and can be paired with SEM's 3D imaging to provide a clearer picture. However, with the size of the particles and the tendency to agglomerate, exact shapes were hard to determine. Therefore, estimations as to the shape of the material had to be made.

4.1. Effect of Applied Potential

An in-depth investigation into the effect of the applied potential and, therefore, the applied electric field, was conducted with the main objective of determining its impact on the bipolar electrochemical synthesis of Cu₂O. All samples were prepared at temperature (80°C) and concentration (19.2 mMol potassium gluconate), with a single Cu plate and varying applied potentials (i.e., 4.5, 5, 6, 7, and 8 V) for one hour. All samples were examined following their collection (10 mg), immersed in 10.0 mL ethanol, sonicated for one hour prior to analysis at UNB's microscopy laboratory. There, the samples received an additional round of sonication prior to deposition onto a nickel (Ni) grid (i.e., TEM) or onto a piece of atomic smooth glass for a clean background (i.e., SEM). Fig. 15 shows the observed shapes of 4.5 V-1H sample vs the 8.0 V sample. These two samples were chosen because 4.5 V show the only difference in structural agglomeration potentially resulting due to the material having higher

index facets which induced the agglomeration into a different preferred orientation [51]. However, no determination of the individual particles was possible due to resolution and size effects.

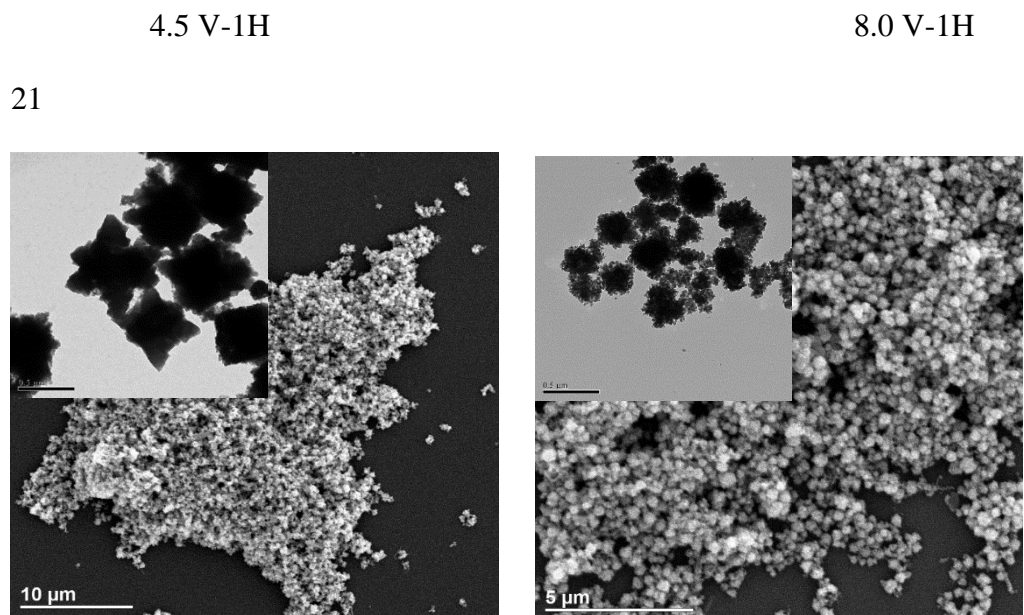


Fig. 15. SEM image with corresponding TEM insert shows the structure of Cu₂O obtained at 4.5 V and 8.0 V.

4.1.1. Applied Potential with Surfactant

Following the observations of section 4.1, an attempt at separating the particles post-synthesis was conducted with polyvinyl pyrrolidone (PVP), hexamethylenetetramines (HMT), sodium dodecyl sulfate (SDS), and centrimonium bromide (CTAB). By sonication with surfactant, the intended effect was to separate the particles by reducing the surface energy that was associated to the small particles, which is known to induce agglomeration by covering the particles. Shown here are the resultant TEM images from HMT. As the other surfactants did not appear to have any impact, investigations are still

ongoing regarding how to separate these particles. HMT appeared to cause either some separation of the individual particles or decomposition, which induced the appearance of holes. Further investigation was not conducted due to the continuance of severe agglomeration (Fig. 16).

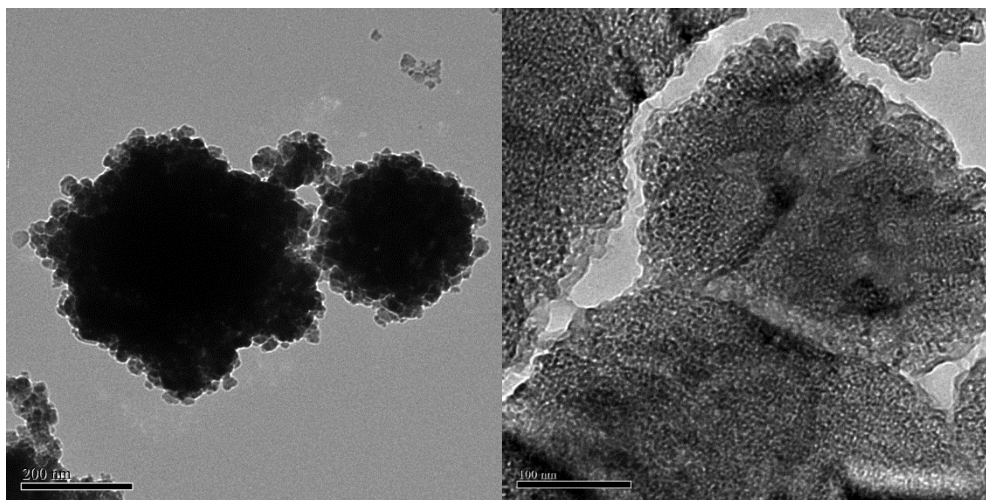


Fig. 16. TEM of Cu_2O after sonication without HMT surfactant (left) and with HMT (right).

4.1.2. Effect of Time

To further investigate the influences of the synthetic process on the morphological and photocatalytic properties, time was considered for one sample: 4.5 V. As seen in Fig. 17, no significant change in morphology was observed between 4.5 V-1H and 4.5 V-3H.

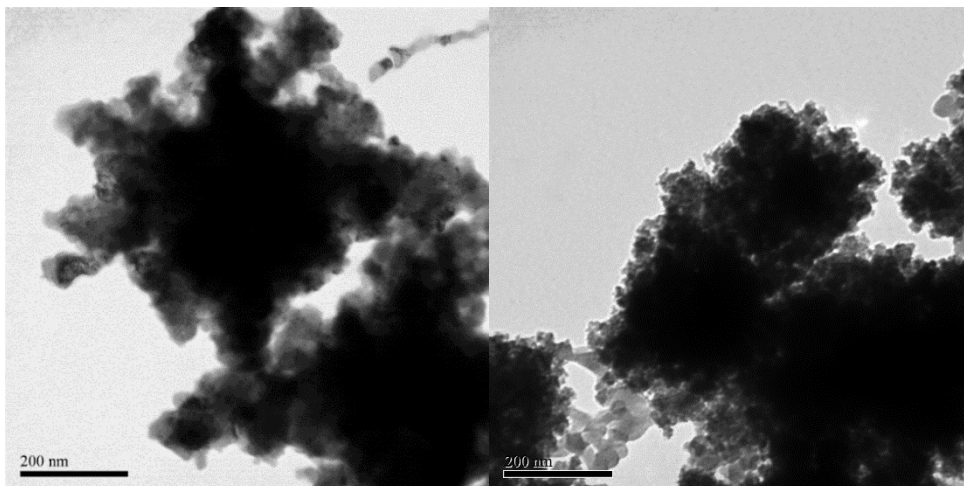


Fig. 17. TEM images of both 4.5 V-3H (left) and 4.5 V-1H (Right) with star like agglomerates.

4.1.3. Effect of pH on Morphology

As mentioned earlier, the pH of the solution can have a large impact on the material synthesized both by impacting the voltage applied and by effecting the properties/terminating ions. Therefore, it is decided to use one voltage (7.0 V) at two different pH's to look for any influence on morphology. However, no structural impact appeared to have occurred, as shown in Fig. 18. The material appears to have similar agglomerations and structure to all samples prepared at 5.0 V and above, as exhibited in the insert of Fig. 15.

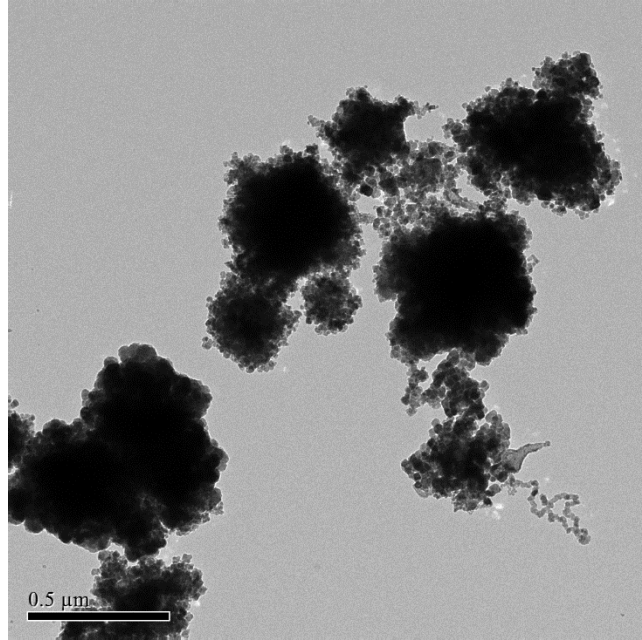


Fig. 18. TEM image of sample synthesized at 7.0 V with a pH of 5.4.

4.1.4. Substructure Generation

Additional TEM imaging was performed in Germany in order to obtain higher resolution images. The findings determined by the TEM images were quite surprising as the crystal lattice appeared to have multiple orientations in the same crystal, as depicted in Fig. 19. The red and blue circled areas depict the crystal lattice with uniform directionality; however, these were in different orientations with respect to each other. The area that is circled in green illustrates multiple crystal lattice's that are facing multiple directions, all within the size range of 2-3 nm. Fig. 20 represents a zoomed in image of the green circled area for the 7.0 V sample. This generation of substructures could potentially present issues depending on if the additional structures provoke grain boundary current

leakage. Finally, as indicated by the TEM of all the samples, the prevalence of the substructures decreased as the applied potential increased; therefore, the substructures are expected to have a minor contribution to the higher potential samples. Finally, where the substructures occurred more frequently in the lower potential sample, this suggests that the reduced concentration of Cu species may influence the formation of smaller Cu_2O particles.

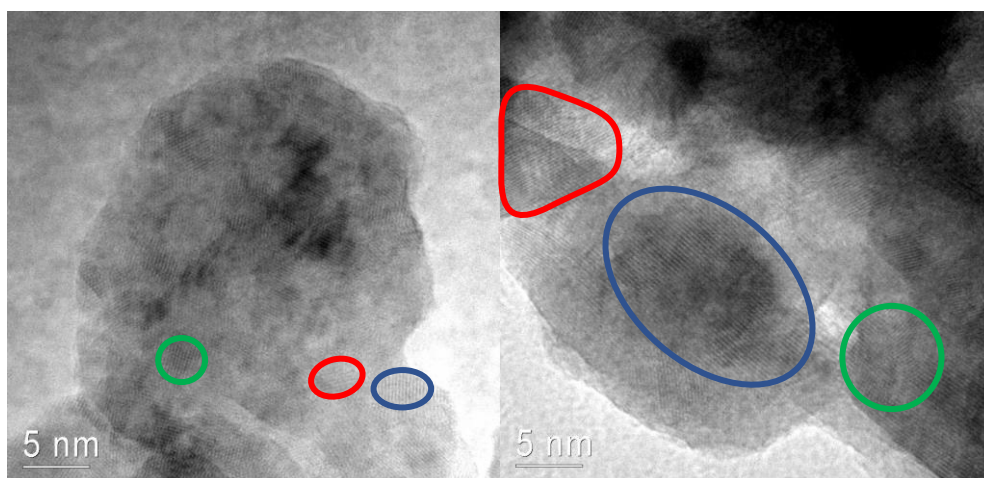


Fig. 19. Cu_2O TEM images indicating substructure generation 4.5 V (Left), 7.0 V (Right).

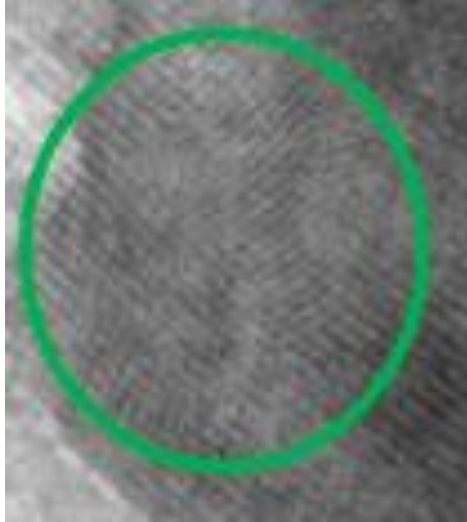


Fig. 20. Enlarged image of multi-crystal lattice section (7.0 V)

5.0. Characterization

Cu₂O samples were characterized by various methods (e.g., XRD, XPS). However, the initial synthetic route that led to the current synthesis route was not mentioned, so it will be briefly discussed here in comparison to the final synthesis conditions. The initial conditions consisted of calcium gluconate (i.e., complexing agent) and NaOH (i.e., utilised to adjust the pH). Comparisons of the initial synthetic route as compared to the final synthesis were completed via XRD.

5.1. X-Ray Diffraction

X-ray diffraction was completed for all samples with the exception of the sample synthesized at pH 5.4 with an applied potential of 7.0 V, as the technician determined that the material did not have a significant enough volume for proper analysis. All samples were compared to a commercial sample that was acquired from Sigma Aldrich. The samples were identified based on a Cu₂O reference card JCPDS #00-005-0667 and contained the diffraction peaks of 100, 111, 200, 220, 311, and 222 [52]. These peaks indicated a cubic lattice structure. The largest peak belonged to the 111-diffraction peak, suggesting that the Cu₂O was grown in a 111 preferred facet orientation. The original synthesized material, however, did not work well. The use of calcium gluconate resulted in severe impurities as this complexing agent generated two different CaCO₃ lattices, as demonstrated in Fig. 21.

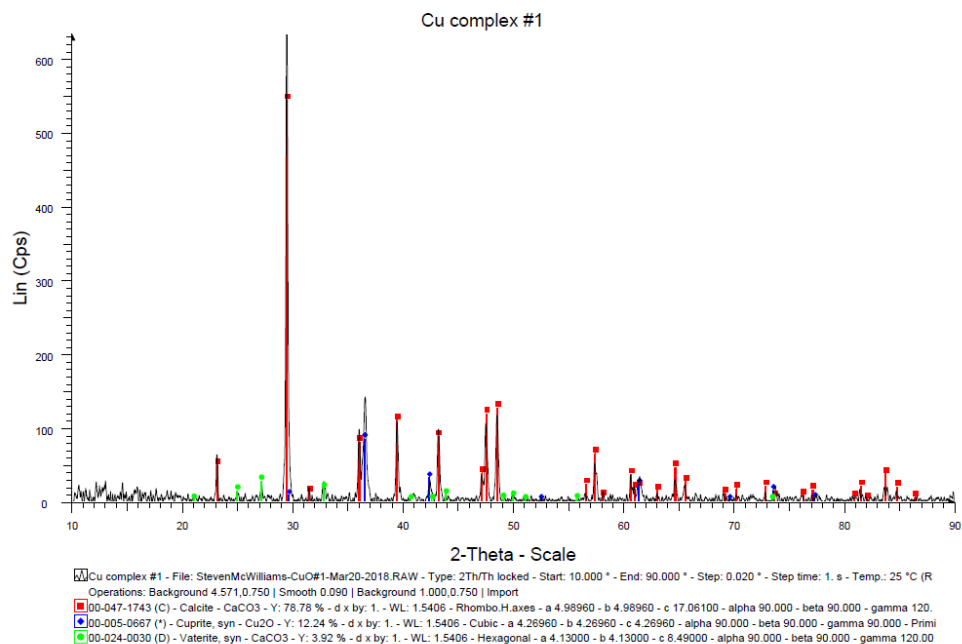


Fig. 21. XRD of Cu₂O formed via bipolar electrochemistry utilizing calcium gluconate as a complexing agent.

Based on the peak intensities, the issue was so problematic that more impurity than product existed, as exhibited by the intense calcite peak in Fig. 21. The initial setback of CaCO₃ formation pushed us toward looking for a way to avoid CaCO₃. The first attempt included degassing the solution over a period of one hour with N₂ to remove excess carbon dioxide (CO₂). This, however, did not provide any change in the XRD results. Therefore, an alternative gluconate that could be utilised as a complexing agent to avoid introducing calcium (Ca) into the system was sought after. Potassium gluconate contained the gluconic species that was needed for complexing, without the drawback of CaCO₃ due to the presence of the K ion. Furthermore, potassium carbonate (K₂CO₃) is soluble under aqueous conditions, which means that if it is formed, it should not

precipitate with the Cu_2O . As evidenced by Fig. 22, the replacement of calcium gluconate with potassium gluconate was significant as it allowed for us to successfully progress in our research.

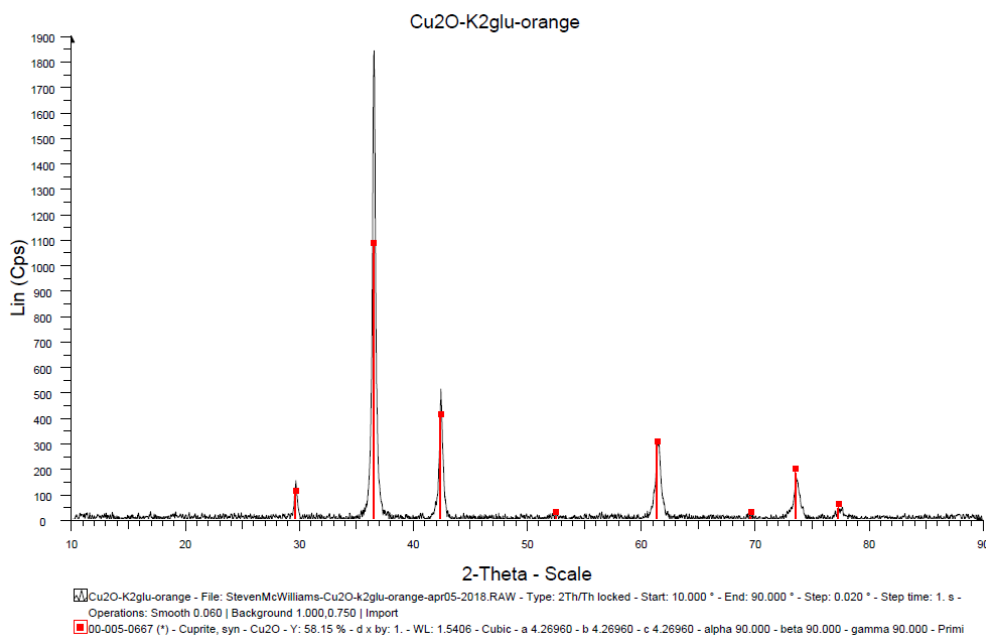


Fig. 22. XRD of cuprous oxide synthesized with potassium gluconate at pH 6.8 with an applied potential of 8.0 V.

Both the calcium gluconate and potassium gluconate samples, however, provided no indication of the presence of Cu metal or Cu^{2+} oxide inside of the sample. As the wet chemical synthesis of Cu_2O provided Cu powder by-product, Fig. 23. shows a sample previously synthesized using a wet-chemical methodology. This demonstrates that XRD could determine the difference between Cu in its different states.

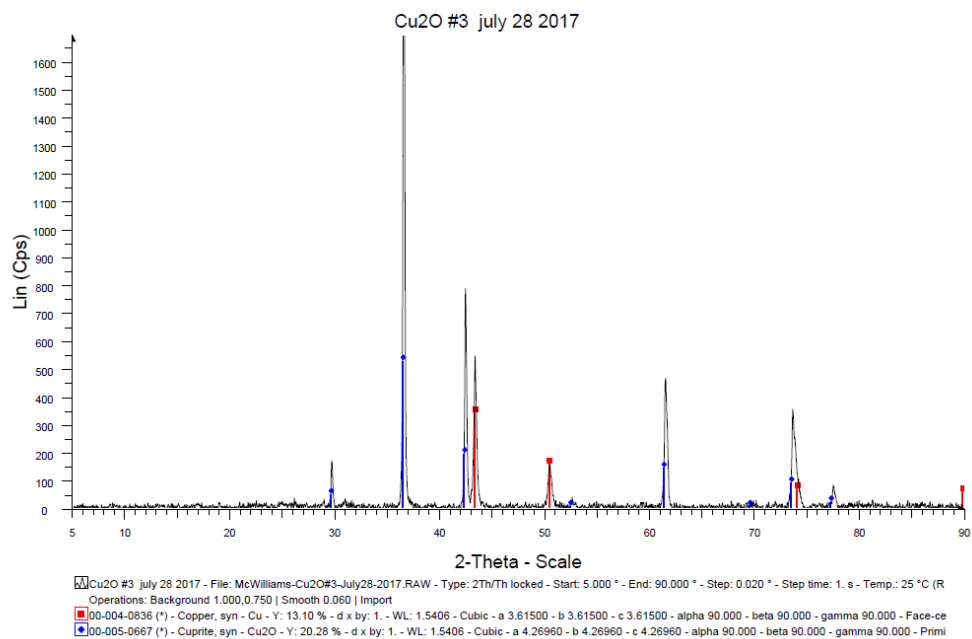


Fig. 23. XRD spectrum of Cu₂O synthesized by wet-chemical route.

As it was possible to make Cu₂O without the potential for unwanted by-products, the next goal was removing any unrequired additives (i.e., NaOH) (Fig. 24). Removing NaOH from the synthesis appeared to have no impact on the XRD, except for a small change in the relative peak intensities between peak 311 and 220. Therefore, NaOH was removed to keep the synthesis both at a reduced cost for scaling up, as well as to maintain a greener synthesis.

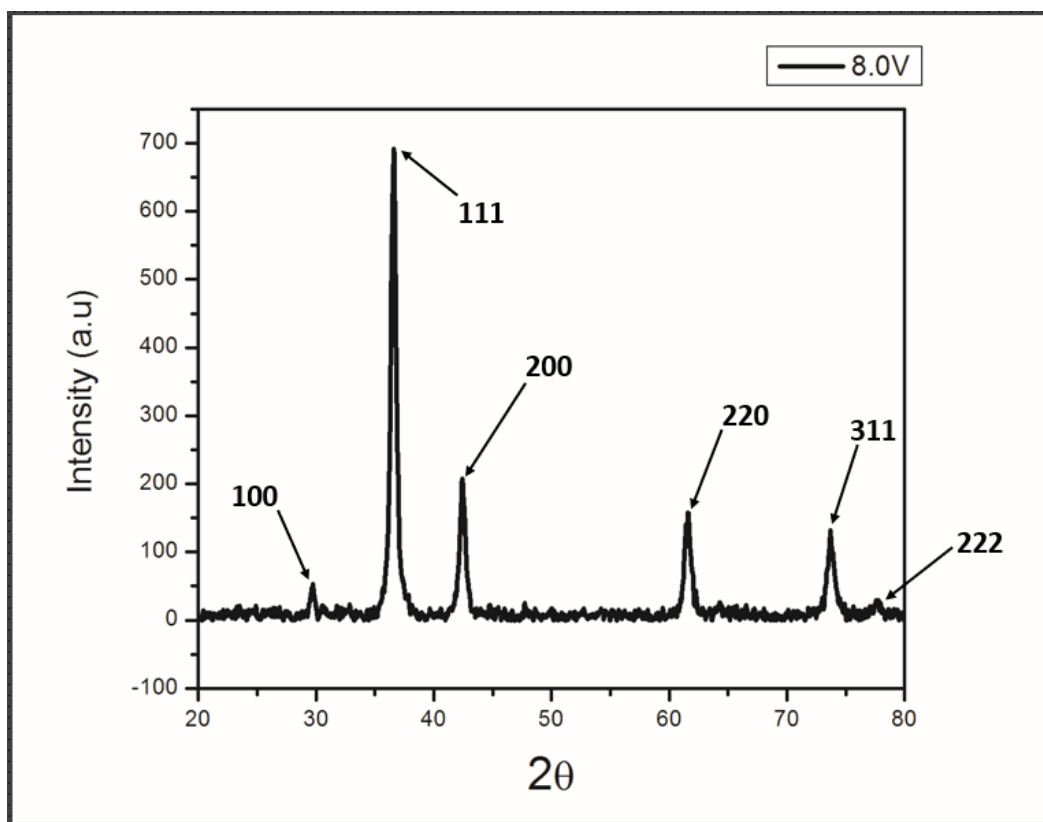


Fig. 24. XRD spectrum of Cu_2O synthesized at 8.0 V for one hour at pH 6.8 at 80°C .

Upon reaching the goal of reducing the amount of chemicals that were involved in the synthetic process, attention was then turned to modifying various conditions. XRD diffractograms were obtained for all samples and were compared to a commercially bought sample from Sigma Aldrich (Fig. 25.). Observing the sections demonstrated in the inserts, it is determined that, as the voltage applied rises, the peaks of the XRD spectra were broadened. This can occur due to two possible reasons: strain and particle size. In order to investigate this, Debye-Sherrer equation (Eq. 17) was used to determine the crystallite size.

$$D = \frac{(0.9\lambda)}{\beta \cos\theta} \quad \text{Eq. 17.}$$

Where D is the size in nm, λ is the wavelength of X-ray radiation in nm (0.0154178), θ is the Bragg's angle in radians, and β is the full width at half maximum (FWHM) [53]. An average was taken across the most intense peaks to obtain the crystallite size. As can be seen in Table. 1, an expected trend resulted in a decrease in the crystallite size due to an increase in the applied potential. This is due to the increase in product generation rate, which could result in a larger abundance of product and a reduction in the size/crystallinity. The crystallite size was also calculated for the three-hour sample, which was hypothesized, and subsequently observed, to have a larger crystallite size due to the longer synthesis duration.

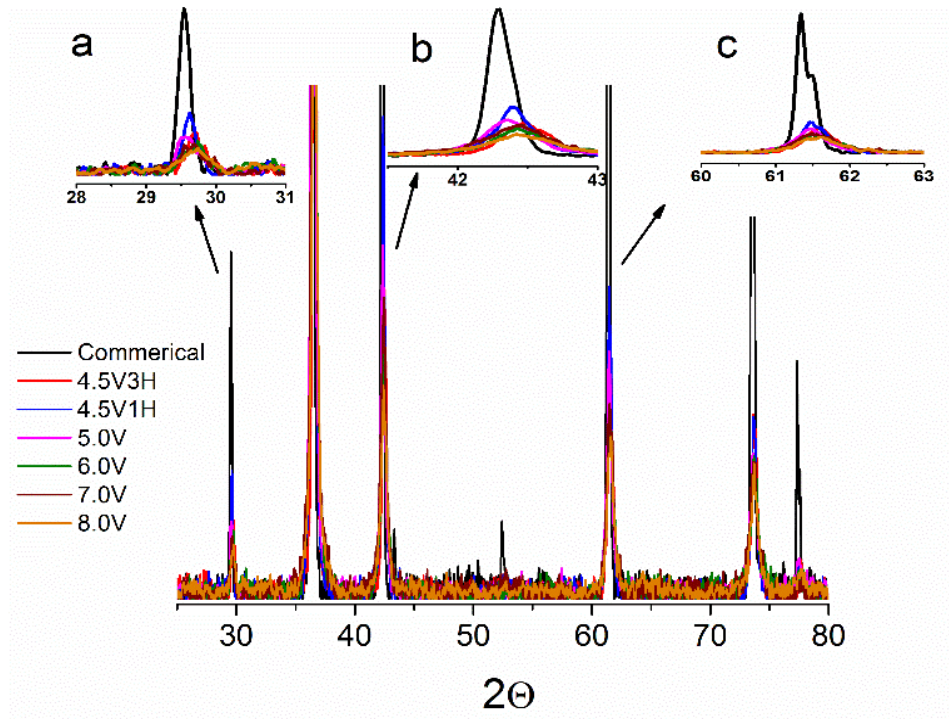


Fig. 25. Stacked XRD of all samples compared to commercial material.

Table 1. Refinement data collected from the Rietveld analysis of room temperature XRD for BPE-made Cu₂O. All samples showed very good correlation with the Cu₂O model (space group: *Pn-3m*, with atom positions for Cu of (0,0,0) and O of (¼, ¼, ¼). Parameter χ^2 is goodness of fit, R_{wp} is weighted profile, R_p is profile residual, and a is the lattice parameter in Angstroms (Å). Crystallite size is also represented with respect to applied potential and time.

Parameter	4.5 V-3H	4.5 V-1H	5.0 V	6.0 V	7.0 V	8.0 V
χ^2	1.166	1.319	1.308	1.328	1.420	1.296
R_{wp} (%)	10.84	10.03	9.94	10.46	10.14	10.42
R_p (%)	8.51	7.95	7.79	8.01	7.93	8.07
a (Å)	4.2641	4.2640	4.2671	4.2609	4.2621	4.2621
Cell Vol (Å ³)	77.53	77.53	77.69	77.36	77.42	77.43
Cu-O bond length (Å)	1.84642	1.84637	1.8477	1.8450	1.8455	1.8457
Cu-O-Cu bond angle (°)	109.471	109.471	109.471	109.471	109.471	109.471
Crystallite size (nm)	27.09	21.69	20.32	16.18	15.64	14.54

Rietveld analysis (Fig. 26 - 31) was performed for the diffraction data collected for all materials using the GSAS suite of programs [54][55] and the model for Cu₂O proposed by Foo *et al.* (as taken from the ICSD) [56]. Refinements were performed for 20 variables which included lattice parameters, atom positions, zero-point, peak shape, and background. The background was modelled with 12 terms using a shifted Chebyshev polynomial function. The peak shape was modelled using the pseudo-Voigt function (type 2 in GSAS) described by Howard, and Thompson *et al.* [57][58]. The U_{iso} were not refined and fixed with a value of 1.00 ($U_i/U_e \cdot 100$) Å² since allowing them to refine

resulted in physically unrealistic values. Six spherical harmonic order (ODF) terms were also refined in a cylindrical geometry in order to mitigate surface roughness effects introduced by preparation of the sample for X-ray diffraction analysis. In all cases, the Texture Index was close to 1, indicating that the sample is randomly orientated. Refinement data are given in Table 1, with the refinement profiles given in Fig. 26 - 31. All materials showed an excellent fit to the proposed model. Peak shape was difficult to refine due to the quality of the data collected. More reliable refinements providing information about size and strain could be achieved with higher quality data. It is also noted that there is only a very small difference in the lattice parameters between the samples. It is difficult to be able to comment if this is significant because of the quality of the data.

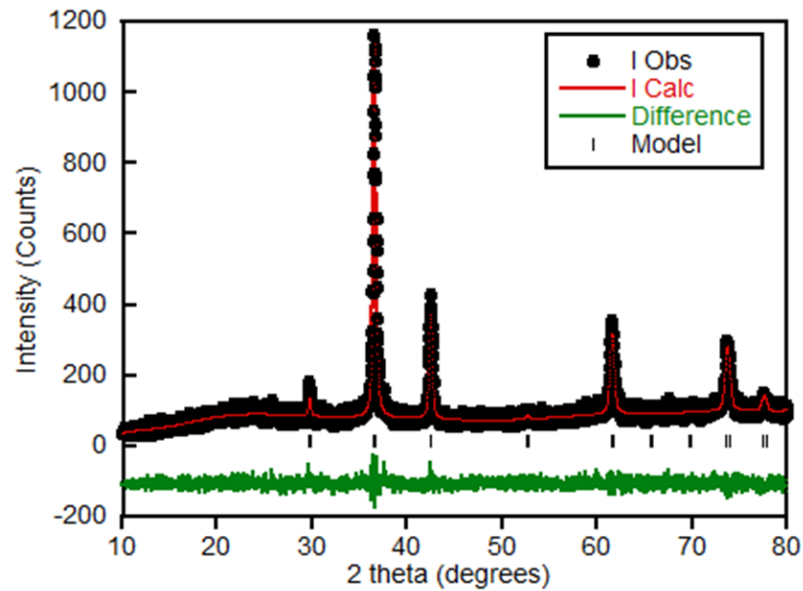


Fig. 26. Refinement profile for the Rietveld analysis of room temperature XRD data collected for 4.5 V3H fitted to the model proposed for Cu_2O by Foo et al. [56].

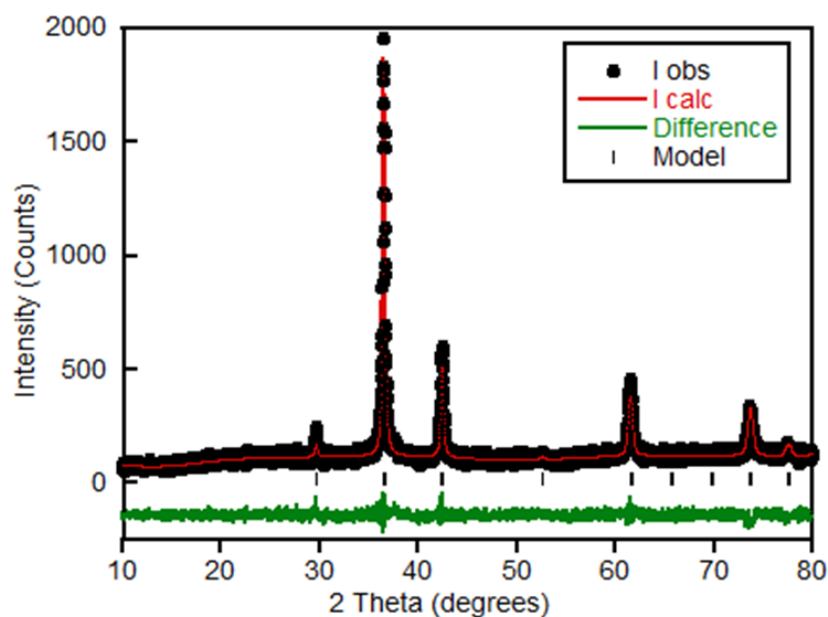


Fig. 27. Refinement profile for the Rietveld analysis of room temperature XRD data collected for 4.5 V1H fitted to the model proposed for Cu_2O by Foo et al. [56].

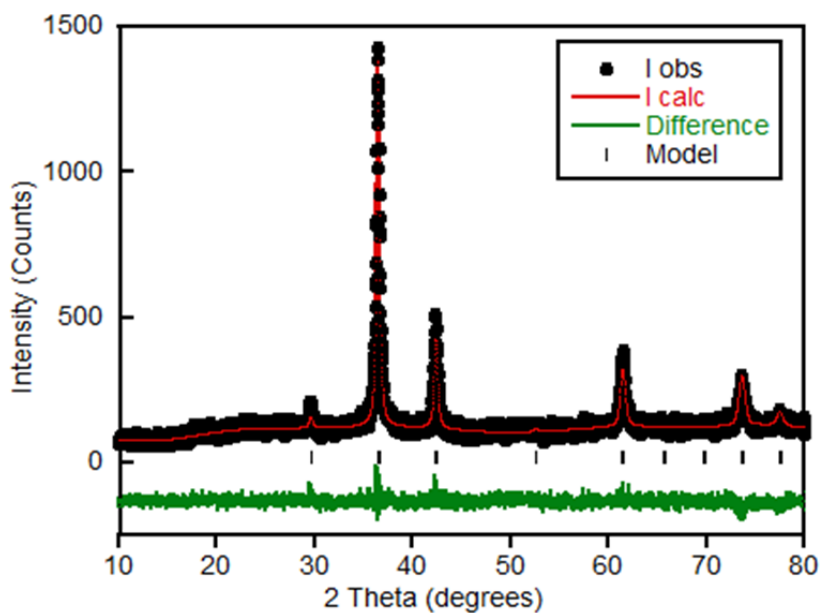


Fig. 28. Refinement profile for the Rietveld analysis of room temperature XRD data collected for 5.0 V fitted to the model proposed for Cu_2O by Foo et al. [56].

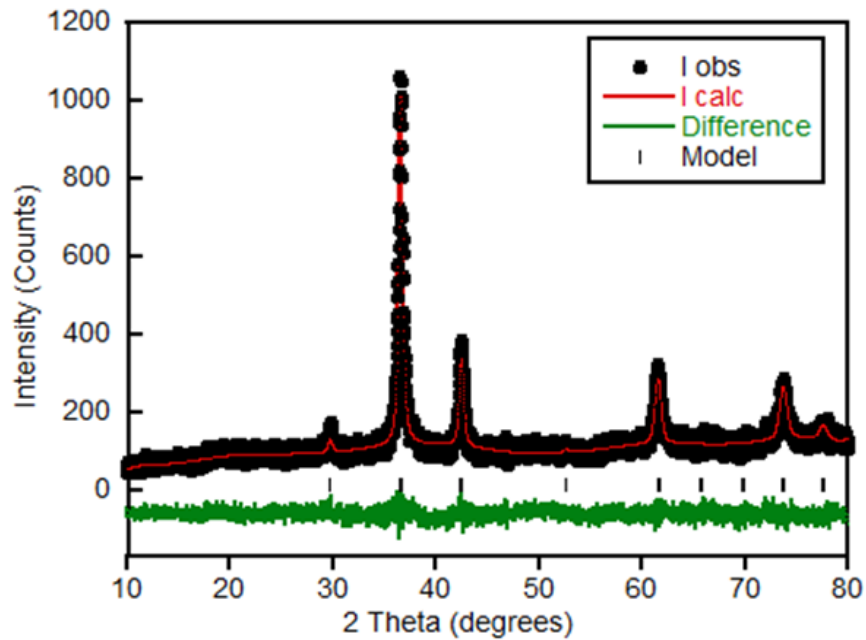


Fig. 29. Refinement profile for the Rietveld analysis of room temperature XRD data collected for 6.0 V fitted to the model proposed for Cu_2O by Foo et al. [56].

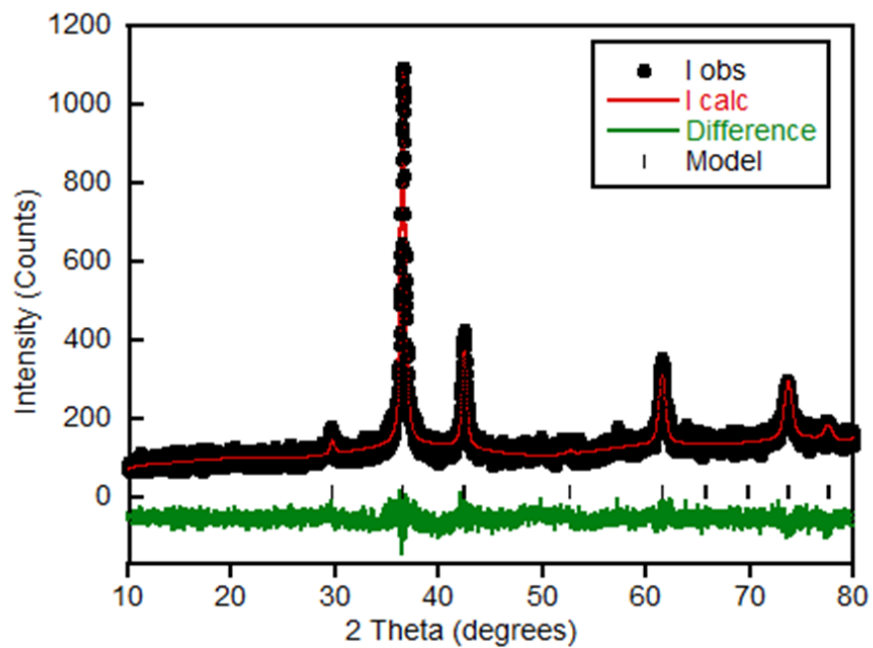


Fig. 30. Refinement profile for the Rietveld analysis of room temperature XRD data collected for 7.0 V fitted to the model proposed for Cu_2O by Foo et al. [56].

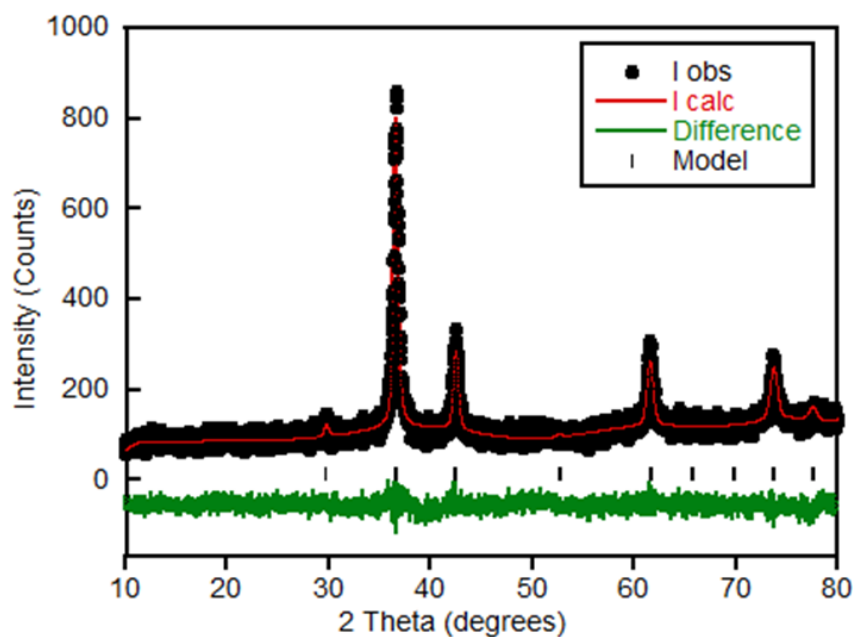


Fig. 31. Refinement profile for the Rietveld analysis of room temperature XRD data collected for 8.0 V fitted to the model proposed for Cu_2O by Foo et al. [56].

5.2 X-Ray Photoelectron Spectroscopy

Cu_2O samples were analyzed by XPS. Charge corrections were completed by the XPS technician at Dalhousie University. Fig. 32 represents the $\text{Cu}2p_{3/2}$ spectrum. Initial observation of this spectrum determined that the beginning stages of degradation had occurred on the surface of the Cu_2O samples, as represented by the formation of the $\text{Cu}(\text{OH})_2$ peak. Sample (4.5 V-1H, 7.0 V) and acidic (7.0 V – pH 5.4) all show CuO . It is hypothesized that this occurred to the non-acidic samples over the duration of time that they were exposed to air; however, no conclusion can be confidently made about the acidic

sample as the XRD was not completed prior to XPS analysis due to sample size limitations. Degradation of Cu_2O is demonstrated by the satellite peaks located at approximately 943 eV [59]; however, if the concentration is sufficiently low, the satellite peaks can be lost in the background of the spectrum.

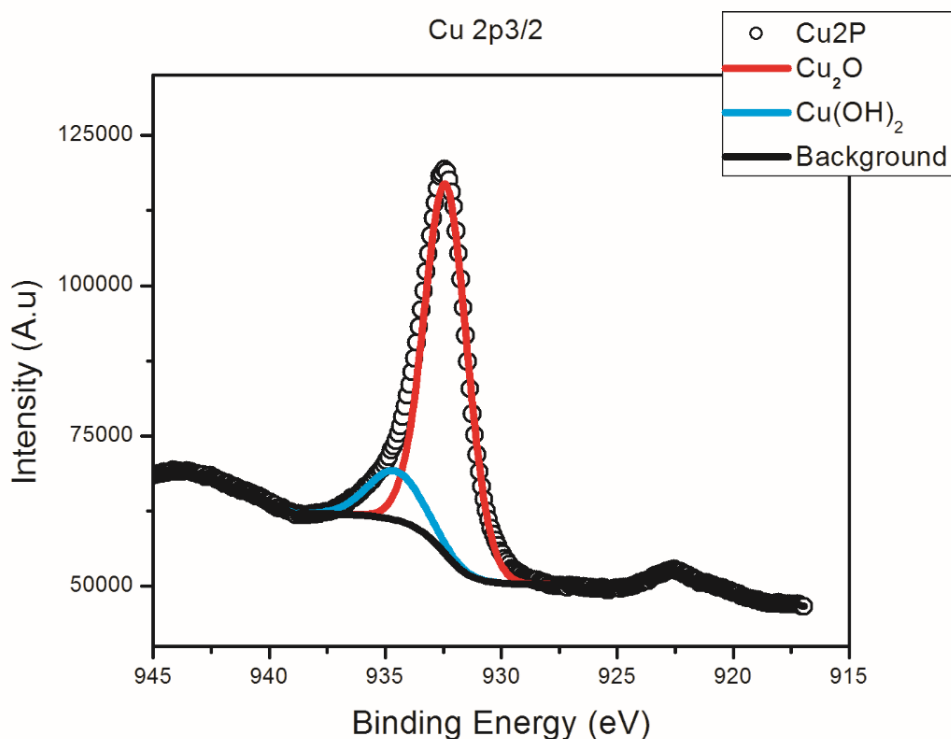


Fig. 32. XPS spectrum of Cu_2O 5.0 V sample with Cu $2p_{3/2}$ peak deconvoluted to determine individual peak contributions.

Further analysis occurred into the identification of Cu_2O , towards the location of two peaks: 933 eV and 952 eV. The peak at 933 eV represents the Cu_2O $2p_{3/2}$ peak, whereas the 952 eV peak represents $2p_{1/2}$. It was not expected that any satellite peaks would have been generated by Cu_2O due to the 3d band of Cu_2O being filled. In Fig. 33, the degradation peaks were removed, which enabled a better comparison of the Cu $2p_{3/2}$ peaks and their potential shifts with

respect to the commercial material. According to M. C. Biesinger [60], the peak's location should have been approximately 932.18 eV. Comparing the samples to that peak, it was noticed that the commercial material had a peak at 931.95 eV, while the synthesized samples were at 932.26, 932.04, 932.48, 931.47, 931.32, 931.73, and 931.552 eV. The shifts in the peak positions, with respect to the commercial material, suggests small changes in the local environment of the surface ions. That is, positive shifts imply the presence of more electronegative ions around the molecules and vice-versa for negative shifts.

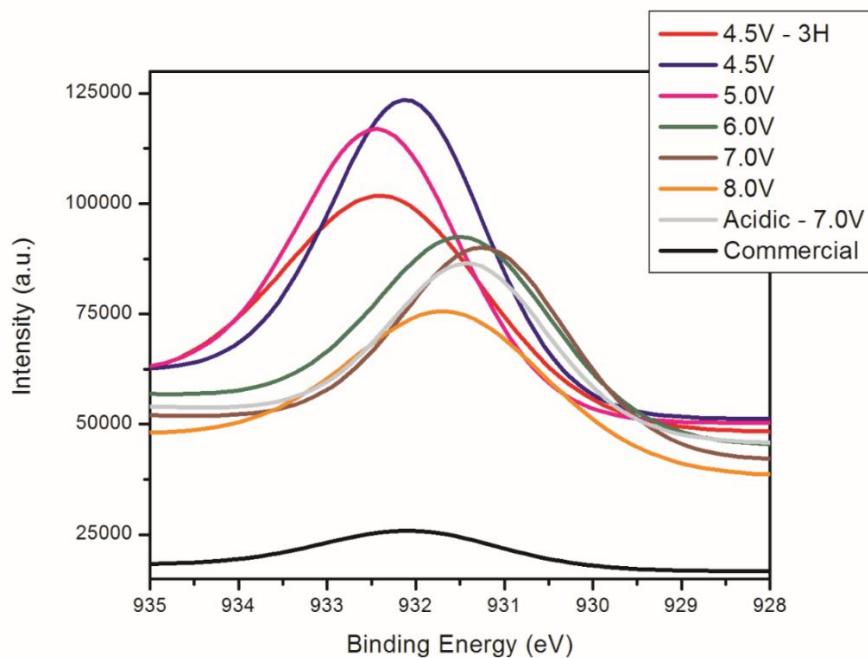


Fig. 33. Cu $2p_{3/2}$ peak for all synthesized samples representing shift compared to commercial material.

As demonstrated by Fig. 34, the peak position was determined to be evident at approximately 531.25 eV in the O1s XPS spectrum. This is interesting to note because the binding energy that have been reported for lattice oxide O1s

peaks range between 528.5 – 529.7 eV, while the binding energy of adsorbed O₂ ranges from 530.54 – 533.77 eV. This indicates that a large volume of the O₂ potentially exists as “adsorbed oxygen”. Therefore, the terminating ions could be Cu-based. However, alternatively, there are two potential values for O1s peaks. These two values are: 530.20 eV for lattice O₂ as compared to 531.57 eV for defective lattice oxide [55]. If defective lattice oxide O₂ exists inside the Cu₂O crystal structure, then the XPS peak is expected to shift towards higher eV values. However, due to the existence of surface oxidation and potential for adsorbed O₂, the defective O₂ lattice cannot be confirmed.

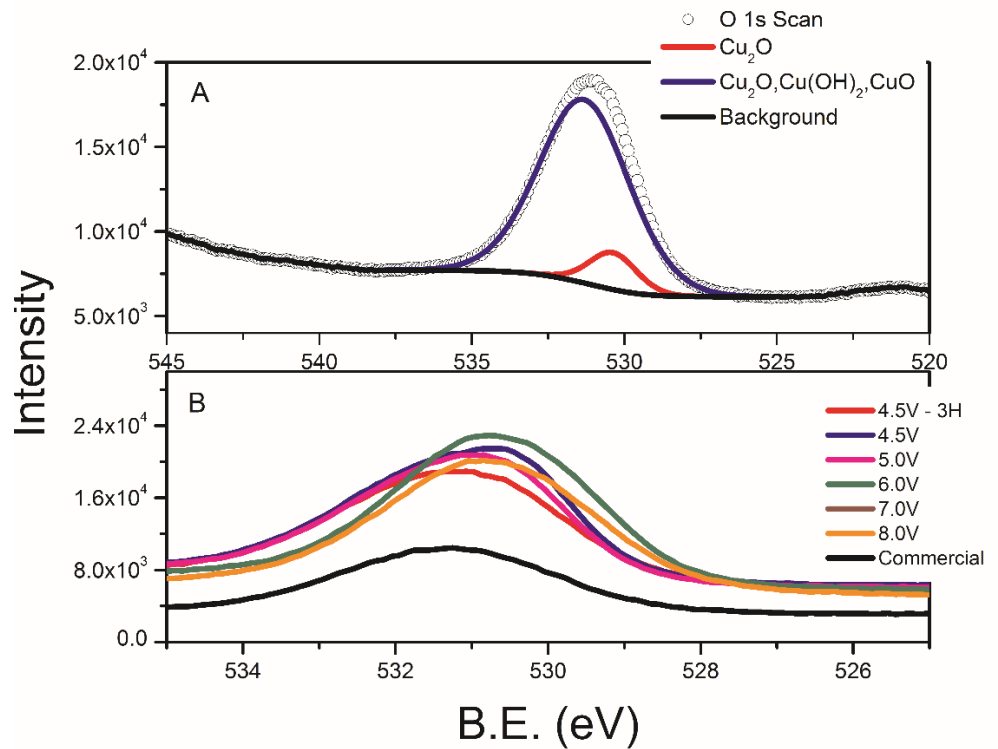


Fig. 34. O1s scan of 8.0 V sample depicting the possible presence of adsorbed O₂ (A). O1s scan of all samples overlaid (B).

6.0. Optical Studies

6.1. UV-Vis Diffusive Reflectance

UV-Vis diffusive reflectance spectroscopy was performed on all synthesized samples and compared to a commercial standard. Fig. 35 demonstrates the % reflectance obtained with respect to the wavelength. It should be noted that low % reflectance is indicative of high absorbance within the material. The samples were prepared on filter paper using a filtration system for a wide uniform dispersion. Also observed is that, within the UV region (< 380 nm), the commercial material had a minimum % absorption of 3.44%. The commercial materials rose significantly, reaching a maximum of 18.67% at 359 nm, and ended at 18% for the limit of the UV region (380 nm). These % reflectance for the commercial material are significantly higher as compared to the synthesized materials. The minimum observed % reflectance for the synthesized samples (Table 2), with increasing potential of 4.5 V – 8.0 V, indicated that a trend was present. This resulted in a slight increase of high energy absorbed wavelengths as they increased in potential, with a sharp increase at 8.0 V. The three-hour and acidic samples, however, had % reflectance values that were closer to the commercial material at 3.44% and 3.82%, respectively. Calculating the average across all samples in the UV region, the commercial material had an average % reflectance of 14.16%, while the synthesized samples ranged from 2.04% - 5.6%.

Table 2. Calculated average of % reflectance with respect to wavelength region per sample.

Sample	Com.	4.5 V-3H	4.5-1H V	5.0 V	6.0 V	7.0 V	8.0 V	7.0 V Acidic
UV	14.16	3.35	3.30	2.82	2.28	2.04	2.31	5.60
Vis	35.03	24.99	26.26	21.94	21.76	21.62	25.06	26.61
Overall	28.18	17.88	18.72	15.66	15.36	15.19	17.59	19.71

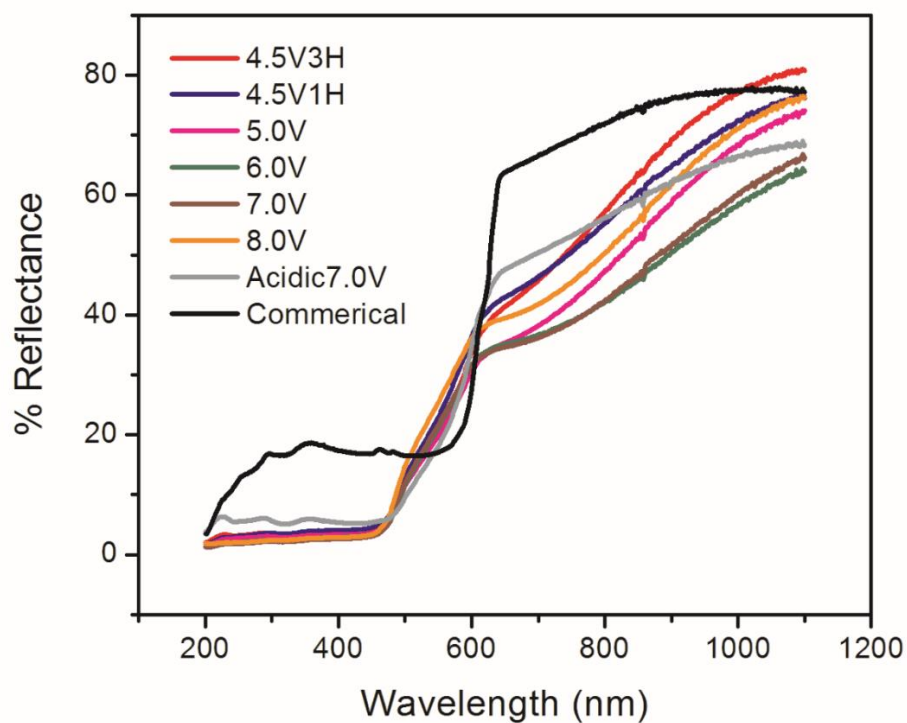


Fig. 35. % reflectance spectrum of all synthesized samples compared to commercial material.

As the synthesized samples approached 450 nm, their % reflectance began to rise steadily as compared to the commercial material. This caused the Cu₂O nanoparticles to have a higher reflectance at about 530 nm until 600 nm. This sharp increase was attributed to the band-gap of the material. The %

reflectance of the visible region demonstrated a close relationship between 5.0, 6.0, and 7.0 V, with a small increase at 8.0 V. To determine the band-gap, by using a Kubelka-Munk function Eq. 18. (Fig. 36), the % reflectance was converted into a Tauc plot. Where R is the absolute value of reflectance, F(R) is the absorption coefficient equivalent, K is the absorption coefficient, S is the scattering coefficient, R_{∞} is the diffusive reflectance of the film.

$$F(R) = \frac{K}{S} = \frac{1-R_{\infty}}{2R_{\infty}} \quad \text{Eq. 18.}$$

The band-gap of the material in Table 3 was determined by extrapolating the linear region of a Tauc plot to zero. The synthesized material has a band-gap that focused around 2.5 eV, with small changes hypothesized to have been caused by changes in their respective size (i.e., the observed increase in band-gap as particle size decreases) as compared to the commercial material at 1.95 eV. However, the standard value for Cu_2O is around 2.0 eV. This discrepancy was likely due to quantum effects, which are expected to occur on materials at the nanoscale. This quantum effect is commonly referred to as quantum confinement.

Quantum confinement has been explained in many ways. One way is that the confinement of the electrons is when they cannot move [61]. The consequence of this confinement of movement is the quantization of their energy and momentum, and the subsequent generation of discrete energy levels. These discrete energy levels only exist in nanomaterials and can contribute a widening effect to the band-gap due to the accessible energy level not being located at the

“bottom” of the conductive band or at the “top” of the valence band. This increase in distance between the two accessible energy states results in an increase in the energy for an electron to be excited to the conduction band.

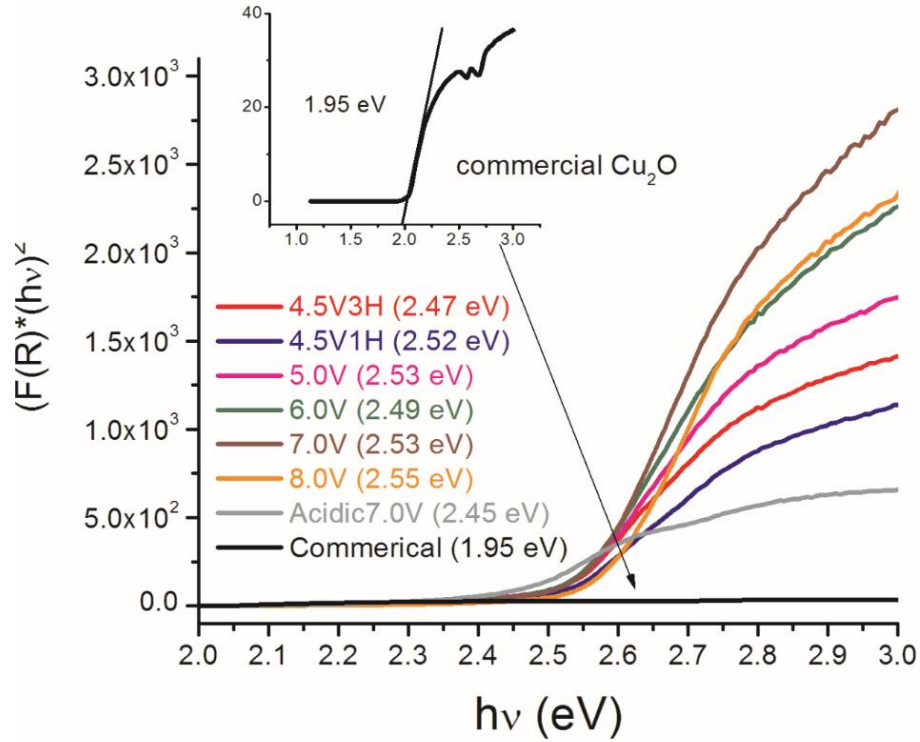


Fig. 36. Kubelka-Munk function for all samples compared to commercial material

Table 3. Band-gap values determined via Kubelka-Munk plot.

Sample	Com.	4.5 V-3H	4.5-1H V	5.0 V	6.0 V	7.0 V	8.0 V	7.0 V – Acidic
BandGap (eV)	1.95	2.47	2.52	2.53	2.49	2.53	2.55	2.47

7.0. Electrochemical Analysis

7.1. Mott-Schottky

In conjunction with photocurrent, M-S was used to determine the type of semi-conducting properties that each sample contained, as well as the carrier concentration (Table 4) and flat-band potential. The type of semi-conductor that a metal oxide is can be determined by the slope of the inverse capacitance squared versus the applied potential (Eq. 19), which is represented in Fig. 37. As the potential increases, the space charge capacitance (C_{sc}) increases for P-type material, resulting in a decrease for the inverse equation and a negative slope. Qualitatively, looking at the slope of the plot determines that Cu_2O is a P-type semi-conductor [62], which is later reenforced by the photocurrent. The flat-band potential was identified by extrapolating the linear region to zero with respect to capacitance. Finally, the carrier concentration was determined by taking the previously extrapolated linear region, determining the slope of the line, and setting it equal to Eq. 20 [63].

$$\frac{1}{C^2} = \frac{2}{\epsilon\epsilon_0 A^2 e N_A} \left(V - V_{fb} - \frac{k_B T}{e} \right) \quad \text{Eq. 19.}$$

$$\text{Slope} = \frac{2}{\epsilon\epsilon_0 A^2 e N_A} \quad \text{Eq. 20.}$$

Where, ϵ is the permittivity of free space, ϵ_0 is the dielectric constant, A is the area, e is the charge of an electron, and N_A represents the acceptor concentration. Unusually, the flatband potentials were recorded to be in the negative potential range; this has been stated in previous literature to be due to solvent effects.

However, what is observed is the gradual increase in the flatband potential towards more positive values, which is indicative of a decrease in the Fermi level (Fig. 38). A decrease in the Fermi level can indicate that a sample could comparatively have less electron density or a higher electron hole density. As observed in the samples, the flat band potential of the 8.0 V sample had the largest potential with respect to the one-hour trials. This matches well with the carrier concentration as it was also the largest. However, in comparison to the commercial product, all samples had significantly less bulk carrier concentrations.

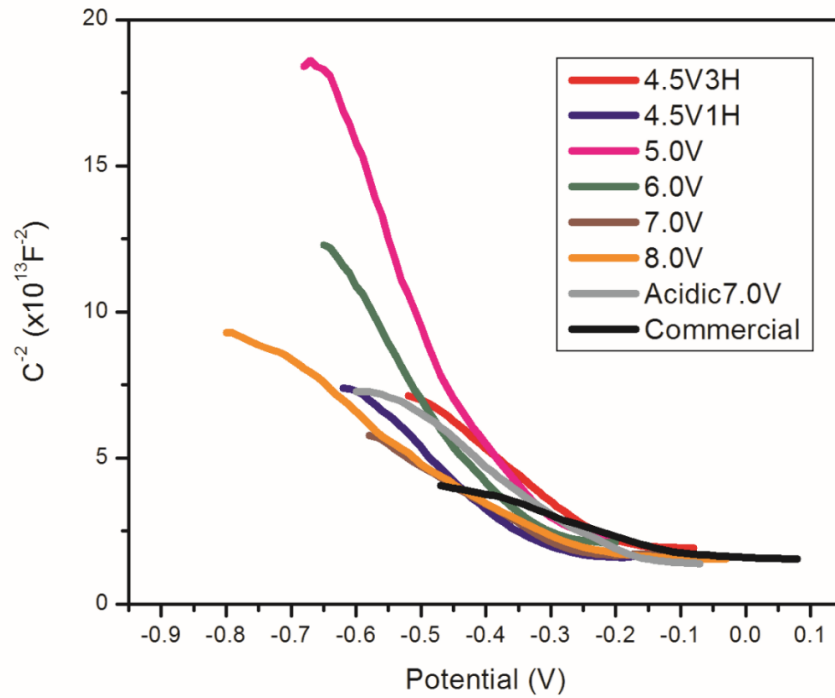


Fig. 37. M-S plot of samples obtained under dark conditions

Table 4. Calculated carrier concentrations determined by slope of M-S plot.

Sample	4.5 V-3H	4.5 V-1H	5.0 V	6.0 V
Concentration (cm³)	1.07*10 ¹⁷	9.15*10 ¹⁶	3.17*10 ¹⁶	5.23*10 ¹⁶
Sample	7.0 V	8.0 V	Acidic	Com.
Concentration (cm³)	1.47*10 ¹⁷	1.57*10 ¹⁷	1.1*10 ¹⁷	2.64*10 ¹⁷

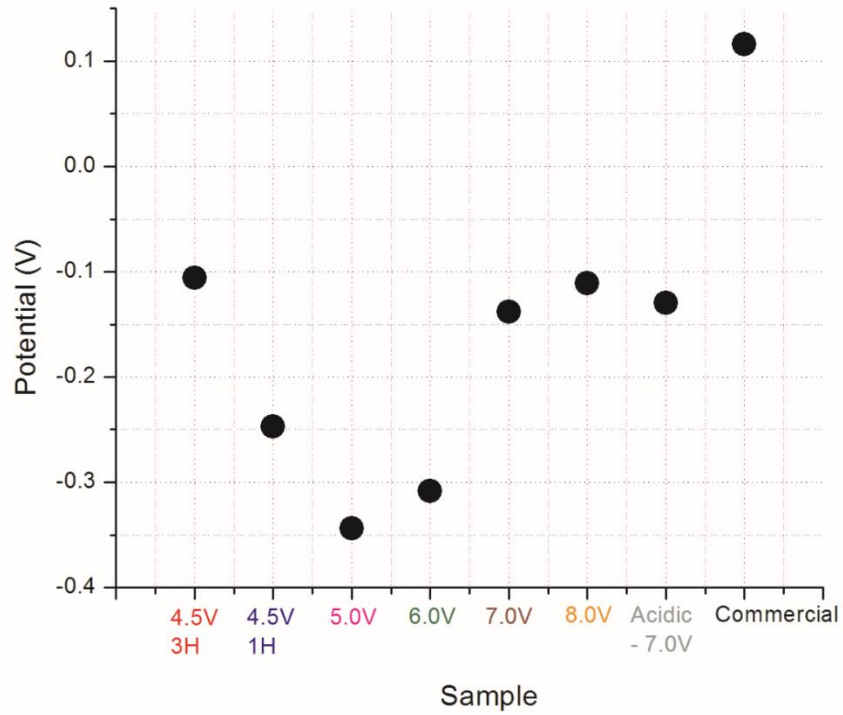


Fig. 38. Flat band potentials determined by x-int for each sample plotted vs. the sample name.

7.2. Carrier Lifetime

The carrier lifetime, also known as the recombination lifetime, is the average time that it takes to recombine the excess of minority carriers (i.e., electrons and electron holes). The electron lifetime can potentially influence the OCP, as well as an overall increase in photocurrent. This relationship implies that larger electron lifetimes and, therefore, a lower recombination rate is preferred. All samples were tested under the same conditions. Fig. 39 represents a phase versus log frequency plot, which is commonly denoted as a Bode plot. By taking the frequency at the peak maximum [64], Bode plots can be used to determine the carrier lifetime (as seen in Eq. 21).

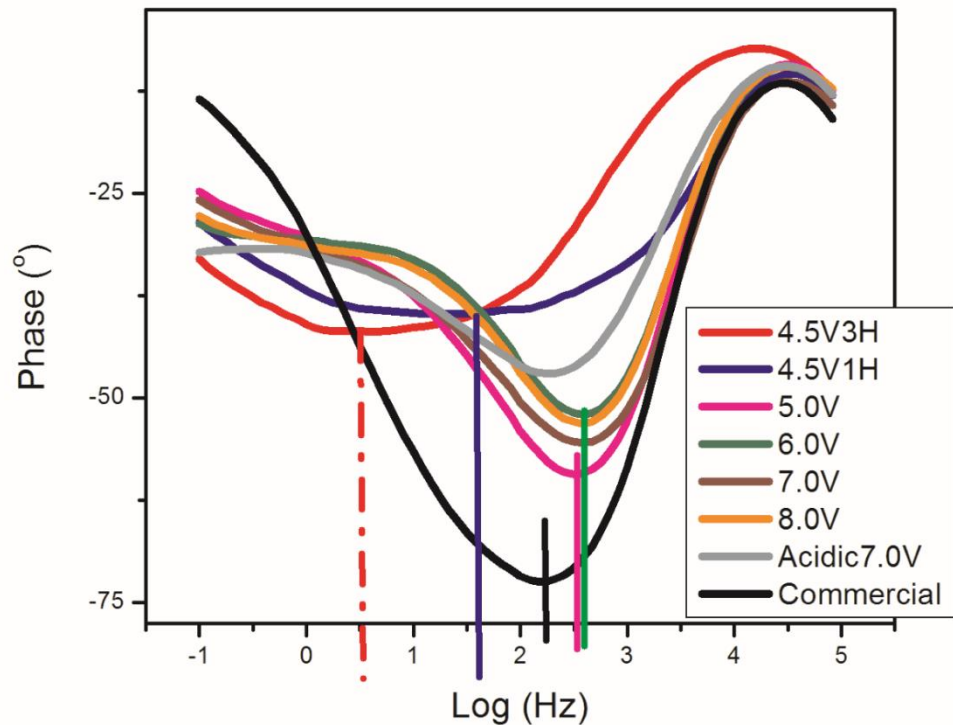


Fig. 39. Phase-Log(Frequency) spectrum (Bode plot) to determine carrier lifetime by f_{max} .

$$\tau = \frac{1}{2\pi f_{max}}$$

Eq. 21.

Where, τ is the carrier lifetime (Table 5) and f_{max} represents the frequency at the peak of the phase plot. What was observed across the samples was that the peak shifted towards higher frequencies at higher potentials and, therefore, carrier lifetime decreased as the applied potential increased. A minimum occurred at 0.418 ms at 6.0 V, which was maintained until 8.0 V. This indicated that the synthesis process that had occurred above 6.0 V had no further impact on the carrier lifetime. When comparing the acidic conditions to the standard 7.0 V sample, the introduction of an acidic environment increased the carrier lifetime to 0.823 ms. This was possibly due to changes to the surface termination ions. The largest carrier lifetime was produced by the three-hour sample, which had a lifetime of 37.9 ms. This was significantly larger than any previous sample. This effect is largely considered to be caused by a higher crystallinity in the sample due to the larger size or possible increase in trap states (i.e., defects). Comparing all samples to the commercial material at 0.996 ms, the commercial material performed better than the samples that were synthesized at 5.0 V – 8.0 V; however, this fell short in the 4.5 V samples. This overall associated increase could imply that there was a structural impact at 4.5 V.

Table 5. Calculated carrier lifetimes of synthesized samples.

Sample	4.5V-3H	4.5V-1H	5.0 V	6.0 V
Carrier lifetime (ms)	37.90	8.57	0.50	0.42
Sample	7.0 V	8.0 V	Acidic 7.0 V	Com
Carrier lifetime (ms)	0.42	0.42	0.82	0.99

7.3. Photocurrent

PV/PECs are often evaluated based on a J-t response curve analysis. The Cu₂O electrodes were subjected to the same illumination (Xenon flashlight 95W) under a chopped light condition (i.e., 50 seconds on, 50 seconds off) (Fig. 40). A moveable object that was capable of blocking all light from reaching the sample was utilized for a total time of 450 s. This was to prevent any possible “warm up” times that could potentially shift the intensity of the light.

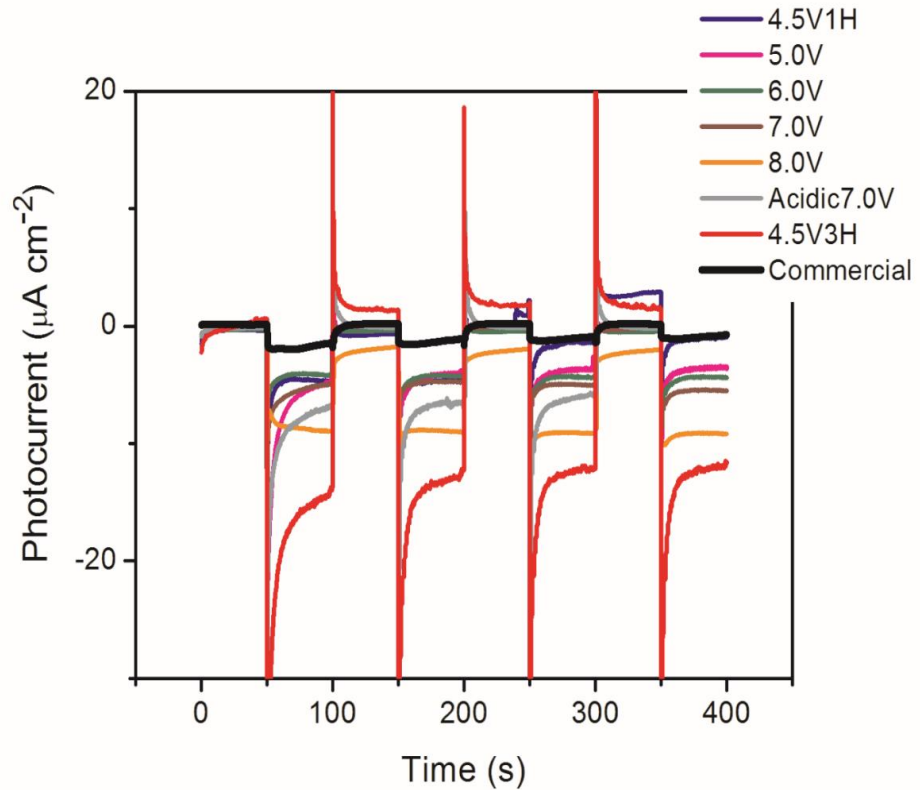


Fig. 40. Photocurrent generated under OCP conditions. Samples exposed to illumination and dark conditions for 50 s intervals for a total of 400 s.

Small increases were observed in the 4.5 V - 7.0 V applied potential samples. 4.5V-1H performed the poorest, which was unexpected due to the larger recombination time; however, this correctly correlates with the carrier concentration. Something else that must be taken into consideration is the shape difference between the 4.5 V sample(s) and the remaining samples. The star-like shapes of the samples may have an increased surface area. However, if they prevent proper contact with the FTO plate, then they may not be able to perform to the best of their capabilities. As the potential increased, a peak was reached at the largest sample, 8.0 V, which generated the highest photocurrent. This was

due to the increase in carrier concentration, slightly smaller size (i.e., larger surface area), and similar structure.

Looking at the extra samples (three-hour, acidic sample), a different effect was observed. The acidic sample appeared to produce a higher photocurrent as compared to the standard 7.0 V sample. This was unexpected due to its lower carrier concentration and less absorbance according to the % reflectance. However, the acidic sample did appear to have a longer recombination time. This information, along with a further investigation into the structure (i.e., TEM analysis), may help provide a better understanding. Shifting the attention towards the time-based sample, a significant increase in photocurrent occurred despite having a lower carrier concentration as compared to both the 7.0 V and 8.0 V samples. This large increase is assumed to have two underlying reasons: 1) The crystallinity of the sample was better due to the longer growth period, allowing for better charge transfer; and 2) The recombination time was significantly larger.

Looking deeper into the photocurrent of the time-altered sample, one key difference became obvious: the initial photocurrent was significantly larger as compared to the stable photocurrent (i.e., the initial photocurrent versus an end of 50 s). This spike is characteristically known as the “spike and overshoot”, which occurs in many metal oxide-based electrodes in response to chopped illumination [65]. This response is typically induced by a large concentration of holes or electrons that are being swept rapidly towards the semiconductor|electrolyte interface. However, due to the slow kinetics of the redox

reaction, the concentration of electrons/holes build until the “rate of arrival” for the electrons/holes is balanced by the rates of recombination and charge transfer. In summary, the initial spike is induced by the large concentration of electron/electron holes, which will reach an equilibrium as the rate of generation slows, resulting in the steady-state current. This can be further evaluated by determining the efficiency of the transfer by comparing the current at each location.

All of the samples were compared to the commercial material which, despite having the largest carrier concentration, a better recombination time, and better band bending had a significantly lower photocurrent in most samples. This impact is easily explained. The large particle size and organic coating (i.e., stability) prevented proper dispersion of the particles, which hindered a full coating despite coating the FTO plate with five times the concentration that was used for the synthesized nanoparticles.

7.4. Impedance Analysis

Fig. 41 represents the theoretical Nyquist plots expected for $\text{Cu}_2\text{O}/\text{FTO}$ electrodes when immersed in an aqueous electrolyte under either dark or illuminated conditions. As depicted, the two semi-circles under illuminated conditions represent the electron hole ejection at the Pt counter electrode|electrolyte junction, which is also known as transport resistance (R_{tr}). This is then followed by a larger semi-circle that is involved with the electron transfer from the Cu_2O surface to the electrolyte at the $\text{Cu}_2\text{O}/\text{Electrolyte}$ junction,

which is reported as the charge transfer resistance (R_{ct}). Finally, (R_s) contributes to the entire impedance spectra and is considered to be caused by the solution resistance.

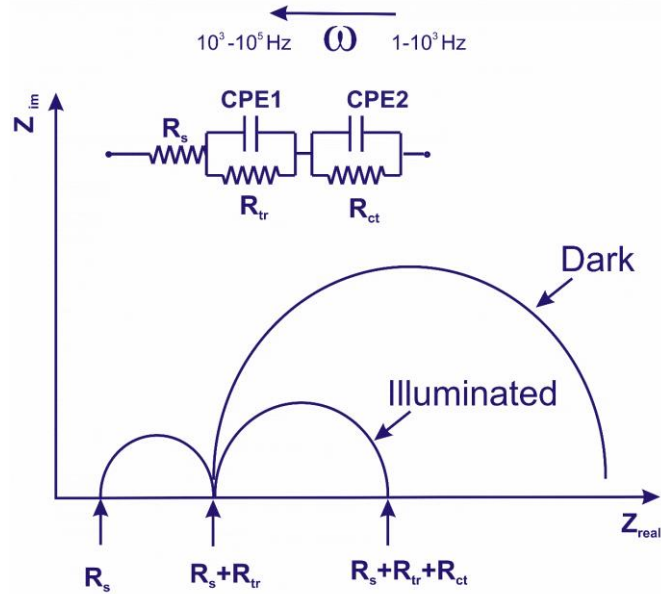


Fig. 41. Theoretical impedance spectra.

Impedance analysis was conducted under both illuminated and dark conditions, with a previously determined OCP applied. In a Nyquist plot, the diameter of the semi-circle represents the interfacial charge transfer resistance (R_{ct}). Finally, (CPE1) and (CPE2) represent the constant phase element, which models the behaviour of a double layer. Fig. 42 shows the impedance measurement for 8.0 V under dark and illuminated conditions. The performed measurements provided incomplete semi-circles; consequently, extrapolation of the semi-circle was required using Z-view. Based on these extrapolations, the diameter of the semi-circle decreased significantly upon illumination of the sample, as indicated by the red line. It can be surmised that, by illuminating the

sample charge transfer at the electrode|electrolyte interface, there is an increase in transfer efficiency. However, as demonstrated in Table 6, the calculated values of R_{ct} across all samples demonstrate no trend. Therefore, the applied potential during the synthesis is assumed to have no significant impact on the carrier transfer.

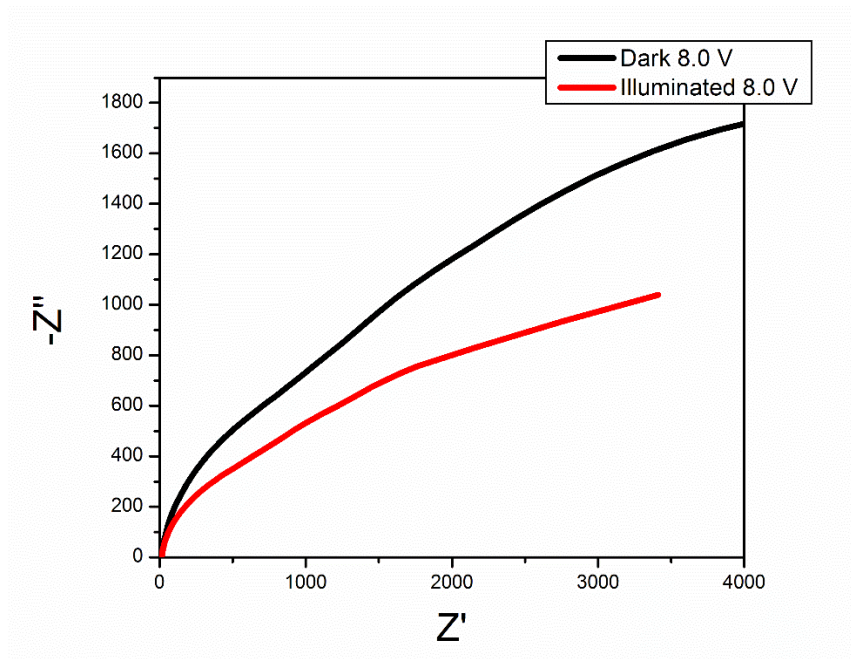


Fig. 42. Nyquist plot of sample synthesized at 8.0 V under both dark and illuminated conditions.

7.5. Charge Carrier Diffusion Length

Carrier diffusion length (L_n) within a metal oxide can be determined via impedance measurements, which characterizes the maximum travel distance of a carrier prior to recombination with an acceptor/electron within the electrolyte. This effect is often calculated in both dye sensitized and PEC cells. An efficient electron pathlength would be larger than the thickness of the respective metal oxide coating (L) in order to allow for sufficient time for charge separation to

occur before recombination. Therefore, examination of the thickness of the drop-cast layers was conducted by SEM and presented in Fig. 43. The electrodes were immersed in an epoxy resin and cut into thin layers. To estimate the thickness of the deposition, the obtained images were processed by an image processing software called Fiji (a derivative of Imagej). Thickness was estimated from this software by averaging thickness at different parts of the electrode. Ideally, the coating would be uniform, unbroken, and constant, which was sufficiently achieved during the deposition process.

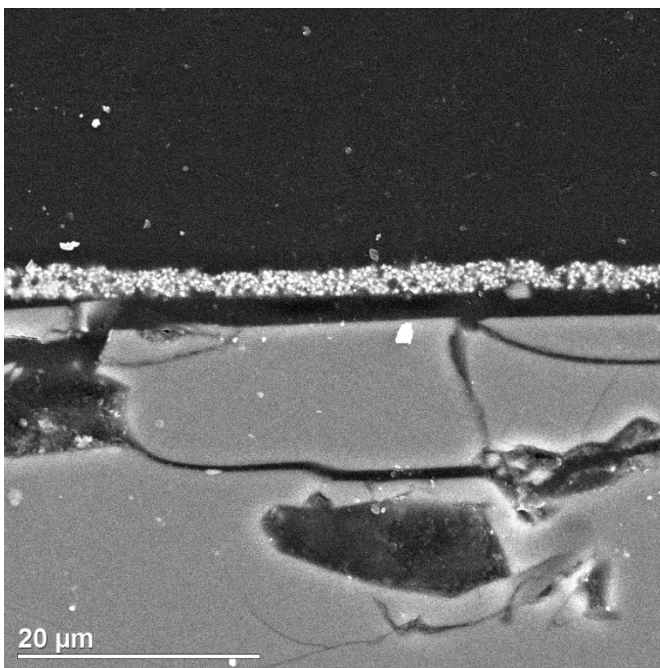


Fig. 43. Cross-section of Cu₂O layer on glass slide coated in epoxy-resin. The layer of Cu₂O is slightly suspended from the FTO depicted as a brighter white due to the cross section cut.

Carrier diffusion length [66] can be expressed as:

$$L_D = L * \sqrt{\left(\frac{\tau_n}{\tau_d}\right)} = L * \sqrt{\left(\frac{R_{ct}}{R_{tr}}\right)}$$

Eq. 22.

Where, L is the thickness of the deposition, τ_n is the charge lifetime, τ_d is the charge extraction time, R_{ct} is the charge recombination resistance, and R_{tr} is the macroscopic transport resistance. By utilizing Nyquist plots, it was possible to obtain R_{ct} and R_{tr} , which was then paired with the value of L that was obtained from the SEM presented in Table 6. The observed ratios of R_{ct} to R_{tr} implies that the charge carrier collection was efficient; however, this was dwarfed in comparison to the commercial material. This effect is assumed to be caused by the difference between large, highly crystalline particles as compared to the nanoparticles that were synthesized. Among the synthesized samples, no apparent trend occurred as both 5.0 V and 7.0 V displayed similar values to each other. This was also observed at 6.0 V and 8.0 V. The largest ratios were observed in the 4.5 V samples, which also visually appeared to be the most porous samples. Thus, the impact on diffusion pathlength is largely expected to be influenced by the uniformity of the deposition, but not to have a significant impact on the photochemistry of each electrode.

Table 6. Calculated values of R_{ct} , R_{tr} , R_{ct}/R_{tr} , L_D by Nyquist plot.

Sample	4.5 V-3H	4.5 V-1H	5.0 V	6.0 V
R_{ct}	1399.38	1038.13	1102.79	712.86
R_{tr}	14.89	11.56	16.084	14.95
R_{ct}/R_{tr}	93.99	89.83	68.57	47.69
L_D (μm)	20.84	20.38	17.80	14.85
Sample	7.0 V	8.0 V	Acidic	Com.
R_{ct}	987.36	697.45	827.54	5666.36
R_{tr}	14.67	14.13	13.90	16.99
R_{ct}/R_{tr}	67.31	49.37	59.54	333.41
L_D (μm)	17.64	15.11	16.59	39.26

8.0. Summary

Predicting the response for the photocurrent is very difficult as many properties need to be taken into account. This includes such properties as shape, size, carrier lifetime, band bending, carrier concentration, band-gap, charge transfer resistance, crystallinity, defects, and photoabsorbance. However, with this in mind, attempts were made to make educated predictions as to how well something may perform during synthesis via BPE. What was discovered was that, by increasing the applied potential, the crystallite size of the material decreased, which enabled a larger density of particles per unit area for electrode fabrication. What was also observed was that, by increasing the potential, the carrier concentration increased and the flat band potential shifted towards more positive values. These resulted in an increase in photocurrent generation for the Cu_2O -fabricated electrode.

Additionally, the trial that was completed at 4.5 V-1H versus 4.5 V-3H demonstrated an increase in carrier concentration and flat band potential with increasing time, which was likely caused by the increased crystallinity of the product (i.e., the crystals were given a longer duration to form). These results compared well with the observed increase in photocurrent. Comparing the synthesized samples to the commercial material, however, it is noted that the commercial material out-performed the 5.0 V – 8.0 V of the bipolar electrochemically synthesized samples in recombination time, carrier concentration, and flat band. Despite this, the commercial material performed significantly less in regards to the photocurrent generated. This result is caused

by the value of photogenerated carriers, as the volume of photogenerated carriers is significantly impacted by the material's capabilities at absorbing light (refer to the % reflectance spectra in Fig. 35.). The significantly reduced absorption of the light likely impacted the photogeneration significantly, therefore, decreasing photocurrent generation.

4.5 V-1H also demonstrated properties outside the expected means by producing increased carrier concentration, flat band potential, and carrier lifetime as compared to 5, 6, and 7 V samples. Despite this, the sample generated the least photocurrent. This effect is likely caused by the potential shift in structure, as demonstrated by the TEM/SEM images. PEC cells have a preference for 111 orientation to be facing the electrolyte paired with sufficient contact with the FTO plate. Therefore, if the structure has insufficient contact, leakage of current would be expected to cause the decrease in photocurrent generation.

The pH of the solution is known to have an impact on Cu_2O 's photocurrent by altering the concentration of oxygen on the surface of the crystal structure. However, no significant impact occurred within one sample. Therefore, further research must be completed for any definitive conclusion to be made about the impact of pH on the bipolar synthesis of Cu_2O . There is still much work to be done to improve the photocurrent that is generated by these particles. As was previously discussed, the 4.5 V-1H sample also had an extremely large initial photocurrent spike. This can be reduced by increasing the charge transfer of the photogenerated carriers, which would allow for the

photocurrent to reach closer to the initial spike levels. This can also be achieved by changing the contact plate or possibly by annealing the sample.

Finally, it is recommended that all future samples be synthesized at a high potential (8.0 V and above) and paired with an increased reaction time (three hours). An in-depth time trial would be required to determine the specific time needed. Building on this, the second set of experiments were developed; isolating the influence of pH by keeping the synthesis time for three hours at 8.0 V, while adjusting pH from pH 12 – 4. The results are introduced in section 9.0.

9.0. pH Analysis of Powders and Plates

9.1. Introduction

As previously stated, it has been determined that the pH of the solution can have a heavy influence on the properties of Cu₂O due to potentially causing a doping effect (H⁺), a shift in termination ions (Cu⁺, O²⁻), or even by altering the presence of defects in the localized crystallite structure [19]. In fact, pH can have such a profound influence over Cu₂O that, instead of just influencing the properties (e.g., flat-band, carrier concentration, carrier lifetime), it can also alter shape, crystal orientation, grain size, and even the type of semi-conducting nature of the metal oxide. Therefore, based on the previous results, a decision to look further into the possible implications of pH on the bipolar electrochemical synthesis of Cu₂O was made.

9.2. Cu₂O Plates and Powder Synthesis Conditions

Cu₂O was prepared similarly to the previously used method, with the exception of the addition of NaOH for samples synthesized at pH 8–12 and acetic acid for pH 4–6. All samples were adjusted drop-wise while under stirring for homogeneity. pH was measured by a pH meter (Science workshop 500 interface). Upon obtaining each specific pH level, all samples were subjected to 8.0 V at 80°C for three hours. The decision to expand the synthesis time to three hours was based on the significant increase in photocurrent that was observed in the results with respect to the three-hour trial as compared to the one-hour trials. The applied potential was also kept at 8.0 V due to this level of voltage having

presented the most promising photocurrent generation results during the one-hour synthetic conditions. It is important to note that the synthesis of Cu_2O was successfully completed for all samples; however, the samples prepared at a high pH (10-12) were produced rapidly as the orange suspended particles formed within 10 minutes of the applied potential. While at pH 6-8, the reaction progressed normally, with the orange suspended particles forming after approximately 30 minutes. Lastly, at pH 4, the Cu_2O formed at a very slow pace as the solution progressed to a deeper blue colour until about two hours had passed; this is when the solution suddenly progressed towards the desired orange product. This relationship is represented in Fig. 44. When comparing the synthesis at all pH levels above pH 4, a significant increase in current was induced by the generation of Cu^{2+} ions; however, no significant increase occurred at pH 4 until about an hour and forty minutes into the experiment. The bipolar electrode was collected, washed with DI H_2O , and dried. What was observed was a thick deep-red layer on the surface of the electrode.

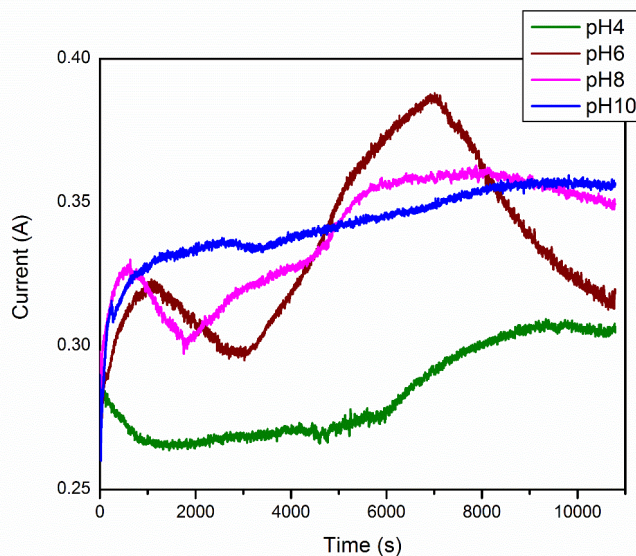


Fig. 44. Current increase and decrease due to Cu ion generation and consumption with respect to samples prepared by specific pH.

9.3. Powder Characterization

9.3.1. X-Ray Diffraction Analysis

Initial characterization was carried out by XRD analysis (Fig. 45) and was compared to the previously synthesized 8.0 V sample that was synthesized over one hour at pH 6.8. Both powder and Cu plate samples were collected for XRD analysis. XRD confirmed the presence of Cu_2O , with the absence of Cu or CuO. This indicated that, despite pH alteration, the material remained phase pure. By comparing this to the original 8.0 V sample, a significant increase in the peak intensity for the product that was prepared under basic conditions was observed. This implies that the crystallinity increased significantly. This was assumed to be caused by the facilitating nature of basic conditions for the formation of Cu_2O . However, a small increase was also observed under acidic conditions. The small

increase, despite the inhibitory effect under acidic conditions, was likely caused by the three-hour synthesis period versus the original sample's one-hour duration. Thus, the crystallinity of both samples under acidic and basic conditions increased. The relative peak intensity of the (111) peak, as compared to the higher facet peaks, increased under basic conditions. This implies that the acidic conditions may have a slight increase in catalytic properties due to the presence of higher facets.

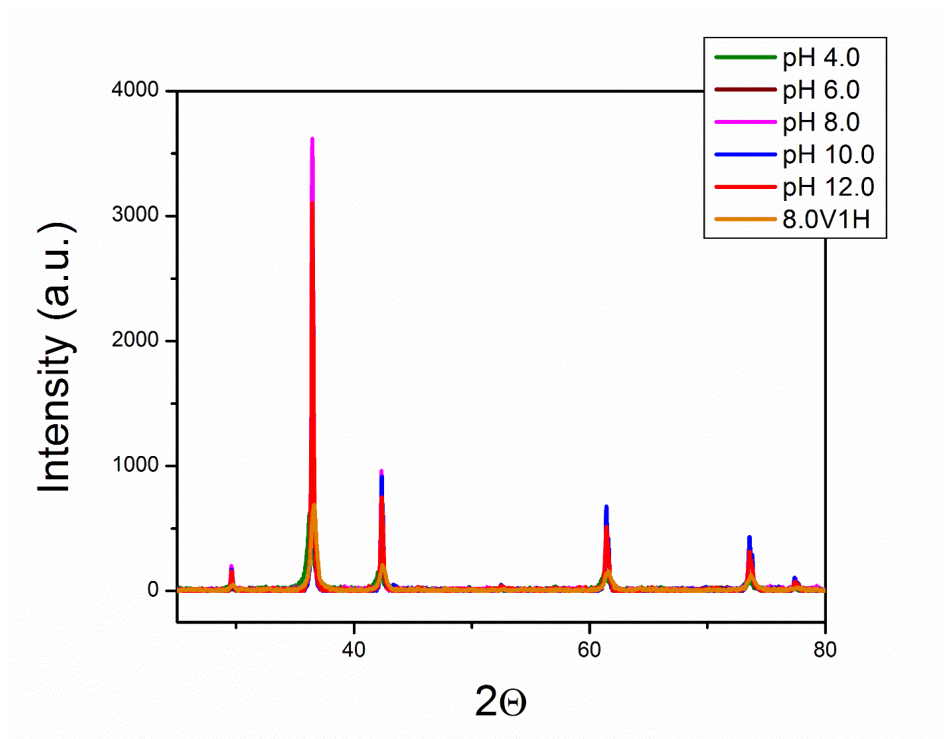


Fig. 45. XRD of the powders for the pH samples compared to 8.0 V-1H sample previously synthesized.

The XRD was also measured on the BPE electrode from pH 10 – 4 (Fig. 46). XRD results depicted a small shift in the 2θ values with respect to the powder sample, which was assumed to be due to the effect of graphing onto the plates as compared to the free-flowing powder samples. The peak positions all

correspond to Cu_2O , with the absence of Cu or CuO. This implies that the layer was thick enough to prevent the detection of Cu metal beneath the Cu_2O layer. However, impurity was detected on the surface of the BPE, as determined by the two peaks occurring at approximately 44 and 51 2θ . These impurities correspond to the degradation that occurred on the driving electrode and its deposition onto the surface of the BPE. The relative peak intensities imply that the growth remained with a preferred 111 orientation. No significant change was detected by shifting the pH, which suggests that no change occurred on the crystal structure with respect to the pH.

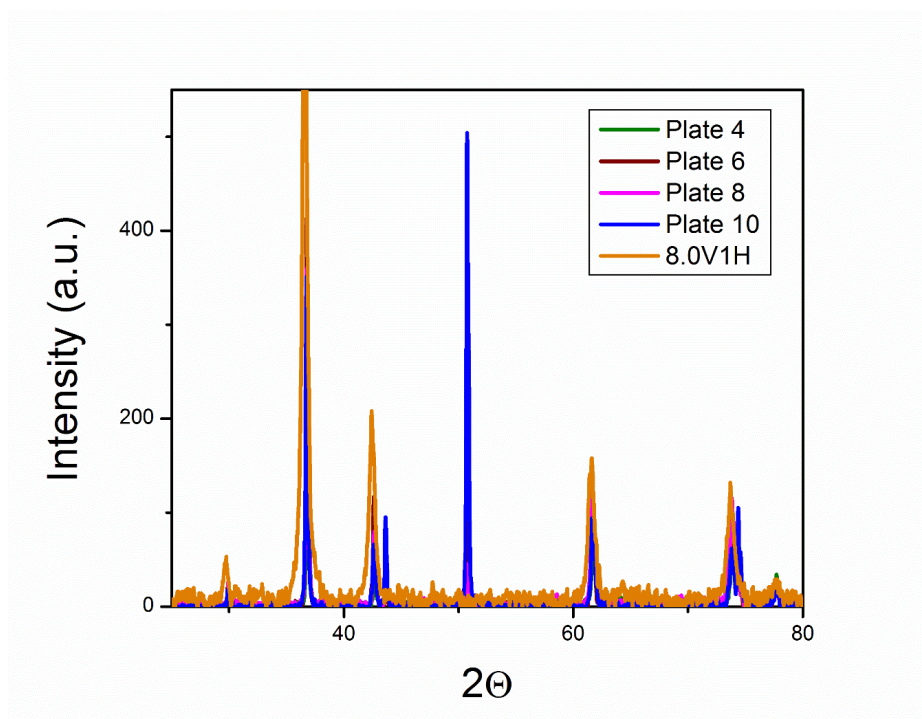


Fig. 46. XRD of Cu_2O layer formed on Cu plate during synthesis at various pH.

9.3.2 (Photo) Electrochemical Analysis

Electrochemical analysis (i.e., M-S and Bode) was conducted on the powder samples; however, this was not completed on the plates due to the inability to isolate the Cu_2O layer. The Cu-exposed surface on the back of the Cu plate could potentially enable interference on the desired properties for M-S/Bode diagrams and were, therefore, omitted. The electrodes were fabricated using the same methods as discussed previously, which resulted in uniform films and mounted inside of 0.5 M solution of NaSO_4 as an electrolyte. This was conducted under OCP conditions.

M-S analysis was conducted using the previously discussed methodology across the voltage range $-0.7 - 0$ V (Fig. 47.). As progression towards 0 V, the applied voltage lead to an increase in the space charge region of the Cu_2O |Electrolyte interface, which resulted in a decrease in the presented plot. A negative slope associated with a M-S plot can be used to determine whether the material has P-type characteristics. The carrier concentration and flat band potential were determined via the slope and x-intercept, respectively, by extrapolating the linear region of the M-S plot. These are presented in Table 7.

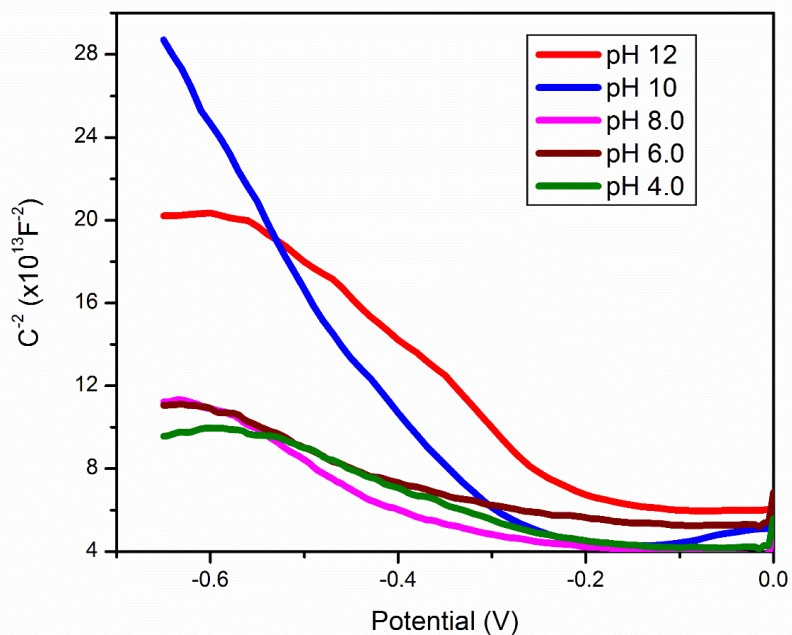


Fig. 47. M-S plot across -0.7 – 0 V applied potential for samples synthesized with varying pH levels.

The carrier concentration increased as the solution became more acidic. Nevertheless, there was an exception at pH 10. The increase in carrier concentration was likely caused by H^+ doping that could have occurred under acidic conditions. The flat-band potential, however, demonstrated that no significant trend was likely to have been caused by the difference in crystallinity of the product, as compared to the H^+ doping effect. Acidic conditions generated less crystalline substances; therefore, this could have countered the impact that was expected from H^+ doping on the flat-band potential.

Table 7. Carrier concentration (Con), Flat-band potential (FB) obtained by M-S for pH samples

Sample	pH 4	pH 6	pH 8	pH 10	pH 12
Con (cm⁻³)	1.13*10 ¹⁷	9.35*10 ¹⁶	6.75*10 ¹⁶	2.47*10 ¹⁶	5.04*10 ¹⁶
FB potential (V)	0.02	-0.063	-0.208	-0.284	-0.03

Following the M-S plot, Bode plots were taken to determine the impact of pH on the carrier lifetime of Cu₂O. As shown in Fig. 48 and Table 8, pH 8 had the worst recombination rate (i.e., the shortest time), which implies that the lack of facilitation of crystal formation (i.e., under basic conditions), as well as the decrease in carriers present (i.e., acidic conditions), negatively impacted the recombination rate. This allowed for the pH 8 sample to have similar recombination rates to the 8.0 V-1H sample that was previously synthesized. pH 12 and 6 demonstrated the same recombination rate, with a small increase at pH 4. The overall impact on carrier lifetime, however, was insignificant, with a total difference of 1.13 ms.

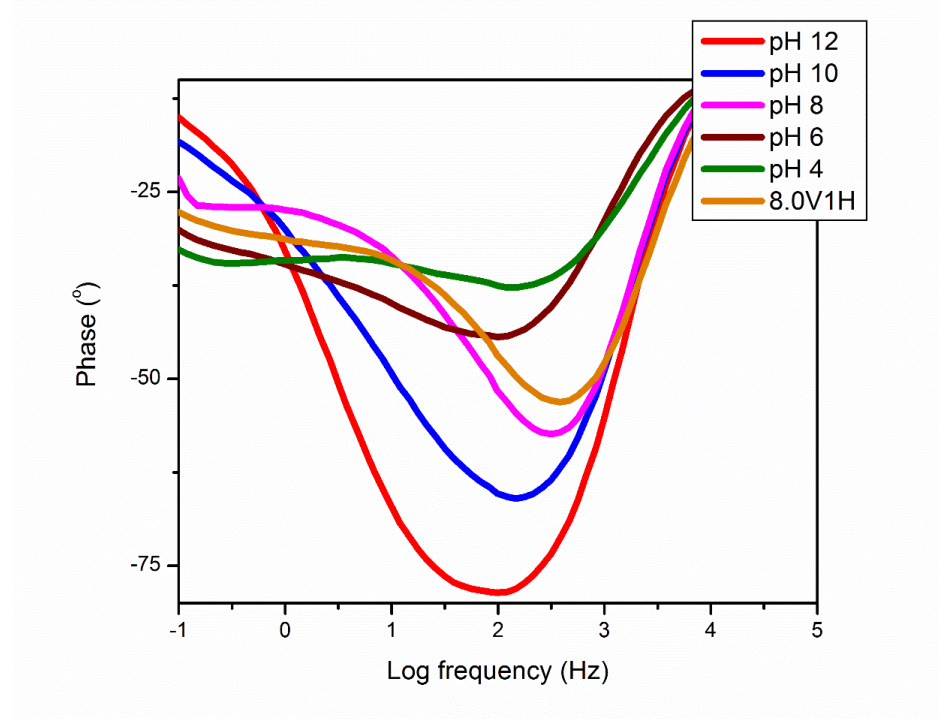


Fig. 48. Bode analysis of pH samples

Table 8. Carrier lifetime of pH samples

Sample	pH 4	pH 6	pH 8	pH 10	pH 12
Carrier lifetime (ms)	1.303	1.63	0.503	1.09	1.63

Photocurrent experiments were also conducted on both the Cu₂O plates and powders via alternating on and off illumination conditions with a Xe lamp. Fig. 49 represents the results for the powders. Interestingly, the photocurrent that was generated by powders synthesized at pH 10 and 12 generated a smaller amount of current with respect to the 8.0 V-1H sample, despite being synthesized over three hours instead of the original one-hour duration. As the previous study

suggests, it is expected that samples produced over a longer duration should have greater photocurrent generation.

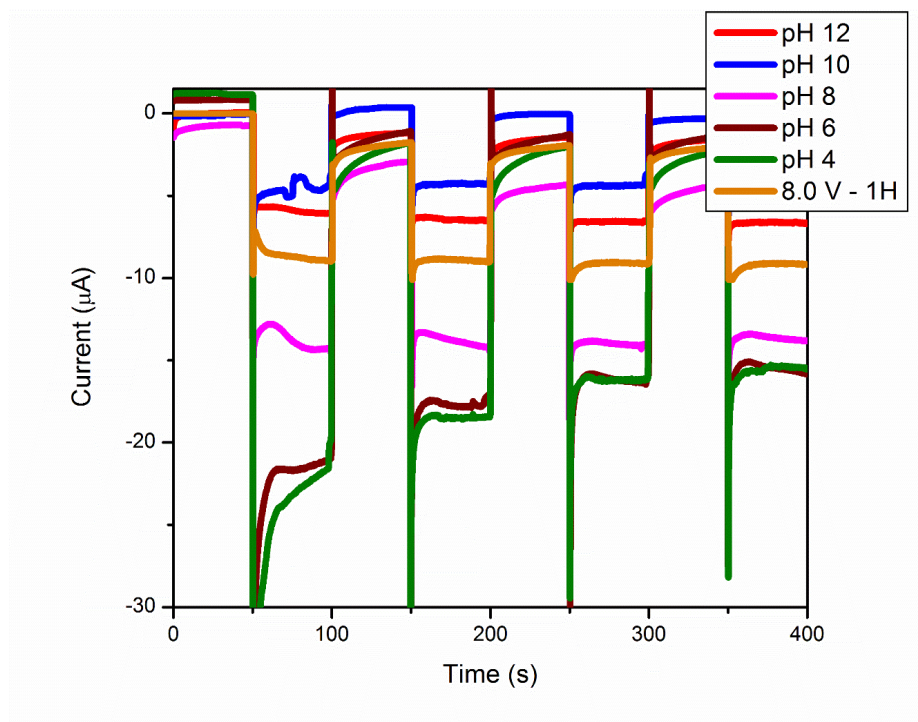


Fig. 49. Photocurrent generation of pH by Xe lamp alternating illumination with 8.0 V-1H serving as a reference material.

On the other hand, photocurrent generation increased as the pH of the solution decreased. Therefore, pH had a significant impact on the photocurrent generation by impacting the carrier concentration. More significant transient peaks were observed in the acidic samples than the samples that were prepared in the more basic media. This indicates that the material formed under acidic conditions exhibits a difficulty with electron transfer, which is possibly due to the decrease in crystallinity.

It has been reported recently [32] that by altering the pH conditions during the synthesis of Cu_2O , this impacts the performance of the material. This

can go as far as inverting the semi-conducting properties from P- to N-type. However, this was not the case here. Altering the pH produced an increase in the photocurrent generation, but did not result in any inversion.

Looking further into this potential inversion, the Cu plates were used to determine if any change would occur on the Cu_2O layer that was formed on the plates directly. Fig. 50 represents the photocurrent that was generated on the Cu plates from pH 4-10. pH 10 demonstrated the largest P-type photocurrent, while pH 6 and 8 had decreased performance; however, they still resulted with an overall P-type semi-conducting property. Interestingly, when the pH was reduced to 4, the photocurrent inverted to N-type behaviour, despite the corresponding powder continuing to display as a P-type. N-type Cu_2O properties were demonstrated. This matches well with previous literature [37] as, when there was an increase of pH, the conductivity properties for Cu_2O shifted towards becoming N-type. This has been proposed to be caused by inducing an O_2 vacancy effect by two possible mechanisms: 1) H_2 adsorption to the O_2 terminating ions, resulting in a similar effect to O_2 defecncies; or 2) By forming on the Cu metal surface, it is likely that less Cu vacancies form due to the Cu rich environment, which would ultimately result in less Cu vacancies compared to O_2 vacancies and N-type characteristics. However, no final conclusions could be reached from this area of research, so the origin of the N-type properties remain to be determined.

As reported by Jayathilaka et al. [37], the inversion of the semi-conducting properties is likely effected not only by the pH of the solution, but by

the localized concentration of Cu^{2+} species. Many researchers refer to the inversion of Cu_2O properties via the pH of the solution. Due to the excess of Cu species present by the Cu precursors, the effect of concentration is commonly ignored. In the bipolar reactor, the localized increase of Cu species around the BPE allowed for the conversion of the Cu_2O layer, which was formed on the surface of the electrode. In comparison, the powder formed in the solution, where the concentration of Cu species remained minimal.

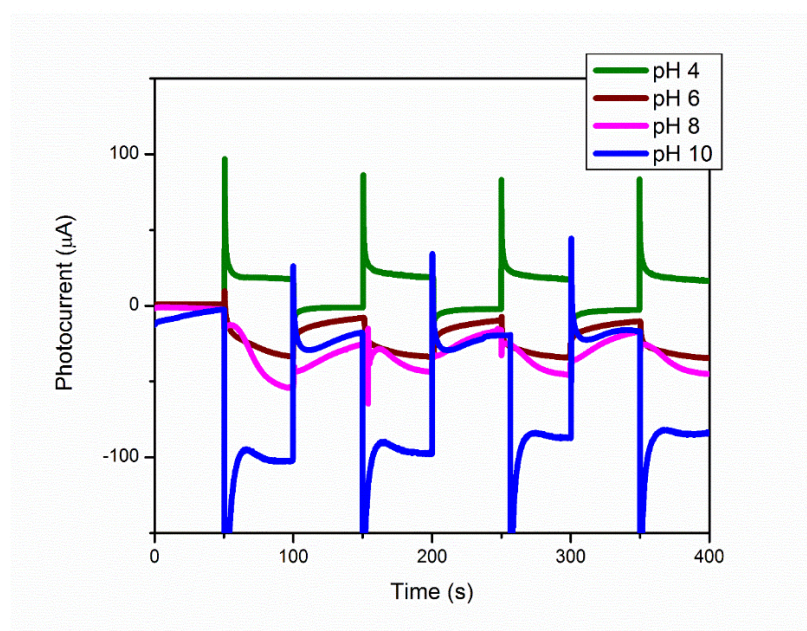


Fig. 50. Photocurrent generation by Cu BPE immersed in sodium sulfate electrolyte under alternating illumination conditions.

9.4 Conclusion

Despite the limitation of product formation at low pH due to a lack of OH^- species, XRD determined that all samples synthesized maintained their single phase nature for both the Cu plate and powder samples. pH studies revealed that, by reducing the pH of the solution, an increase in the carrier

concentration of Cu_2O powders could occur, with a total shift of 8.83×10^{16} from pH 10 to 4. Flat-band potential experienced a shift, with the best values having been obtained at pH 4 and 12. This indicates that the increase in carrier concentration may have influenced the pH 4 sample, while crystallinity may have impacted the pH 12 sample. However, no significant impact occurred on the sample's carrier lifetime as the largest shift was only 1.129 ms.

The most interesting result in this study came from comparing the photocurrent of the powder and plate samples under alternating illumination and dark conditions. The grafted samples on the surface of the BPE exhibited inversion of the semi-conducting properties for Cu_2O , which indicates that both pH and Cu concentration were sufficient for inversion. This result helps reinforce the previously determined conclusion that both concentration of Cu species and powder likely play a significant role in the properties of Cu_2O . Despite a sufficient decrease of pH (to 4), the powder samples did not display an inversion of semi-conducting properties. Instead, lowering the pH of the solution resulted in an increase in the carrier concentration, and consequently, an increase in its capabilities and photocurrent generation. However, photocurrent generation demonstrated no significant impact beyond pH 6. Thus, in order to keep the reaction in good yield, pH 6 is recommended to be utilized during further research on the optimization of Cu_2O synthesis.

10.0. Future Research

The work presented here determined that the synthesis of Cu_2O powders, and even thick layers onto Cu electrodes, was possible, all while maintaining a green methodology by utilizing reusable-multiapplicable electrolyte for conductivity, complexation, and reduction of Cu species. This discovery was further examined by studies into effect of the applied potential, time, and pH of the synthetic process, which allowed for the optimization of the photosensitivity of the Cu_2O product. The question then lies: What lies ahead? Research into Cu_2O is significantly far from current use in industrial applications due to its aqueous instability, photocurrent optimization, and electron scavaging issues. As previously mentioned, Cu_2O is extremely sensitive to its method of synthesis and, therefore, these properties could begin to be remedied by changing the complexing agent that is involved in the bipolar reaction. This could potentially allow for material to be further optimized. Besides the exchanging of complexing agents, changes in the electrode preparation, as well as annealing, could lead to significant increases in photocurrent generation and stability of the fabricated electrodes.

Although PVs and PEC cells are the most common applications of Cu_2O , other applications should be explored in future studies. Future applications range from dye degradation (e.g., methylene orange) to electrochemical CO_2 reduction, all the way to potential fuel sources. As the material synthesized is in powder form, ideal applications would involve the suspension of the material in an electrolyte to provide the possibility of capitalizing on its porous structure.

11. References

- [1] Manohara, G. V. "Exfoliation of layered double hydroxides (LDHs): a new route to mineralize atmospheric CO₂". *RSC Advances* (2014), 4(86), pp. 46126-46132.
- [2] Canada, Natural resources. 2020. "Electricity Facts | Natural Resources Canada". *Nrcan.Gc.Ca*. <https://www.nrcan.gc.ca/science-data/data-analysis/energy-data-analysis/energy-facts/electricity-facts/20068>.
- [3] N. L. Panwar, S. C. Kaushik, and S. Kothari, "Role of renewable energy sources in environmental protection: A review," *Renew. Sustain. Energy Rev.* (2010), 15(3), pp. 1513–1524.
- [4] Sun, S., Zhang, X., Yang, Q., Liang, S., Zhang, X. and Yang, Z. Cuprous oxide (Cu₂O) crystals with tailored architectures: A comprehensive review on synthesis, fundamental properties, functional modifications and applications. *Progress in Materials Science* (2018), 96, pp. 111-173.
- [5] Bagal, I., Chodankar, N., Hassan, M., Waseem, A., Johar, M., Kim, D. and Ryu, S. "Cu₂O as an emerging photocathode for solar water splitting - A status review". *International Journal of Hydrogen Energy* (2019), 44(39), pp. 21351-21378.
- [6] R. M. Adams, "Global Climate Change and Agriculture: An Economic Perspective," *Am. J. Agric. Econ.* (1989), 71(5), pp. 1272 - 1989.
- [7] C. Rosenzweig, A. Iglesias, X. B. Yang, P. R. Epstein, and E. Chivian, "Climate change and extreme weather events", *Global Change & Human Health* (2001), 2(2), pp. 90–104.
- [8] Howard, Brian. 2019. "First Mammal Species Goes Extinct Due To Climate Change". *Nationalgeographic.Com*.<https://www.nationalgeographic.com/news/2016/06/first-mammal-extinct-climate-change-bramble-cay-melomys/>.
- [9] Energypowerlab. (2019). Executive recruitment for the energy industry. [online] Available at: <https://energypowerlab.com/renewables-supply-25-of-global-power-in-2017>
- [10] R. Mabro, "The future of oil," *Futur. Oil as a Source Energy* (2003), pp. 3–11.
- [11] Park, N., Grätzel, M. and Miyasaka, "Organic-Inorganic Halide Perovskite Photovoltaics.", *Springer* (2016).
- [12] H. Spanggaard and F. C. Krebs, "A brief history of the development of organic and polymeric photovoltaics," *Sol. Energy Mater. Sol. Cells* (2004), 83(2–3), pp. 125–146.
- [13] Zahedi, A. Solar photovoltaic (PV) energy; latest developments in the building integrated and hybrid PV systems. *Renewable Energy* (2006), 31(5), pp. 711-718.
- [14] Ellabban, O., Abu-Rub, H. and Blaabjerg, F. "Renewable energy resources: Current status, future prospects and their enabling technology". *Renewable and Sustainable Energy Reviews* (2014), 39, pp. 748-764.

- [15] Gupta, Nishant & Alapatt, Githin & Podila, Ramakrishna & Singh, Rajneel & Poole, K.F. “Prospects of Nanostructure-Based Solar Cells for Manufacturing Future Generations of Photovoltaic Modules. International Journal of Photoenergy.” *Int. Journal of photoenergy* (2009): 1.
- [16] Yoon, J., Sun, Y. and Rogers, J. “Semiconductor Nanomaterials for Flexible Technologies: From Photovoltaics and Electronics to Sensors and Energy Storage.” Elsevier Ltd (2010), pp.159-196.
- [17] Jacobsson, T., Fjällström, V., Edoff, M. and Edvinsson, T. “CIGS based devices for solar hydrogen production spanning from PEC-cells to PV-electrolyzers: A comparison of efficiency, stability and device topology.” *Solar Energy Materials and Solar Cells* (2015), 134, pp.185-193
- [18] Lin, W. “Manifestation of Photocatalysis Process Variables in a Titanium Dioxide-Based Slurry Photoelectrochemical Cell.” *Journal of The Electrochemical Society* (1997), 144(2), p. 497.
- [19] Jia, J., Seitz, L., Benck, J., Huo, Y., Chen, Y., Ng, J., Bilir, T., Harris, J. and Jaramillo, T. “Solar water splitting by photovoltaic-electrolysis with a solar-to-hydrogen efficiency over 30%.” *Nature Communications* (2016), 7(1).
- [20] Dincer, I. and Acar, C. “Review and evaluation of hydrogen production methods for better sustainability.” *International Journal of Hydrogen Energy* (2015), 40(34), pp. 11094-11111.
- [21] Husain, A., Hasan, W., Shafie, S., Hamidon, M. and Pandey, S. “A review of transparent solar photovoltaic technologies.” *Renewable and Sustainable Energy Reviews* (2018), 94, pp.779-791.
- [22] Goetzberger, A., Hebling, C. and Schock, H. “Photovoltaic materials, history, status and outlook.” *Materials Science and Engineering: R: Reports* (2003), 40(1), pp.1-46.
- [23] Scanlon, D. and Watson, G. “Undoped n-Type Cu₂O: Fact or Fiction?”. *The Journal of Physical Chemistry Letters* (2010), 1(17), pp. 2582-2585.
- [24] Y. Ren, Z. Ma, and P. G. Bruce, “Ordered mesoporous metal oxides: synthesis and applications,” *Chem. Soc. Rev.* (2012), 41(14), p. 4909.
- [25] A. H. Moharram, S. A. Mansour, M. A. Hussein, and M. Rashad, “Direct precipitation and characterization of ZnO nanoparticles,” *J. Nanomater.* (2014)
- [26] S. Kerli and Ü. Alver, “Preparation and Characterisation of ZnO / NiO Nanocomposite Particles for Solar Cell Applications,” *J. Nanotechnol.* (2016), pp. 1–5.
- [27] A. Naveed Ul Haq, A. Nadhman, I. Ullah, G. Mustafa, M. Yasinzai, and I. Khan, “Synthesis Approaches of Zinc Oxide Nanoparticles: The Dilemma of Ecotoxicity,” *J. Nanomaterial.* (2017).
- [28] Yunusa, Abdu & Musa, A. “Copper (I) oxide (Cu₂O) based solar cells - A review”. *Bayero J. Pure Appl. Sci.* (2017), 2, pp. 8-12.

- [29] Raebiger, H.; Lany, S.; Zunger, A. "Origins of the p-Type Nature and Cation Deficiency in Cu₂O and Related Materials". *Phys. Rev. B* (**2007**), 76(4).
- [30] R. W. G. Wychoff, *Crystal Structure*, Volume 1, Wiley, New York (1965).
- Scanlon, D. and Watson, G. "Undoped n-Type Cu₂O: Fact or Fiction?". *The Journal of Physical Chemistry Letters* (**2010**), 1(17), pp. 2582-2585.
- [31] Y. Lee, J. Heo, M. Winkler, S. Slah, S. Kim, R. Gordon, T. Buonassisi. "Nitrogen-doped cuprous oxide as a p-type hole-transporting layer in thin-film solar cells", *Journal of Materials Chemistry A* (**2013**), 1(48), pp. 15416.
- [32] Siripala, W. and Jayakody, J. "Observation of n-type photoconductivity in electrodeposited copper oxide film electrodes in a photoelectrochemical cell." *Solar Energy Materials* (**1986**), 14(1), pp. 23-27
- [33] Li, M., Zhang, J., Zhang, Y. and Wang, T. "Oxygen vacancy in N-doped Cu₂O crystals: A density functional theory study". *Chinese Physics B* (**2012**), 21(8), p.087301.
- [34] Zang, Z., Nakamura, A. and Temmyo, J. "Single cuprous oxide films synthesized by radical oxidation at low temperature for PV application". *Optics Express* (**2013**), 21(9), p.11448.
- [35] Wang, W., Wu, D., Zhang, Q., Wang, L. and Tao, M. "pH-dependence of conduction type in cuprous oxide synthesized from solution". *Journal of Applied Physics* (**2010**), 107(12), p.123717.
- [36] Zhang, N., Du, Y., Zhang, Y. and Wang, C. "A simple method for controlling the type of cuprous oxide semiconductors using different surfactants". *Journal of Materials Chemistry* (**2011**), 21(14), p.5408.
- [37] Jayathileke, K., Siripala, W. and Jayanetti, J. "Electrodeposition of p-type, n-type and p-n Homojunction Cuprous Oxide Thin Films". *Sri Lankan Journal of Physics* (**2010**), 9, p.35.
- [38] Betts. K., "How Industrial Applications in Green Chemistry Are Changing Our World". *American Chem. Soc.* (**2015**), pp. 1-32.
- [39] P. T. Anastas and J. C. Warner, "Green Chemistry: Theory and Practice," *Green Chem. Theory Pract.* Oxford Univ. Press. New York, p. 30, 1998.
- [40] J. H. Clark, "Green chemistry: challenges and opportunities," February, pp. 1-8, 1999.
- [41] D. J. C. Constable, A. D. Curzons, and V. L. Cunningham, "Metrics to 'green' chemistry—which are the best?," *Green Chem.*(**2002**), 4(6), pp. 521-527.
- [42] S. E. Fosdick, K. N. Knust, K. Scida, and R. M. Crooks, "Bipolar electrochemistry," *Angew. Chemie - Int. Ed.* (**2013**), 52(40), pp. 10438-10456.
- [43] Gamero-Quijano, A., Molina-Osorio, A., Peljo, P. and Scanlon, M. "Closed bipolar electrochemistry in a four-electrode configuration". *Physical Chemistry Chemical Physics* (**2019**), 21(19), pp. 9627-9640.
- [44] Duval, J., van Leeuwen, H., Cecilia, J. and Galceran, J. "Rigorous Analysis of Reversible Faradaic Depolarization Processes in the

- Electrokinetics of the Metal/Electrolyte Solution Interface”. The Journal of Physical Chemistry B (2013), 107(28), pp. 6782-6800.
- [45] A. Arora, J. C. T. Eijkel, W. E. Morf, A. Manz, Anal. Chem. (2001), 73, pp. 3282 – 3288.
- [46] Bradley, J.-C.; Chen, H.-M.; Crawford, J.; Eckert, J; Ernazarova, K.; Kurzeja, T.; Lin, M.; McGee, M.; Nadler, W.; Stephens, S.G. “Creating Electrical Contacts between Metal Particles using Directed Electrochemical Growth”, Nature (1997), 389, p. 268
- [47] Ramaswamy, R.; Shannon, C. “Screening the optical properties of Ag-Au alloy gradients formed by bipolar electrodeposition using surface enhanced raman spectroscopy”. Langmuir (2010), 27, pp. 878–881
- [48] Allagui, A., Alawadhi, H., Alkaaby, M., Gaidi, M., Mostafa, K. and Abdulaziz, Y.. Mott-Schottky analysis of flower-like ZnO microstructures with constant phase element behavior. physica status solidi (a) (2015), 213(1), pp. 139-145.
- [49] Hakimian, A., McWilliams, S. and Ignaszak, A. “ZnO Synthesized Using Bipolar Electrochemistry: Structure and Activity”. Materials (2019), 12(3), p.535.
- [50] Jenkins, R. and Snyder, R. “Introduction to X-ray powder diffractometry”. New York, NY: Wiley (2012), (138), pp. 1-432.
- [51] Bantz, C., Koshkina, O., Lang, T., Galla, H., Kirkpatrick, C., Stauber, R. and Maskos, M. “The surface properties of nanoparticles determine the agglomeration state and the size of the particles under physiological conditions”. Beilstein Journal of Nanotechnology (2014), 5, pp. 1774-1786.
- [52] Meghana, S., Kabra, P., Chakraborty, S. and Padmavathy, N. “Understanding the pathway of antibacterial activity of copper oxide nanoparticles”. RSC Advances (2015), 5(16), pp. 12293-12299.
- [53] Abbas, zena mohammed ali. “Study and Characterization of Copper Oxide Nanoparticles Prepared by Chemical Method using X-Ray Diffraction and Scanning Electron Microscope”. American Journal of Scientific Research (2012), 77, pp. 49-53.
- [54] Toby, B. EXPGUI,” A Graphical User Interface for GSAS”. Journal of Applied Crystallography (2001), 34(2), pp. 210-213.
- [55] A. C. Larson and R. B. von Dreele, “Los Alamos National Report LAUR”, 1994, 96, 86.
- [56] Foo, M., Huang, Q., Lynn, J., Lee, W., Klimczuk, T., Hagemann, I., Ong, N. and Cava, R. “Synthesis, structure and physical properties of Ru ferrites: BaMRu5O11 (M=Li and Cu) and BaM'2Ru4O11 (M'=Mn, Fe and Co)”. Journal of Solid State Chemistry (2006), 179(2), pp.563-572.
- [57] Howard, C. “The approximation of asymmetric neutron powder diffraction peaks by sums of Gaussians”. Journal of Applied Crystallography (1982), 15(6), pp. 615-620.

- [58] El Yacoubi, A., Massit, A., El Moutaoikel, S., Rezzouk, A. and Chafik El Idrissi, B. "Rietveld Refinement of the Crystal Structure of Hydroxyapatite Using X-ray Powder Diffraction". *American Journal of Materials Science and Engineering* (2017), 5(1), pp.1-5.
- [59] Sun, Lili & Guo, Peng & Ke, Pei-ling & Li, Xiaowei. "Synergistic effect of Cu/Cr co-doping on the wettability and mechanical properties of diamond-like carbon films. *Diamond and Related Materials*", Elsevier (2016), 68, pp. 1-8.
- [60] Biesinger, M. "Advanced analysis of copper X-ray photoelectron spectra". *Surface and Interface Analysis* (2017), 49(13), pp.1325-1334.
- [61] Neikov, O. and Yefimov, N. "Handbook of Non-Ferrous Metal Powders", Elsevier (2009), 1, pp. 271-311.
- [62] Mirjana, M., Zoran, G. and Sasha, O. "Change of n-type to p-type conductivity of the semiconductor passive film on N-steel: Enhancement of the pitting corrosion resistance". *Journal of the Serbian Chemical Society* (2013), 78(12), pp.2053-2067.
- [63] Sellers, M. and Seebauer, E. "Measurement method for carrier concentration in TiO₂ via the Mott-Schottky approach". *Thin Solid Films* (2011), 519(7), pp.2103-2110.
- [64] C V, Niveditha & Mj, Jabeen & Sindhu, Swaminathan. "Comprehensive Interfacial Study of Potentio-Dynamically Synthesized Copper Oxide Thin Films for Photoelectrochemical Applications". *Journal of The Electrochemical Society* (2016). 163(6), pp. H426-H433.
- [65] Dunn, H., Feckl, J., Müller, A., Fattakhova-Rohlfing, D., Morehead, S., Roos, J., Peter, L., Scheu, C. and Bein, T. "Tin doping speeds up hole transfer during light-driven water oxidation at hematite photoanodes". *Phys. Chem. Chem. Phys.* (2014), 16(44), pp. 24610-24620.
- [66] R. A. Wahyuono et al., "ZnO Nanostructures for Dye-Sensitized Solar Cells Using the TEMPO+/TEMPO Redox Mediator and Ruthenium(II) Photosensitizers with 1,2,3-Triazole-Derived Ligands" *Chempluschem* (2016), 81(12), pp. 1281–1291.

Curriculum Vitae

Candidate's full name: Steven Robert Curtis McWilliams

Universities attended:

University of New Brunswick, Fredericton, NB, Canada (Bachelor of Science, Chemistry, 2011-2016).

University of New Brunswick, Fredericton, NB, Canada (Masters of Science, Chemistry, 2017-2020).

Publications: Hakimian, A., **McWilliams, S.** and Ignaszak, A. "ZnO Synthesized Using Bipolar Electrochemistry: Structure and Activity". *Materials* (2019), 12(3), p. 535.

McWilliams, Steven; Flynn, Connor D.; McWilliams, Jennifer; Arnold, Donna C.; Wahyuono, Ruri A.; Undisz, Andreas; Rettenmayr, Markus; Ignaszak, Anna. (2019). "Nanostructured Cu₂O Synthesized via Bipolar Electrochemistry." *Nanomaterials* 9, no. 12: 1781.

Conference Presentations:

S. R. C. McWilliams, A. Ignaszak*. (June 2018) "Synthesis of Cuprous Oxide (Cu₂O): A Wireless Bipolar Electrochemical Approach" at CCCE 2019, Quebec, QC, Canada (MSc. Work – Oral presentation).

S. R. C. McWilliams, A. Ignaszak*. (June 2018) "Synthesis of Cuprous Oxide (Cu₂O): A Wireless Bipolar Electrochemical Approach" at ChemCon2018, Halifax, NS, Canada (MSc. Work – Oral presentation).